國立臺灣大學理學院化學研究所

碩士論文

Department of Chemistry

College of Science

National Taiwan University

Master's Thesis

應用量子薛丁格朗之萬方程式的研究在費米共振系統上之二維紅外光譜

Application of the Quantum Schrödinger-Langevin Equation Approach to Two-Dimensional Infrared Spectroscopy of Fermi Resonance Systems

尤俊皓

Jun-Hao Yu

指導教授: 鄭原忠 博士

Advisor: Yuan-Chung Cheng, Ph.D.

中華民國 113 年 9月

September, 2024

doi:10.6342/NTU202404353

國立臺灣大學碩士學位論文

口試委員會審定書

NTU Master's Thesis

Oral Defense Approval Form

應用量子薛丁格朗之萬方程式的研究在費米共振系統上之二維紅外光譜

Application of the Quantum Schrödinger-Langevin Equation Approach to Two-Dimensional Infrared Spectroscopy of Fermi Resonance Systems

本論文係 尤俊皓 君（學號 R11223119）在國立臺灣大學化學系完成之碩士學位論文，於民國 113 年 7 月 2 日承下列考試委員審查通過及口試及格，特此證明。

The student Jun-Hao Yu (student no. R11223119) enrolled in the Master Program of the Department of Chemistry, NTU has satisfactorily passed the oral defense on 2024/7/2 with the approval of all committee members as follows.

口試委員(Committee Members)：

吳哲源 （簽名 Signature）

郭哲孝（指導教授 Advisor） 林倫年

系主任、所長 陳振中 （簽章）

doi:10.6342/NTU202404353

Acknowledgements

在這兩年著實學到了很多東西。不管是鄭原忠老師每週的個別會議，還是在我遇到研究困難時，實驗室的同仁們的相助與熱烈討論，都使我收穫良多。此外很感謝鄭原忠老師讓我參加國科會化學鍵結整合型計畫，能在研究室之餘，能在週末和郭哲來老師、林倫年老師和黃千睿研究員討論科學問題，並且給予我很多的建議與研究動力。最後也要感謝金必耀老師在團體會議時的報告建議，能讓我反省報告裡做不夠好的地方。

doi:10.6342/NTU202404353

doi:10.6342/NTU202404353

摘要

紅外二維光譜為近二十年成為研究凝態中振動模資訊及微觀環境的化學工具。在模擬方法方面，目前仰賴分子動力學模擬，來得到無細節波包資訊之二維光譜。本研究之主題為得到精確的振動波包動態的情況下，模擬二維紅外光譜。吾人的方法是結合量子朗之萬方程式（quantum Langevin equation）、微擾理論（perturbation theory）和得到的非簡諧振動態的第一原理計算。並在以獨立震盪體（independent oscillators）模型描述系統環境耦合的物理模型為基礎，再搭配高斯波包近似法（Gaussian wavepacket approximation）後，得到量子薛丁格朗之萬方程式。而吾人將此模擬技術應用在有費米共振（Fermi resonance）現象的系統上。費米共振現象是在紅外光譜上具有特徵的現象，主要源自於振動模之間非簡諧耦合。在關於費米共振系統在紅外二維光譜之研究中，討論費米共振之光譜特徵的研究是較於缺乏的。故在這份研究中，吾人將會使用此二維紅外光譜模擬技術，來研究在二維光譜上費米共振的光譜特徵。在水合氫離子系統中，吾人發現方形四重譜線（square quartet）和量子拍（quantum beating）是費米共振的光譜特徵。除此之外，氣相二維紅外光譜在偵測近紅外光區能態的能力也被仔細討論。接下來在甲基銨離子的研究中，吾人發現費米共振可作為偵測有機－無機混合型鈣鈦礦中甲基銨離子所感受到的微觀環境，像是甲基銨離子和鉛與鹵素晶格間的相互作用力。最後，吾人研究如何將馬可夫假設的模擬技術推展到非馬可夫假設的情況，使模擬方法更接近現實中的物理現象。

doi:10.6342/NTU202404353

關鍵字：量子朗之萬方程式、二維紅外光譜、費米共振、波包動態學、量子拍

doi:10.6342/NTU202404353

Abstract

Two-dimensional infrared (2DIR) spectroscopy has become a powerful tool for probing micoscopic dynamics in the condensed phase over the past two decades. Theoretically, the modern method to simulate 2DIR spectra combines moleclular dynamics simulation and response function calculation. However, this approach often depends on empirical parameters and Newton model mechanism. Thus, the exact treatment of coherent and dissipative dynamics is lacking. In this work, we introduce a dynamical method for the simulation of 2DIR spectra including full coherent quantum dynamics of a molecular system and dissipation involved by the surrounding environment, and then demonstrate the effectiveness of the method by simulating 2DIR spectra of solvated hydronium systems and solvated methylaommonium systems. The dynamical method combines quantum Langevin equation (QLE) and a perturbation scheme that extract phase-matching signals by propagating auxiliary wavefunctions. We present the derivation of the QLE using a linear system-bath coupling model, and show that the quantum Schrödinger-Langevin equation

doi:10.6342/NTU202404353

(QSLE) can be written as a Schrödinger equation with the addition of a friction operator by adopting a Gaussian wavepacket picture. This approach explicitly treat the wavepacket dynamics, including coherent and dissipative dynamics, evolving on the complex potential energy surface. Subsequently, we demonstrate the effectiveness of our method by simulating 2DIR spectra of molecular systems with Fermi resonance phenomenon.

We first demonstrate the QSLE simulation of 2DIR spectra on Ar- and N_2-tagged hydronium system, which exhibits Fermi resonance, and we are interested in revealing 2DIR spectral signatures of Fermi resonance on these systems. The Fermi resonance is a unique feature on infrared spectra that stems from the anharmonic coupling between vibrational modes. However, the discussion of spectral signiture on 2DIR spectra of the Fermi resonance remains under developed. Our simulation reveals that square quartets and the beatings of 2DIR peaks can provide decisive evidence for Fermi resonance in the Ar-tagged system. Moreover, the potential of gas-phase 2DIR spectroscopy is disclosed in probing the states in the near-IR region. Secondly, we apply the QSLE method to the simulation of 2DIR spectra of hydrogen bromide- and chloride- tagged methylammonium (MA), which mimic the micro-environment within the organic-inorganic perovskite (MAPbX3, X is halogen). The simulation indicates a physical insight in which the Fermi resonance occurs in N-H stretching region is sensitive to the intermolecular interactions.

doi:10.6342/NTU202404353

Finally, we conduct the examination of our theoretical method with the non-Markovian friction operator. To validate the new approach, we simulate the dissipative dynamics, infrared and 2DIR spectra of a vibrational mode in an independent oscillator model. The results show that the dissipative dynamics induced by explicit system-bath coupling are manifested in our approach. Therefore, this study demonstrate the effectiveness of QSLE in 2DIR spectroscopic simulation, which is useful for assigning complex 2DIR spectra and provide physical insights.

Keywords: quantum Langevin equation, two-dimensional infrared spectroscopy, Fermi resonance, wavepacket dynamics, quantum beating

doi:10.6342/NTU202404353

doi:10.6342/NTU202404353

Contents

doi:10.6342/NTU202404353

doi:10.6342/NTU202404353

doi:10.6342/NTU202404353

doi:10.6342/NTU202404353

List of Figures

doi:10.6342/NTU202404353

doi:10.6342/NTU202404353

doi:10.6342/NTU202404353

doi:10.6342/NTU202404353

List of Tables

doi:10.6342/NTU202404353

doi:10.6342/NTU202404353

Denotation

QLE	Quantum Langevin Equation
QSLE	Quantum Schrödinger-Langevin Equation
IR	Infrared
FTIR	Fourier Transform Infrared Spectroscopy
2DIR	Two-Dimensional Infrared Spectroscopy
TDSE	Time-Dependent Schrödinger Euqation
PES	Potential Energy Surface
LC Model	Linear Coupling Model
IO Model	Independent-Oscillator Model
MA	Methylammonium

doi:10.6342/NTU202404353

doi:10.6342/NTU202404353

Chapter 1 Introduction

1.1 Infrared spectroscopy

Molecular vibrations arise from the relative motions of atoms within a molecule, providing crucial information about molecular structures. Molecules consist of specific groups of atoms and bonds known as functional groups, which contribute to the chemical properties. These functional groups exhibit characteristic vibrational frequencies, which match the frequencies of infrared (IR) light. A method that utilizes IR light to detect the frequency of molecular vibrations is known as infrared spectroscopy.

Infrared spectroscopy is a valuable technique for identifying molecular structures and studying intermolecular interactions. It works by using IR light to detect vibrational frequencies of molecular vibrations, which can be analyzed to determine the molecular structure. Additionally, the vibrational frequencies can change due to structural alterations or interactions with the surrounding environment. For instance, Heather C. Allen and his co-workers use infrared spectrosocpy to identify hydrogen bonding pattern changed in different hydrogen halide salt solution. [1]

Linear infrared spectroscopy is commonly applied to molecular identification in the gas phase due to a simpler experimental setup. Etienne Garand and his co-workers uses

doi:10.6342/NTU202404353

linear spectraoscopy to study protonated tripeptides in the gas phase.[2] They identified numerous structures of tripeptides composed of glycine and alanine to gain a comprehensive understanding of how local proton affinity changes induced by methyl substitution, affect peptide structures. However, due to the limitation of linear infrared spectroscopy, they can not identify the fluctuations of intramolecular hydrogen bonding patterns, which is also important in the study of peptides.

Nevertheless, the application of linear IR spectroscopy is limited because it only provides information along a single frequency axis. Jheng-Wei Li and his co-worker assign experimental spectra of $H_3O^+Ar_m$ by utilizing *ab initio* vibrational calculation.[3] It is difficult to assign the complicated spectral features of solvated hydroniums in linear spectra without *ab initio* vibrational calculations. Even with the aid of *ab initio* vibrational calculations, assigning Fermi resonance remains challenging in linear IR spectra. Therefore, we choose two-dimensional infrared spectroscopy to study Fermi resonance, which provides two frequency degrees of freedom and time domain information.

1.2 2DIR spectroscopy

Recently, two-dimensional infrared (2DIR) spectroscopy has become a decisive tool in probing ultrafast dynamics and dissipative dynamics of molecular systems. The four-wave mixing process in 2D techniques correlates the absorption and emission frequencies of the system. This technique utilizes femtosecond laser pulses, which provide advantages in investigating ultrafast dynamics in the condensed phase.[4] Moreover, the two-dimensional frequency resolution offers a more comprehensive understanding of potential energy surfaces of chemical systems, enabling easy identification of molecular struc-

doi:10.6342/NTU202404353

tures.[5]

1.2.1 2DIR Experiment

We briefly introduce a typical experimental setup of 2DIR spectroscopy to explain why it has these advantages. Figure.1.1 illustrates a experimental setup of 2DIR spectroscopy, which is known as the box-CARS geometry.[6] The sample interacts with three laser pulses and emits vibrational echo signals in the direction of $k_{echo} = -k_1 + k_2 + k_3$. To extract the signal, the probing pulse of a local oscillator combines with the spectral signal. The schematic diagram of time ordering of laser pulses is shown in Fig.1.2.[7] The time interval between first and second laser pulses is called the coherent time, τ; that between third laser pulse and local oscillator is called the detection time, t. Hence, the Fourier transform is conducted to obtain information in the frequency domain, comprised by ω_τ and ω_t, by scaning the coherent and detection time intervals. Moreover, in 2DIR spectroscopy, the population time, T, which is between second and third pulses, can offer information on ultrafast time scale in chemical dynamics such as vibrational relaxation, spectral diffusion and chemical exchange.

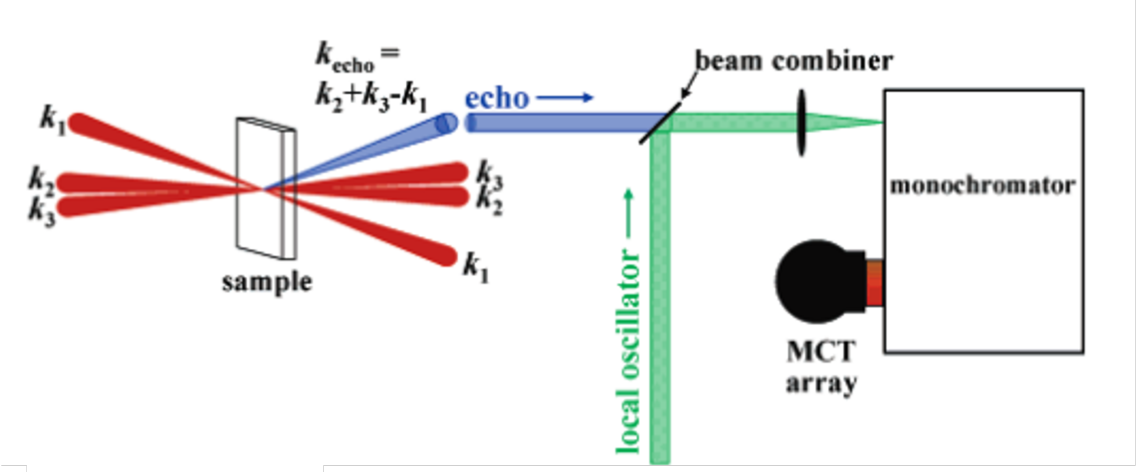

Figure 1.1: The 2DIR experimental setup with box-CARS geometry and heterodyne detection. The figure is taken from Ref.[6].

doi:10.6342/NTU202404353

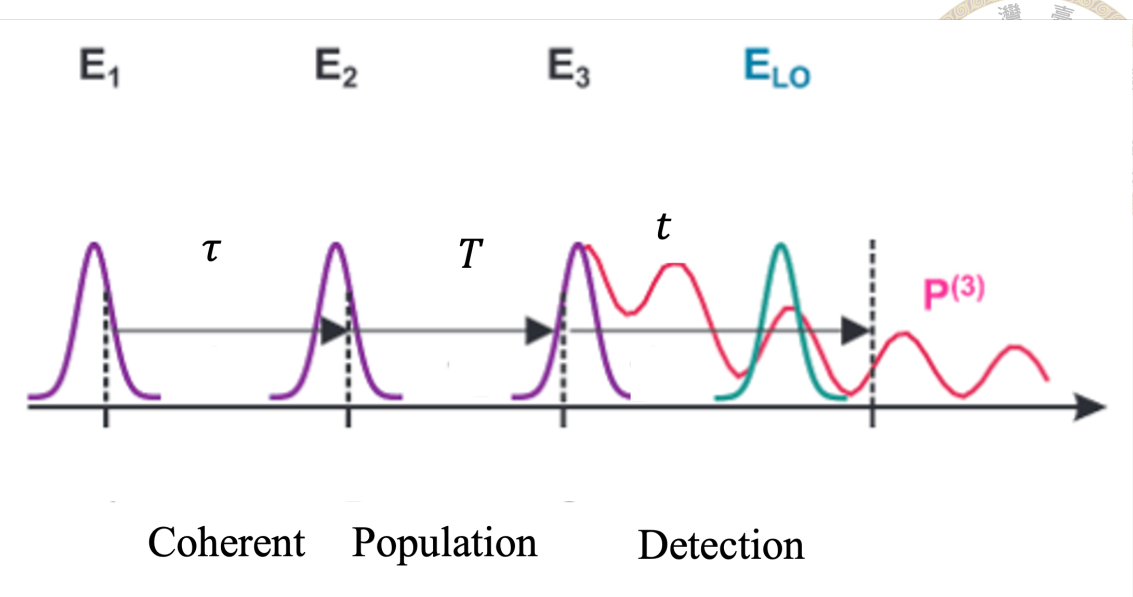

Figure 1.2: The 2DIR schematic figure of laser pulses, which made from the figure taken from Ref.[7].

In addition to structural identification, a 2DIR spectrum gives detailed information about chemical systems, such as vibrational anharmonicity and intermode coupling. These information can be obtain from the patterns of peaks in 2DIR spectra. For instance, Fig.1.3 depicts 2DIR experimental spectra. The 2DIR spectra are shown with the x-axis representing ω_τ and the y-axis representing ω_t. The diagonal peaks (A peaks in Fig.1.3) with positive signals, located at positions where $\omega_\tau = \omega_t$, correspond to the fundamental frequencies of each vibrational mode. The peaks (C peaks in Fig.1.3) surrounding these diagonal peaks with positive signals, known as cross peaks, provide insights into the anharmonic couplings between different vibrational modes. In addition, negative peaks (B peaks in Fig.1.3) stem from the absorptions from first excited states to second excited states which can be identified. Therefore, the negative peaks offer the information of anharmonicity.

doi:10.6342/NTU202404353

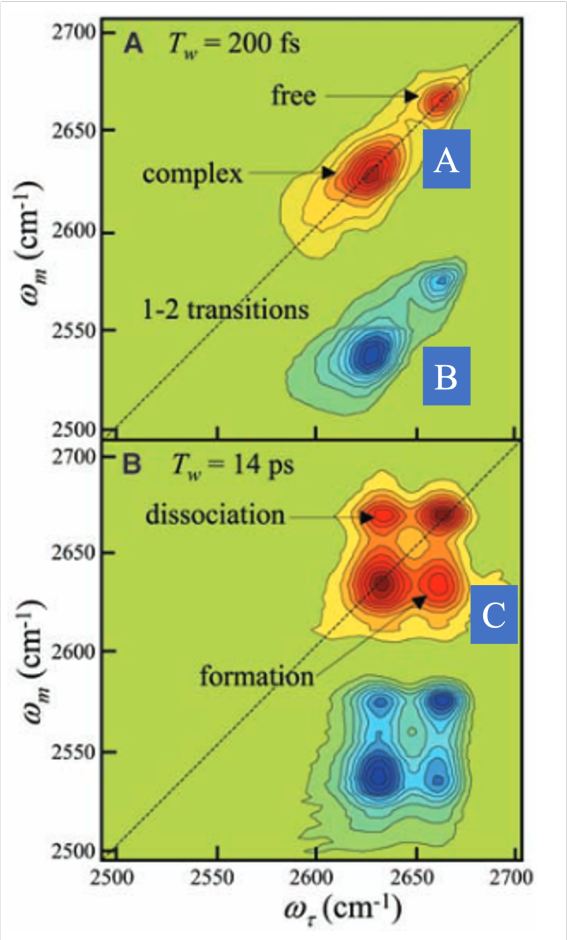

Figure 1.3: 2D IR vibrational echo spectra of the O-D stretch of phenol in the mixed benzene-CCl_4solvent. The figure taken from Ref.[8].

The 2DIR spectraoscopy has been applied on various researches, such as ultrafast chemical dynamics in the condensed phase. For example, Maiti and his co-worker investigate the chemical exchange of hydrogen bonded oligomers in 2-Pyrrolidinone by analyze the cross peaks on 2DIR spectra in the N-H stretching region.[9] They successfully identified the mechanism of hydrogen-bond breaking and formation, which is an ultrafast dynamic process that is difficult to observe using traditional spectroscopic techniques. Chi-Jui Feng et al. conducted 2DIR experiment on dialanine to reveal that that the hydrogen bonding fluctuations can affect the vibrational relaxation and dephasing.[10] On the other hand, 2DIR spectroscopy also can combine with polarization laser pulses which

doi:10.6342/NTU202404353

efficiently probe information in energy levels in the near-IR region in aniline-d_5.[11] In summary, numerous experimental studies with 2DIR technique provide unprecedented results in chemistry.

1.2.2 Theoretical simulation

The development of theoretical method in a spectroscopic technique is also important to provide clear assignment in complicated experimental spectra. The theoretical method for simulating 2DIR spectra is currently based on time-dependent perturbation theory (TDPT). By considering the interaction between light and matter as a perturbation, the signal in 2DIR spectroscopy can be calculated using the third-order polarization. This polarization carries information about the system called the response function. The response function can be visualize by double-sided Feynman diagrams.

Double-sided Feynman diagrams are constructed by presenting field-induced evolution of elements of density matrix in a graphical manner. In Fig.1.4, we show an example of double-sided Feynman diagrams. The horizontal line denotes the time evolution, which defines the order light-matter interactions induced from laser pulses. Each laser pulse is depicted by an arrow. The diagrams illustrate the response function, making them useful for 2DIR spectral assignment.

doi:10.6342/NTU202404353

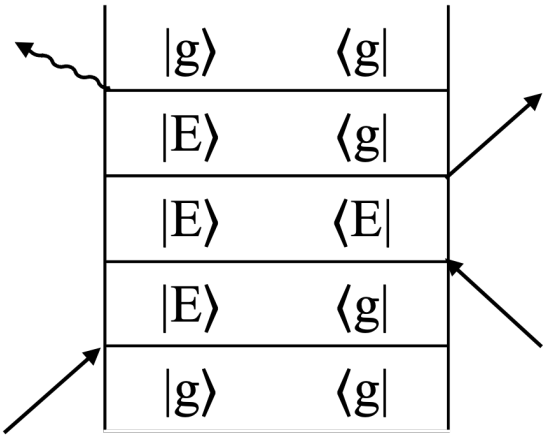

Figure 1.4: An example of a double-sided Feynman diagrams.

In practical applications, the response functions can be calculated either by using simple phonomenological models or by molecular dynamics (MD) simulations.[12, 13] In this approach, it is necessary to calculate the time correlation function of dipole operator for each light-matter interaction pathway to simulate 2DIR spectra.[14] Therefore, it has the merit of a simple extraction of the 2DIR signals at the phase-matching direction.

However, most previous theoretical studies utilized phenomenological model without explicit nuclear dynamics. The explicit nuclear dynamics such as the vibrational relxation and dephasing can change the lineshapes in 2DIR spectra. Moreover, dealing with the convolution between laser pulse envelopes and the response function by numerical integration can be computationally expensive. Therefore, a new theory is needed for providing insight into the experimental results of intricate vibrational coupling and dissipative effects.

The dynamical simulation can handle those issue that naturally includes the overlap of finite-width pulses and propagate the system dynamics induced by three laser pulses. This approach have used in photon-echo spectroscopy and 2D electronic spectroscopy,

doi:10.6342/NTU202404353

which we condider that it is also suitable for 2DIR simulation. The development of a wavefunction-based method to calculate third-order polarizations in multi-dimensional systems was proposed to simulate 2D spectra,[15] which execute with affordable computational cost. The method needs auxiliary wavefunctions to obtain time-resolved optical signals at the photon-echo phase-matching direction. Moreover, the multi-dimensional quantum Schrödinger-Langevin equation (QSLE) approach was used to emphasize the explicit treatment of vibrational relaxation dynamics by incorporating the environmental effects.[16] The explicit vibrational wavepacket dynamics, evolving on the potential energy surface, is propagated and fully captured in the method, which especially includes the coherent dynamics. Hence, this theory has the benefit of dealing with systems which have large dimensions and intricate intermode couplings, and giving detailed descriptions of vibrational relaxation dynamics. In this thesis, we aim to use this theoretical approach to simulate 2DIR spectra and study molecular clusters in the gas phase with Fermi resonance signatures.

1.3 Molecular systems and Fermi resonance

1.3.1 Molecular clusters

Molecular clusters serve as simple models to provide insights into complex chemical systems such as bulk materials. In this work, we study two molecular systems using 2DIR spectroscopy to investigate anharmonic coupling and hydrogen bonds in Fermi resonance systems. For instane, studies on clusters of solvated protons with water molecules elucidate proton defects in the hydrogen-bonding network.[17] The methylammonium tagged with hydrogen haildes offer an insight into hydrogen bonds among hybrid organic-

doi:10.6342/NTU202404353

inorganic perovskites.[18] Moreover, molecular clusters have the advantage of studying intermode anharmonic coupling because of the adjustability of the system properties by changing tagged atoms or molecules.

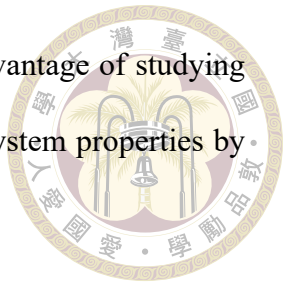

1.3.2 Fermi resonance

Fermi resonance in a vibrational spectroscopy is particularly informative to molecular structures and intermolecular interactions. The first case of Fermi resonance is in the Raman spectrum of CO_2 discovered by Fermi in 1931.[19] Fermi resonance occurs in the accidental energy degenercy between a fundamental tone and an overtone or combination tones coupled by the anharmonic couplings leading to complicated spectral patterns in vibrational spectra. Therefore, the traditional analysis, which relies on the harmonic approximation and uses normal modes to describe vibrational motion in molecules, encounters difficulties in Fermi resonance systems.

2DIR spectroscopy has been utilized to study Fermi resonance. In 2011, Michael W. Nydegger and his co-workers employed 2DIR spectroscopy to identify Fermi resonance between C-D stretching and COD bending in deuterated formic acid dimer .[20] Although they clearly describe the pathways contributing to the spectral patterns induced by Fermi resonance, we believe their simulation is limited in providing detailed information on time-domain evolution. Furthermore, they used eigenenergies extracted from experimental spectra to construct an approximated Hamiltonian with two bright oscillators, which did not provide microscopic nature of the vibrations. Hence, we believe a more advanced study with molecular details and descriptions of time-evolution, where the vibrational wavepacket dynamics is needed.

doi:10.6342/NTU202404353

1.3.3 Hydronium

Structures and properties of a solvated proton represnet an important scientific topic both in chemistry and biology. The debate regarding the presence of Eigen (H_3O^+) or Zundel ($H_5O_2^+$) ions is still ongoing.[5] Hence, it is important to study the hydronium ion (protonated water) in detail to enhance our understanding of hydrogen bonding and proton affinity which is an important factor to determine the presence of Eigen or Zundel ions. Several studies of vibrational spectroscopy focus on the gas-phase cluster of hydronium,[21, 22] and we summarize the relevant results from those studies in the following.

Anne B. McCoy and co-workers in 2012 found that the non-Condon effects in hydronium ion contributes the peaks around 1900-2100 cm^{-1} composed of the combination band involving O-H bending and hindered rotation.[22] The features of Fermi resonance between O-H stretching and bending in Ar-tagged hydronium are identified in the study in 2015 conducted by Jheng-Wei Li and co-workers.[3] Particularly, the intermolecular interaction also affect the vibrational coupling. For example, the species in the first solvation shell of hydronium ion can change the anharmonic coupling between O-H bending and stretching.[23, 24] The spectra measured by gas-phase infrared predissociation (IR-PD) experiment also agrees with the theoretical calculations.[24, 25] Figure.1.5 depicts the frequency change of O-H banding overtone (blue line) and stretching fundamental (red line) when hydroniums are tagged with different molecules.[25] They studies the trend of Fermi resonance between O-H bending and stretching in solvated hydronium ion analyze by the finite basis representation (FBR) Hamiltonian 3×3 Hamiltonian. However, we consider that 2DIR spectra can provide an insight of these trend without conducting anharmonic calculation. Therefore, we aim to study the spectral features of Fermi resonance

doi:10.6342/NTU202404353

in solvated hydronium on 2DIR spectra based on the FBR effective Hamiltonain.

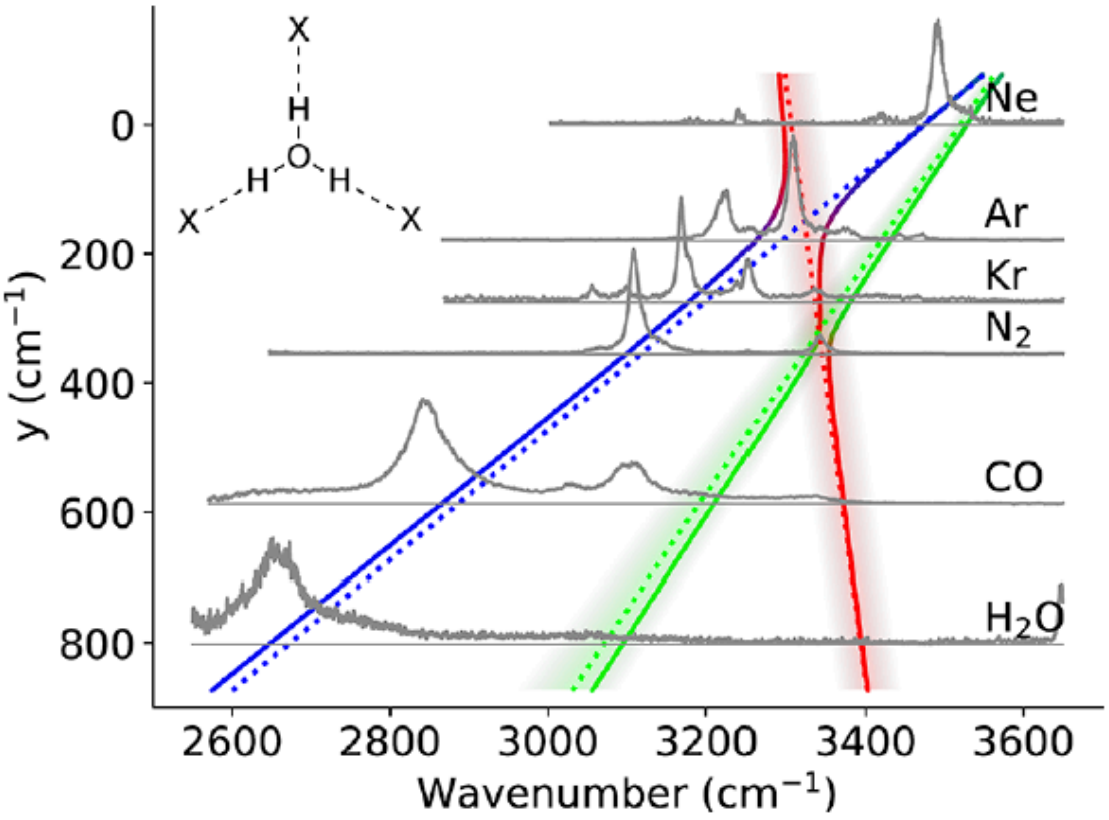

Figure 1.5: The illustration of vibrational couplings and peaks positions between O-H bending (red line), stretching (blue line) and intermolecular stretching (green line).[25].

1.3.4 Methylammonium system

In this subsection, we provide a backfground perspective of a material related to methylammonium (MA), which is an important molecule included in hybrid organic-inorganic peroskites (HOIPs). Hybrid organic-inorganic perovskites have attracted significant interest and exhibited outstanding performance in photovoltaics. HOIPs first were synthesized in 1978.[26] The general chemical formula of HOIPs is ABX_3, where A is an organic cation such as MA, B is a metal cation such as Pb, and X is a halide anion.

HOIPs, like $MAPbBr_3$, have several advantages in material science and photovoltaics.

doi:10.6342/NTU202404353

First, their fabrication is straightforward, typically involving spin-coating techniques using organic and metal salt solutions. In the aspect of photovoltaics, HOIPs excel because they efficiently generate excitons with low binding energies upon light exposure due to their high absorption coefficients. This process subsequently produces free carriers (electrons) with low effective mass, high mobility, and long lifetimes. Additionally, MA provide structural templating for the Pb-Br framework and introduce a permanent dipole, which influences the dielectric properties of the material and its interactions with the Pb-Br network related to the properties of photovoltaics. The above information is extracted from the review articles.[27, 28]

Several research groups have studied IR spectroscopy. The IR spectroscopy is suitable for studying the microscopic environment of organic cations in the inorganic lattice through. In 2015, two groups employed harmonic calculations to provide detailed assignments for the spectral range of 800-1800 cm^{-1} at both low and room temperatures. [29, 30] Additionally, Gotz Schuck and co-workers examined IR spectra, focusing on the tetragonal-orthorhombic phase transition and carefully discussing the changes in spectral features during this transition.[31]

For 2DIR spectrocopy, the rotational motion of MA molecule has been extensively discussed. In 2015, Artem A. Ballin *et al.* discovered the wobbling-in-a-cone and jump-like reorientation motion of MA in lead-iodide perovskites by 2D-IR polarization-resolved spectrocopy in the umbrella mode of NH_3.[32] Furthermore, Oleg Selig and his co-workers examined the relationship between the rotational motion of MA and the mixability of halide atoms.[33]

doi:10.6342/NTU202404353

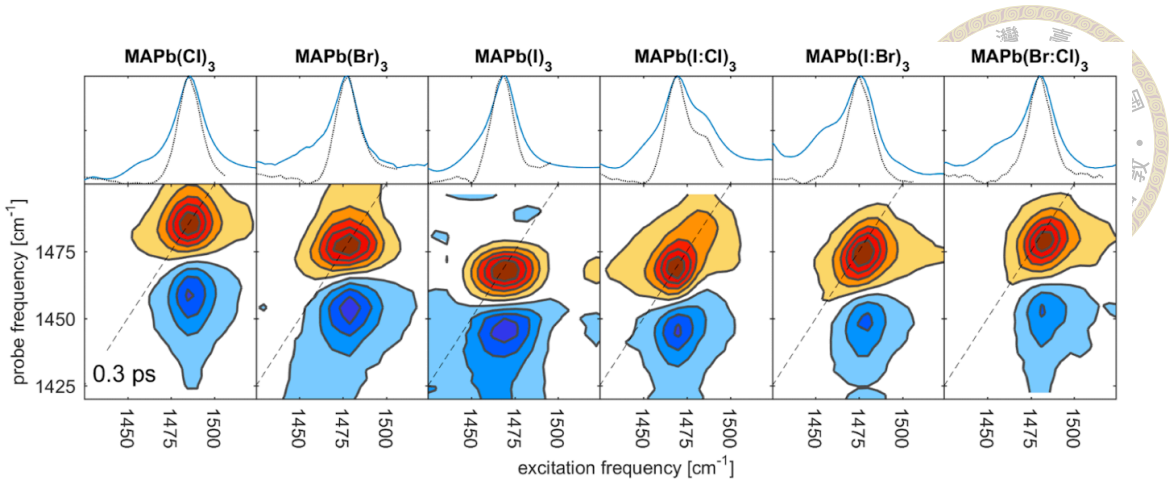

Figure 1.6: Isotropic 2DIR spectra for MA perovskites at a delay of 300 fs. Top: Linear infrared spectrum with blue line and slice along the diagonal of the 2DIR spectrum with black dotted line.[33].

However, the assignment in the stretching region remains unclear, as it is sensitive to the hydrogen bonds between MA and halide atoms. In 2021, Chih-Kai Lin and co-workers indicated that the Fermi resonance occurs in the stretching region of solvated MA system.[18] Moreover, they proposed an approach using hydrogen halide-tagged MA in the gas phase to study the microscopic environment of MA in HOIPs. Therefore, we aim to investigate the halide-tagged MA with a focus on Fermi resonance, which acts as a probe to the microscopic environment of MA in HOIPs. Moreover, the simulation of MA faces a challeng due to numerous vibrational states related to Fermi resonance in stretching region. Our QSLE approach and dynamical simulation can easily deal with the large dimension of Hamiltonian in MA molecules.

1.4 Overview of this work

In this study, we apply the theoretical QSLE approach to calculate the 2DIR spectra of Fermi resonance systems. In Chapter 2, we present the derivation of our theoretical

doi:10.6342/NTU202404353

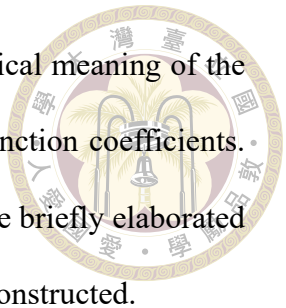

approach, including QLE and SQLE. In addition, we discuss the phsical meaning of the Gaussian wavepacket approximation and the rates related to wavefunction coefficients. Subsequently, the simulation method of IR and 2DIR spectroscopy are briefly elaborated in chapter 3. Hence, a complete picture of our theoretical method is constructed.

In Chpater 4, we investigate the spectral signatures on 2DIR spectra by examining the Ar and N_2-tagged hydronium systems. First, the N_2-tagged hydronium is expected to exhibit a uncoupled vibrational modes on 2DIR spectra. By comparsion, the Ar-tagged hydronium, where the Fermi resonance perfectly happens, can offer obvious spectral signtures. Then, the hydrogen halide-tagged methylammonium is studied with a focus on the benefit that spectral signatures of Fermi resonance on 2DIR spectra can provide. We starts from $(HBr)_3$ and $(HCl)_3$-tagged MA systems, where the cluster obey C_{3V} symmetry, to fully understand the spectra in these systems in chpater 5. Ultimately, the mixing tagged MA,$(HBr)_1(HCl)_2$-tagged MA, is investigated. We analyze those difference from the signals oscillating in the population time period and provide the insight on microscopic environment of MA in HOIPs. In Chapter 6, we validate the non-Markovian quantum Langevin equation in a harmonic oscillator. Finally, in Chpater 7, we will summarize the results found in previous chpater and highlight the importance in this thesis.

doi:10.6342/NTU202404353

Chapter 2 Quantum Schrödinger-Langevin Equation Approach

The exact treatment explicit nuclear dynamics in the approach follows the previous study conducted by Joshua M. Jackson *et al.*.[34] In this chapter, we aim to summarize the derivation of the quantum Langevin equation (QLE). Subsequently, the method of propagating dissipative dynamics in the Schrödinger picture, known as ”quantum Schrödinger-Langevin equation (QSLE) approach” under the Markovian limit will be included. Finally, we will discuss the rate of vibrational relaxation induced by the QSLE approach.

2.1 Derivation of the quantum Langevin equation

We start with the independent-oscillator (IO) model, in which a system is coupled to bath mode through the displacement operator. The derivation follows these paper.[35, 36] Here, the total Hamiltonian is

$$H = \frac{p^2}{2m} + V(x) + \sum_{\alpha} [\frac{p_\alpha^2}{2m_\alpha} + \frac{1}{2} m_\alpha \omega_\alpha^2 (q_\alpha - x)^2] \tag{2.1}$$

doi:10.6342/NTU202404353

where m, p, x and $V(x)$ represent the mass, momentum operator, position operator and potential of the system, respectively. Moreover, m_α, p_α and q_α is the mass, momentum operator and position operator of the αth of collective bath modes, respectively. The system is a single vibrational mode with the potential $V(x)$ and the bath (surrounding) is composed of collective harmonic modes.

$$\frac{dA(t)}{dt} = \frac{i}{\hbar}[H(t), A(t)] \tag{2.2}$$

Here, we utilize the formula for the time derivative of operators ($A(t)$) in the Heisenberg picture, where H(t) is a total Hamiltonian including the system and bath.

$$\begin{aligned} \frac{dx(t)}{dt} &= \frac{i}{\hbar}[H(t), x(t)] = \frac{p(t)}{m} \\ \frac{dp(t)}{dt} &= \frac{i}{\hbar}[H(t), p(t)] = -V'(x) + \sum_\alpha g_\alpha m_\alpha \omega_\alpha^2 (q_\alpha(t) - g_\alpha x(t)) \end{aligned} \tag{2.3}$$

Here, we obtain the time derivative of position and momentum operator. It is worth noting that the system is acted a force from the system-bath coupling manifesting in the time derivative of momentum operator.

$$\begin{aligned} \frac{dq_\alpha(t)}{dt} &= \frac{i}{\hbar}[H(t), q_\alpha(t)] = \frac{p_\alpha(t)}{m_\alpha} \\ \frac{dp_\alpha(t)}{dt} &= \frac{i}{\hbar}[H(t), p_\alpha(t)] = -m_\alpha \omega_\alpha^2 (q_\alpha(t) - g_\alpha x(t)) \end{aligned} \tag{2.4}$$

In the two equation, the equation of motion (EOM) of the αth bath mode is captured. The motions of the system and bath modes are closely intertwined. Therefore, we obtain the time derivative of the position and momentum operators for both the system and bath modes to derive the EOM.

doi:10.6342/NTU202404353

By eliminating the momentum variables, we can obtain

$$m\frac{d^2x(t)}{dt^2} + V'(x) = \sum_\alpha g_\alpha m_\alpha \omega_\alpha^2 (q_\alpha(t) - g_\alpha x(t))$$
$$\frac{d^2q_\alpha(t)}{dt^2} + \omega_\alpha^2 q_\alpha(t) = g_\alpha \omega_\alpha^2 x(t) \tag{2.5}$$

To focus on the system only, we need to obtain $q_\alpha(t)$ and substitute it into the EOM of the system to reduce the degrees of freedom associated with the bath modes. Therefore, we perform a Laplace transform on the EOM of the bath transition from the time domain (t) to the Laplace domain (s).

$$s^2Q_\alpha(s) - sq_\alpha(0) - \frac{dq_\alpha(0)}{dt} + \omega_\alpha^2 Q_\alpha(s) = g_\alpha \omega_\alpha^2 X(s) \tag{2.6}$$

Then, we arrange the equation.

$$Q_\alpha(s) = \frac{1}{s^2 + \omega_\alpha^2}\{sq_\alpha(0) + \frac{p_\alpha(0)}{m_\alpha} + g_\alpha \omega_\alpha^2 X(s)\} \tag{2.7}$$

Here, $Q(s)$ represents the Laplace transform of $q(t)$, and $X(s)$ represents the Laplace transform of $x(t)$, respectively. Subsequently, we take the inverse Laplace transform on Eq.2.7.

$$q_\alpha(t) = cos(\omega_\alpha t)q_\alpha(0) + sin(\omega_\alpha t)\frac{p_\alpha(0)}{m_\alpha \omega_\alpha} + \int_0^t g_\alpha \omega_\alpha sin(\omega_\alpha(t-\tau))x(\tau)d\tau \tag{2.8}$$

Finally, we can obtain the EOM, which only includes the varibles of the system. Subsequently, we substitute $q_\alpha(t)$ into the the EOM of system.

$$m\frac{d^2x(t)}{dt^2} + V'(x) = \sum_\alpha [g_\alpha m_\alpha \omega_\alpha^2 \cos(\omega_\alpha t)q_\alpha(0) + g_\alpha \omega_\alpha \sin(\omega_\alpha t)p_\alpha(0)]$$
$$+ \int_0^t \sum_\alpha g_\alpha^2 m_\alpha \omega_\alpha^3 \sin(\omega_\alpha(t-\tau))x(\tau)d\tau - \sum_\alpha g_\alpha^2 m_\alpha \omega_\alpha^2 x(t) \tag{2.9}$$

doi:10.6342/NTU202404353

To derive the standard form of the quantum Langevin equation, we apply the integration by part on Eq.2.9.

$$\begin{aligned}
&\int_0^t \sum_\alpha g_\alpha^2 m_\alpha \omega_\alpha^3 \sin(\omega_\alpha(t-\tau))x(\tau)d\tau \\
&= \sum_\alpha \{g_\alpha^2 m_\alpha \omega_\alpha^2 x(\tau)[cos(\omega_\alpha(t-\tau))]_0^t - \int_0^t g_\alpha^2 m_\alpha \omega_\alpha^2 cos(\omega_\alpha(t-\tau))\dot{x}(\tau)\} \\
&= \sum_\alpha \{g_\alpha^2 m_\alpha \omega_\alpha^2 x(t) - g_\alpha^2 m_\alpha \omega_\alpha^2 x(0) cos(\omega_\alpha(t)) - \int_0^t g_\alpha^2 m_\alpha \omega_\alpha^2 cos(\omega_\alpha(t-\tau))\dot{x}(\tau)\}
\end{aligned} \tag{2.10}$$

By substituting Eq.2.10 into Eq.2.9, we obtain

$$\begin{aligned}
&m\frac{d^2x(t)}{dt^2} + V'(x) = f(t) - \eta(t)x(0) - \frac{1}{m}\int_0^t \eta(t-\tau)p(\tau) \\
&f(t) = \sum_\alpha \left[g_\alpha m_\alpha \omega_\alpha^2 \cos(\omega_\alpha t)q_\alpha(0) + g_\alpha \omega_\alpha \sin(\omega_\alpha t)p_\alpha(0)\right] \\
&\eta(t) = \sum_\alpha g_\alpha^2 m_\alpha \omega_\alpha^2 cos(\omega_\alpha(t)) \\
&\dot{x}(t) = \frac{p(\tau)}{m}
\end{aligned} \tag{2.11}$$

The equation is the standard form of the quantum Langevin equation (QLE), where $f(t)$ and $\eta(t)$ is the random force and friction kernel, respectively.

2.2 Quantum Schrödinger-Langevin equation approach

In 2011, Joshua M. Jackson and his co-workers proposed a qunatum Schrödinger-Langevin equation (QSLE) approach that can be easily implemented.[34] Therefore, we follow the way to cast the quantum Schrödinger-Langevin equation.

doi:10.6342/NTU202404353

2.2.1 Gaussian wave packet approximation

In the previous section, we have derived the EOM in the Heisenberg picture. However, we aim to manifest the EOM by propagating the time-dependent Schrödinger equation (TDSE), namely in the Schrödinger picture,

$$\begin{aligned} i\hbar\frac{\delta\psi(x,t)}{\delta t} &= H\psi(x,t) \\ H &= \sum_i \frac{p_i^2}{2m_i} + V(x) \end{aligned} \tag{2.12}$$

where the system with the wavefunction ($\psi(x,t)$) contains a vibrational mode with an index i.

$$\begin{aligned} V(x) = V_0 + \sum_i V_{x,i}(x_i - \langle x_i\rangle(t)) + \frac{1}{2}V_{xx,ii}(x_i - \langle x_i\rangle(t))^2 \\ + \sum_{j\neq i}\frac{1}{2}V_{xx,ij}(x_i - \langle x_i\rangle(t))(x_j - \langle x_j\rangle(t)) \end{aligned} \tag{2.13}$$

Here, we expand the potential $V(x)$ to the second order. V_0, $V_{x,i}$, $V_{xx,ii}$ correspond to zero-point energy, the first differential of PES in the ith dimension and the second differential of PES in the ith dimension,respectively. Subsequently, we assume that the wavefunction is a multi-dimensional Gaussian wave packet, known as Gaussian wave packet (GWP) approximation,

$$\begin{aligned} \psi(x,t) = & Cexp\{\frac{i}{\hbar}\sum_i \alpha_{ii}(t)(x_i - \langle x_i\rangle(t))^2 \\ & + \sum_{j\neq i}\beta_{ij}(t)(x_i - \langle x_i\rangle(t))(x_j - \langle x_j\rangle(t)) \\ & + \langle p_i\rangle(t)(x_i - \langle x_i\rangle(t)) + \gamma(t)\} \end{aligned} \tag{2.14}$$

doi:10.6342/NTU202404353

where C is the amplitude of the wave packet, $\langle x_i \rangle(t)$ corresponds to the center of the wave packet, the $\alpha_{ii}(t)$,$\beta_{ii}(t)$ are related to the width and distortion between dimensions of the wave packet, and $\gamma(t)$ is a time-dependent phase.

By substituting Eq.2.14 into Eq.2.12, several equations of motion can be obtained. In this work, we only consider the EOM related to the displacement $(x_i - \langle x_i \rangle(t))$ of the wave packet, which means the forces acting on the wave packet.

$$2\alpha_{ii}(t)\langle \dot{x}_i \rangle(t) - \langle \dot{p}_i \rangle(t) + \beta_{ii}(t)\langle \dot{x}_i \rangle(t) = \frac{2}{m_i}\alpha_{ii}(t)\langle p_i \rangle(t) + V_{x,i} \tag{2.15}$$

where the left-hand side is generated from the time derivative of the wavefunction, and the right-hand side is derived from the Hamiltonian. According to Eq.2.15, we find

$$\begin{aligned} \langle \dot{x}_i \rangle(t) &= \frac{\langle p_i \rangle(t)}{m_i} \\ -\langle \dot{p}_i \rangle(t) &= -\beta_{ij}(t)\langle \dot{x}_j \rangle(t) + V_{x,i} \end{aligned} \tag{2.16}$$

where the $-\beta_{ij}(t)\langle \dot{x}_j \rangle(t)$ denotes that the other modes can influence the force acting on i$^{\text{th}}$ mode through momentum. Now we return to Eq.2.11, take expectation values and rewrite that

$$-m_i\langle \ddot{x}_i(t) \rangle = -\langle \dot{p}_i \rangle(t) = \langle V'(x) \rangle(t) - f_i(t) - \int_0^t \eta_i(t-\tau)\langle p_i \rangle(\tau)d\tau - \eta(t)x(0) \tag{2.17}$$

We can observe and the friction kernel generated from the system-bath coupling would alter the time derivative of momentum observable. Therefore, we combine these terms with the displacement $(x_i - \langle x_i \rangle(t))$ of the wavepacket to formulate the friction operator $F_i(t)$ associated with the ith dimension, where expecting the procedure can reproduce the expectation value of QLE in the wavepacket dyanmics.

doi:10.6342/NTU202404353

$$F_i(t) = [-f_i(t) + \int_0^t \eta_i(t-\tau)\langle p_i\rangle(\tau)d\tau + \eta(t)x(0)](x_i - \langle x_i\rangle(t)) \tag{2.18}$$

and add that to the right-hand side of TDSE.

For simplicity, we can apply the Markovian approximation. The meaning of Markovian approximation is that the EOM of the system is not related to the history of the system becuase we assume the evolution of bath modes is extremely fast than the system. Under the Markovian approximation, the friction operator can expressed as

$$F_i(t) = [-f_i(t) + \eta_M p_i(t)](x_i - \langle x_i\rangle(t)) \tag{2.19}$$

where η_M is the friction coefficient. In the end, the dissipative dynamics, which is approached by the quantum Langevin equation, can be propagated in the Schrödinger picture, calling the quantum Schrödinger-Langevin equation (QSLE) approach, by

$$i\overline{h}\frac{\delta\psi(x,t)}{\delta t} = [H + \sum_i F_i(t)]\psi(x,t) \tag{2.20}$$

To explore the dyanmics underlying the Gaussian wave packet approximation, here, we investigate the physical meaning of the EOM within the GWP approximation. In section 2.2.1, we have derived the EOM of Gaussian wave packet by substituting it into TDSE. However, the EOM related to the displacement of wave packet is discussed only. Therefore, we begin to discuss the physical meaning of other EOM. First, the EOM related to $(x_i - \langle x_i\rangle(t))^2$ is

$$-\dot{\alpha}_{ii}(t) = \frac{2}{m_i}\alpha_{ii}^2(t) + \frac{1}{2}V_{xx,ii} \tag{2.21}$$

doi:10.6342/NTU202404353

where α_{ii} represents the width of wave packet and $V_{xx,ii}$denotes the curvature of PES of the system in ith dimension (harmonic frequency). Therefore, the evolutiono of width is related to the curvature of potential energy surface (PES) in the ith dimension or the harmonic frequency of the ith vibrational mode. Second, the displacement in the jth dimension $(x_j - \langle x_j \rangle(t))$ $(j \neq i)$ is associated with

$$\beta_{ij}(t)\langle \dot{x}_i \rangle(t) = \frac{1}{m_i}\beta_{ij}(t)\langle p_i \rangle(t) \tag{2.22}$$

which means that the i[th] mode can exert a force on the other j[th] modes through the observable of momentum operator. Finally, $(x_i - \langle x_i \rangle(t))(x_j - \langle x_j \rangle(t))$ links to

$$-\beta_{ij}(t) = \frac{2}{m_i}\alpha_{ii}(t)\beta_{ij}(t) + \frac{1}{2}V_{xx,ij} \tag{2.23}$$

indicating that the anharmonic couplings $V_{xx,ij}$ between different modes of PES correlate with the evolution of the distortion of wave pakcet. In conclusion, we summarize the physical meaning of each EOM of Gaussian wave packet propagated in the Schrödinger picture.

2.2.2 The rate of vibrational relaxation and decoherence

Relaxation and decoherence dynamics induced form the friction operator defined in Eq.2.19 and Eq.2.20 remains unclear. Therefore, to clearly elucidate, we will investigate the rate equation of vibrational relaxation in this section.

The following derivaiton will be restricted to single harmonic oscillator system in the Markovian limit. To obtain the time derivative of the coefficients of the wavefunction, we

doi:10.6342/NTU202404353

derive from the TDSE,

$$i\bar{h}\frac{\delta\psi(x,t)}{\delta t} = [H + F(t)]\psi(x,t) \tag{2.24}$$

Here, we expanse the wavefunction $\psi(x,t)$ into a basis the eigenstates of a harmonic oscillator $|n\rangle$.

$$\psi(x,t) = \sum_n c_n |n\rangle \tag{2.25}$$

The Hamiltonian and friction operator of system with single harmonic vibrational mode can be expressed as

$$\begin{aligned} H &= \frac{p^2}{2m} + \frac{1}{2}m\omega^2 x^2 \\ F(t) &= \gamma(t)(x - \langle x\rangle(t)) \\ \gamma(t) &= -f(t) + \frac{\eta}{m}\langle p\rangle(t) \end{aligned} \tag{2.26}$$

where $\gamma(t)$ denotes the friction kernel. Subsequently, the wavefunction is multiplied by a bra $\langle m|$ to extract the time derivative of the coefficient of $|m\rangle$.

$$\begin{aligned} \langle m| i\bar{h}\sum_n \dot{c}_n(t)|n\rangle &= \langle m|[H + F(t)]\sum_n c_n(t)|n\rangle \\ i\bar{h}\dot{c}_m(t) &= \sum_n c_n(t)[\langle m|H|n\rangle + \langle m|F(t)|n\rangle] \\ i\bar{h}\dot{c}_m(t) &= c_m(t)\epsilon_m + \sum_n c_n(t)\langle m|F(t)|n\rangle \end{aligned} \tag{2.27}$$

doi:10.6342/NTU202404353

Then, the $\sum_n \langle m| F(t) |n\rangle$ can be derived as

$$\begin{aligned}\sum_n \langle m| F(t) |n\rangle &= \sum_n c_n(t)\gamma(t)(\langle m| x |n\rangle - \langle x\rangle(t) \langle m|n\rangle) \\ &= \sum_n c_n(t)\gamma(t)(\sqrt{\frac{\hbar}{2m\omega}} \langle m| (a^\dagger + a) |n\rangle - \langle x\rangle(t) \langle m|n\rangle) \\ &= \sum_n c_n(t)\gamma(t)(\sqrt{\frac{\hbar}{2m\omega}}[\sqrt{n+1} \langle m|n+1\rangle + \sqrt{n} \langle m|n-1\rangle] \\ &\quad - \langle x\rangle(t) \langle m|n\rangle) \\ &= \gamma(t)(\sqrt{\frac{\hbar}{2m\omega}}[c_{m-1}(t)\sqrt{m} + c_{m+1}(t)\sqrt{m+1}] - c_n(t)\langle x\rangle(t))\end{aligned} \tag{2.28}$$

Therefore, we can obtain the time derivative of $c_m(t)$ and $c_m^*(t)$

$$\begin{aligned}\dot{c}_m(t) =& -\frac{i}{\hbar}c_m(t)\epsilon_m \\ &- \frac{i}{\hbar}\gamma(t)(\sqrt{\frac{\hbar}{2m\omega}}[c_{m-1}(t)\sqrt{m} + c_{m+1}(t)\sqrt{m+1}] - c_m(t)\langle x\rangle(t)) \\ \dot{c}_m^*(t) =& \frac{i}{\hbar}c_m(t)^*\epsilon_m \\ &+ \frac{i}{\hbar}\gamma(t)(\sqrt{\frac{\hbar}{2m\omega}}[c_{m-1}^*(t)\sqrt{m} + c_{m+1}^*(t)\sqrt{m+1}] - c_m^*(t)\langle x\rangle(t))\end{aligned} \tag{2.29}$$

To understand the rate of change of population and coherence, we introduce a density matrix, which can be formed from the wavefuntion, to describe a pure quantum state. (We

doi:10.6342/NTU202404353

show the quantum states to the 2nd in the array.)

$$\begin{aligned}\rho(t) &= |\psi(t)\rangle \langle\psi(t)| \\ &= \sum_{n,m} c_n(t)c_n^*(t) |n\rangle \langle m| \\ &= \begin{bmatrix} c_0(t)c_0^*(t) & c_1(t)c_0^*(t) & c_2(t)c_0^*(t) \\ c_0(t)c_1^*(t) & c_1(t)c_1^*(t) & c_2(t)c_1^*(t) \\ c_0(t)c_2^*(t) & c_1(t)c_2^*(t) & c_2(t)c_2^*(t) \end{bmatrix} \\ &= \begin{bmatrix} \rho_{00} & \rho_{10} & \rho_{20} \\ \rho_{01} & \rho_{11} & \rho_{21} \\ \rho_{02} & \rho_{12} & \rho_{22} \end{bmatrix}\end{aligned} \tag{2.30}$$

Then, the change of the population of ground state can be derived

$$\begin{aligned}\frac{d\rho_{00}}{dt} &= \frac{dc_0(t)}{dt}c_0^*(t) + c_0(t)\frac{dc_0^*(t)}{dt} \\ &= -\frac{i}{\hbar}\gamma(t)\sqrt{\frac{\hbar}{2m\omega}}c_1(t)c_0^*(t) + c_0(t)\frac{i}{\hbar}\gamma(t)\sqrt{\frac{\hbar}{2m\omega}}c_0(t)c_1^*(t) \\ &= i\gamma(t)\sqrt{\frac{1}{2\hbar m\omega}}(-\rho_{10} + \rho_{01})\end{aligned} \tag{2.31}$$

Similarly, the change of the population of 1st state can also be obtained.

$$\frac{d\rho_{11}}{dt} = i\gamma(t)\sqrt{\frac{1}{2\hbar m\omega}}(-\sqrt{2}\rho_{21} + \sqrt{2}\rho_{12} + \rho_{10} - \rho_{01}) \tag{2.32}$$

and the change of coherence is shown here.

$$\begin{aligned}\frac{d\rho_{10}}{dt} &= -i(E_1 - E_0)\rho_{10} + i\gamma(t)\sqrt{\frac{1}{2\hbar m\omega}}(\rho_{11} - \rho_{00}) - i\gamma(t)\sqrt{\frac{1}{\hbar m\omega}}\rho_{20} \\ \frac{d\rho_{01}}{dt} &= -i(E_1 - E_0)\rho_{01} - i\gamma(t)\sqrt{\frac{1}{2\hbar m\omega}}(\rho_{11} - \rho_{00}) + i\gamma(t)\sqrt{\frac{1}{\hbar m\omega}}\rho_{02}\end{aligned} \tag{2.33}$$

From Eq.2.32, a key point is that if we set the initial state to be a pure quantum state (not superposition), the rates would become zero, resulting in non-dissipative dynamics. The

doi:10.6342/NTU202404353

vibration relaxation is assisted from the off-diagonal term in the density matrix. In summary, we investigate the relaxation and decoherence rate induced by the friciton operator in this section.

2.3 Effective Hamiltonian

The effective Hamiltonian is supplied from Prof. Kuo's group in the institute of atomic and molecular sciences academia sinica. They have published their method in 2018 and 2020 with a assigning study of the infrared predissociation spectra of solvated hydronium clusters.[24, 25] Moreover, the method calculating the theoretical solvated methylammonium cluster are also published showing a good agreement with lead-bromide MA perovskite.[18] Therefore, we use the effective Hamiltonians which has been validated in previous studies. The detailed description of constructing effective Hamiltonian is attached in appendix 7. The matrices of effective Hamiltonian and dipole are in appendix 7.

doi:10.6342/NTU202404353

Chapter 3 Theoretical Method for the Simulation of Linear and Two-dimensional Infrared Spectroscopy

In this section, we would summarize the theoretical method to calculate a linear and 2DIR spectrum. The detailed introduction of time-dependent perturbation theory and fundamental knowledge of double-sided Feynman diagram are attached in Appendix.B and Appendix.D, respectively.

3.1 Linear spectroscopy

In infrared spectroscopy, the time interval between two laser pulses is scanned to capture signals in the time domain. Under the electric point dipole approximation, $V(t)$ can be represented as

$$V(t) = -\hat{\mu} \cdot \boldsymbol{E}(t) \tag{3.1}$$

doi:10.6342/NTU202404353

From Appendix.B.8, we treat light-matter interaction as a perturbation and the nth order wavefunction can be denoted as

$$\begin{aligned}&\left|\psi^{(n)}(t)\right\rangle \\ &=(-\frac{i}{\hbar})^n\int_{t_0}^{t}d\tau_n\int_{t_0}^{\tau_n}d\tau_{n-1}\cdots\int_{t_0}^{\tau_2}d\tau_1 U_0(t,t_0)V(\tau_n)V(\tau_{n-1})\cdots V(\tau_1)\left|\psi(t_0)\right\rangle\end{aligned} \tag{3.2}$$

To describe the signals in linear infrared spectroscopy, the first order polariztion need to be discussed. By definition, the first order polarization can be expressed as

$$P^{(1)}(t)=\left\langle\psi^0(t)\right|\hat{\mu}\left|\psi^{(1)}(t)\right\rangle+\left\langle\psi^{(1)}(t)\right|\hat{\mu}\left|\psi^0(t)\right\rangle \tag{3.3}$$

According to Appendix.B.3, if we propagate an auxiliary wavefunction $|\psi_1(t)\rangle$ with $H(t)=H_0+V(t)$, we obtain a wavefunction containing multiple orders of interaction with light. Under the assumption of weak field conditions, higher-order wavefunctions can be disregarded.

$$\begin{aligned}i\hbar\frac{\partial}{\partial t}\left|\psi_1(t)\right\rangle&=\left[H_0+V(t)\right]\left|\psi_1(t)\right\rangle \\ &=\sum_n\left|\psi^{(n)}(t)\right\rangle \\ &=\left|\psi^0(t)\right\rangle+\left|\psi^{(1)}(t)\right\rangle+O(n\geq 2)\end{aligned} \tag{3.4}$$

Consequently, the first-order wavefunction $\left|\psi^{(1)}(t)\right\rangle$ can be derived by subtracting the zero-order wavefunction.

$$\left|\psi^{(1)}(t)\right\rangle=\left|\psi_1(t)\right\rangle-\left|\psi^0(t)\right\rangle \tag{3.5}$$

The zero-order wavefunction can be obtained by propagating a auxiliary wavefunction

doi:10.6342/NTU202404353

with H_0 only.

$$i\hbar\frac{\partial}{\partial t}\left|\psi_0(t)\right\rangle = H_0\left|\psi_0(t)\right\rangle$$
$$\left|\psi^0(t)\right\rangle = \left|\psi_0(t)\right\rangle \tag{3.6}$$

In summary, the spectral signals of linear spectroscopy cam be obtained by propagating two auxiliary wavefunctions. Finally, in linear spectroscopy, the corrsponding spectrum is obtained by the Fourier transform.

$$S(\omega) \sim \int_0^\infty dt e^{-i\omega t} \times iP^{(1)}(t), \tag{3.7}$$

3.2 Two-dimensional infrared spectroscopy

Two-dimensional infrared spectroscopy is a technique related to nonlinear optics, an experiment that involves three laser pulses interacting with the sample to generate polarization and the signal in the phase matching direction.[12] The signal is Fourier-transformed with respect to the coherence time τ (the time interval between the first and second pulses) and the detection time t (the time interval between the third pulse and the signal) to obtain the 2D infrared spectrum at a certain population time T (the time interval between the second and third pulses). Under the electric point dipole approximation, $V(t)$ can be represented as

$$\begin{aligned} V(t) &= -\hat{\mu}\cdot\boldsymbol{E}(t) \\ &= -\hat{\mu}\cdot\sum_{a=1}^{3}\Lambda_a(t,\tau_a)[exp(i\boldsymbol{k}_a\cdot\boldsymbol{r}-i\omega_a(t-\tau_a))+c.c.] \end{aligned} \tag{3.8}$$

Here, $\boldsymbol{E}(t)$ is the time-dependent electric field of laser pulses. The laser pulse denotes as its envelope $\Lambda_a(t)$, wavevector $\boldsymbol{k}$, central frequency ω, and pulse central time τ_a. $\hat{\mu}$ is the transition dipole operator written as

doi:10.6342/NTU202404353

$$\hat{\mu} = \sum_{i} \sum_{[k'|\varepsilon_{k'} > \varepsilon_k]} \mu_{kk'} \left|k\right\rangle \left\langle k'\right| + \mu_{k'k} \left|k'\right\rangle \left\langle k\right| \equiv X + X^{\dagger} \tag{3.9}$$

where $\mu_{kk'}$ is the transition dipole moment between state k and k' with energy $\varepsilon_{k'} > \varepsilon_k$. We adjust the transition dipole operator that is separated into the excitation part X and the de-excitation part $X^{\dagger}$. Using the fact that the photo-induced excitation and de-excitation are related to the direction of the wave vector, the excitation part X (the de-excitation part $X^{\dagger}$) of ket (bra) is associated with the $+\boldsymbol{k}$-component ($-\boldsymbol{k}$-component) of the laser field.

In our theoretical method, the wavefunctions are propagated to generate 2DIR spectral signals. By definition, the third-order polarixation is

$$P^{(3)}(t) = \sum_{m=0}^{3} \left\langle \psi^{(3-m)}(t) \right| \hat{\mu} \left| \psi^{(m)}(t) \right\rangle \tag{3.10}$$

Gelin *et al.* showed that the third-order polarization could be described by calculating the time evolution of auxiliary wavefunctions $|\psi_{a^{(\dagger)}b^{(\dagger)}c^{(\dagger)}}(\boldsymbol{r}, t)\rangle$ defined by the following form.

$$i\bar{h}\frac{\partial}{\partial t} \left|\psi_{a^{(\dagger)}b^{(\dagger)}c^{(\dagger)}}(\boldsymbol{r}, t)\right\rangle = [H - aV_1^{(\dagger)}(t) - bV_2^{(\dagger)}(t) - cV_3^{(\dagger)}(t)] \times \left|\psi_{a^{(\dagger)}b^{(\dagger)}c^{(\dagger)}}(\boldsymbol{r}, t)\right\rangle \tag{3.11}$$

where a, b, c are integers of either 0 or 1 representing the times of interacting with the laser 1, 2, and 3. The $V_a(t)$ is the combination of the wavevector's effect and the operator $X(X^{\dagger})$.

$$V_a(t) = \Lambda_a(t, \tau_a) exp(-i\omega_a(t - \tau_a)) \cdot X \tag{3.12}$$

where $\Lambda_a(t, \tau_a)$, ω_a and τ_a denote envelope, central frequency and pulse center time, respectively. In 2DIR spectroscopy, the wavevector of laser pulses should satisfy the phase-

doi:10.6342/NTU202404353

matching condition $\boldsymbol{k} = -\boldsymbol{k}_1 + \boldsymbol{k}_2 + \boldsymbol{k}_3$ and the third-order polarization becomes

$$\begin{aligned} P_{PE}^{(3)}(t) = &\left\langle \phi_{101^\dagger}^{(2)}(t) \middle| X \middle| \phi_{01^\dagger 0}^{(1)}(t) \right\rangle + \left\langle \phi_{11^\dagger 0}^{(2)}(t) \middle| X \middle| \phi_{001^\dagger}^{(1)}(t) \right\rangle \\ &+ \left\langle \phi_{000}^{(0)}(t) \middle| X \middle| \phi_{11^\dagger 1^\dagger}^{(3)}(t) \right\rangle + \left\langle \phi_{100}^{(1)}(t) \middle| X \middle| \phi_{01^\dagger 1^\dagger}^{(2)}(t) \right\rangle \end{aligned} \tag{3.13}$$

$\left| \phi_{a^{(\dagger)}b^{(\dagger)}c^{(\dagger)}}^{(n)}(t) \right\rangle$ means a nth-order contribution due to the different interaction with each laser pulse.

In the following, we describe about how we calculate spectral signals from auxiliary wavefunctions. $\left\langle \phi_{101^\dagger}^{(2)}(t) \right|$ can be obtained by propagating two auxiliary wavefunctions.

$$i\hbar \frac{\partial}{\partial t} |\psi_{1^\dagger 01}(t)\rangle = [H_0^\dagger - V_1^\dagger(t) - V_3(t)] |\psi_{1^\dagger 01}(t)\rangle \tag{3.14}$$

$$i\hbar \frac{\partial}{\partial t} |\psi_{1^\dagger 00}(t)\rangle = [H_0^\dagger - V_1^\dagger(t)] |\psi_{1^\dagger 00}(t)\rangle \tag{3.15}$$

These two auxiliary wavefunction are consist of following perturbative expansion terms.

$$\begin{aligned} |\psi_{1^\dagger 01}(t)\rangle &= \sum_{i,j=0}^{\infty} |\psi_{i^\dagger 0j}(t)\rangle \\ &= |\psi_{1^\dagger 00}(t)\rangle + |\psi_{001}(t)\rangle + |\psi_{2^\dagger 00}(t)\rangle + |\psi_{002}(t)\rangle + |\psi_{1^\dagger 01}(t)\rangle + O(i+j \geq 3) \end{aligned} \tag{3.16}$$

$$\begin{aligned} |\psi_{1^\dagger 00}(t)\rangle &= \sum_{i=0}^{\infty} |\psi_{i^\dagger 00}(t)\rangle \\ &= |\psi_{1^\dagger 00}(t)\rangle + |\psi_{2^\dagger 00}(t)\rangle + O(i \geq 3) \end{aligned} \tag{3.17}$$

Due to the rotating wave approximation, -**k** wouldn't interact with $|g\rangle$. Therefore, $|\psi_{001}(t)\rangle$ and $|\psi_{002}(t)\rangle$ don't contribute significant values that can be discarded. By definition,

doi:10.6342/NTU202404353

$\langle\psi_{abs}(t)| = |\psi_{a^\dagger b^\dagger c^\dagger}(t)\rangle^\dagger$, and we can recast that as below.

$$\begin{aligned}
\left\langle \phi^{(2)}_{101^\dagger}(t) \right| &= \langle\psi_{101^\dagger}(t)| - \langle\psi_{100}(t)| \\
\langle\psi_{101^\dagger}(t)| &= |\psi_{1^\dagger 01}(t)\rangle^\dagger \\
\langle\psi_{100}(t)| &= |\psi_{1^\dagger 00}(t)\rangle^\dagger
\end{aligned} \tag{3.18}$$

Therefore, we can calculate $\left\langle \phi^{(2)}_{101^\dagger}(t) \right|$ by subtract the auxiliary wavefunctions of $\langle\psi_{101^\dagger}(t)|$ and $\langle\psi_{100}(t)|$. Apart from these two auxiliary wavefunctions, for all terms in the third-order polarization, we need to propagate other eight auxiliary wavefunctions.

$$i\hbar\frac{\partial}{\partial t}|\psi_{11^\dagger 1^\dagger}(t)\rangle = \left[H_s + F(t) - V_1(t) - V_2^\dagger(t) - V_3^\dagger(t)\right]|\psi_{11^\dagger 1^\dagger}(t)\rangle \tag{3.19}$$

$$i\hbar\frac{\partial}{\partial t}|\psi_{11^\dagger 0}(t)\rangle = \left[H_s + F(t) - V_1(t) - V_2^\dagger(t)\right]|\psi_{11^\dagger 0}(t)\rangle \tag{3.20}$$

$$i\hbar\frac{\partial}{\partial t}|\psi_{1^\dagger 10}(t)\rangle = \left[H_s^\dagger + F^\dagger(t) - V_1^\dagger(t) - V_2(t)\right]|\psi_{1^\dagger 10}(t)\rangle \tag{3.21}$$

$$i\hbar\frac{\partial}{\partial t}|psi_{101^\dagger}(t)\rangle = \left[H_s + F(t) - V_1(t) - V_3^\dagger(t)\right]|\psi_{101^\dagger}(t)\rangle \tag{3.22}$$

$$i\hbar\frac{\partial}{\partial t}|\psi_{01^\dagger 1^\dagger}(t)\rangle = \left[H_s + F(t) - V_1^\dagger(t) - V_2^\dagger(t) - V_3^\dagger(t)\right]|\psi_{01^\dagger 1^\dagger}(t)\rangle \tag{3.23}$$

$$i\hbar\frac{\partial}{\partial t}|\psi_{01^\dagger 0}(t)\rangle = \left[H_s + F(t) - V_2^\dagger(t)\right]|\psi_{01^\dagger 0}(t)\rangle \tag{3.24}$$

$$i\hbar\frac{\partial}{\partial t}|\psi_{001^\dagger}(t)\rangle = \left[H_s + F(t) - V_3^\dagger(t)\right]|\psi_{001^\dagger}(t)\rangle \tag{3.25}$$

$$i\hbar\frac{\partial}{\partial t}|\psi_{000}(t)\rangle = \left[H_s + F(t)\right]|\psi_{000}(t)\rangle \tag{3.26}$$

For $\left|\phi^{(1)}_{01^\dagger 0}(t)\right\rangle$, it can be obtained from the auxiliary wavefuntion in Eq.3.24 and Eq.3.26.

$$\left|\phi^{(1)}_{01^\dagger 0}(t)\right\rangle = |\psi_{01^\dagger 0}(t)\rangle - |\psi_{000}(t)\rangle \tag{3.27}$$

doi:10.6342/NTU202404353

For $\left\langle \phi^{(2)}_{11^\dagger 0}(t) \right|$, it can be obtained from the auxiliary wavefuntion in Eq.3.21 and Eq.3.15.

$$\left\langle \phi^{(2)}_{11^\dagger 0}(t) \right| = \langle \psi_{11^\dagger 0}(t)| - \langle \psi_{100}(t)| \tag{3.28}$$

For $\left| \phi^{(1)}_{001^\dagger}(t) \right\rangle$, it can be obtained from the auxiliary wavefuntion in Eq.3.25 and Eq.3.26.

$$\left| \phi^{(1)}_{001^\dagger}(t) \right\rangle = |\psi_{001^\dagger}(t)\rangle - |\psi_{000}(t)\rangle \tag{3.29}$$

For $\left\langle \phi^{(0)}_{000}(t) \right|$, it can be obtained from the auxiliary wavefuntion in Eq.3.26.

$$\left\langle \phi^{(0)}_{000}(t) \right| = \langle \psi_{000}(t)| \tag{3.30}$$

For $\left| \phi^{(3)}_{11^\dagger 1^\dagger}(t) \right\rangle$, it can be obtained from the auxiliary wavefuntion in Eq.3.19, Eq.3.20, Eq.3.22, Eq.3.23, Eq.3.24 and Eq.3.25.

$$\left| \phi^{(3)}_{11^\dagger 1^\dagger}(t) \right\rangle = |\psi_{11^\dagger 1^\dagger}(t)\rangle - |\psi_{11^\dagger 0}(t)\rangle - |\psi_{101^\dagger}(t)\rangle - |\psi_{01^\dagger 1^\dagger}(t)\rangle + |\psi_{01^\dagger 0}(t)\rangle + |\psi_{001^\dagger}(t)\rangle \tag{3.31}$$

For $\left\langle \phi^{(1)}_{100}(t) \right|$, it can be obtained from Eq.3.15, Eq.3.20, Eq.3.15,

$$\left\langle \phi^{(1)}_{100}(t) \right| = \langle \psi_{100}(t)| - \langle \psi_{000}(t)| \tag{3.32}$$

For $\left| \phi^{(2)}_{01^\dagger 1^\dagger}(t) \right\rangle$, it can be obtained from the auxiliary wavefuntion in Eq.3.23, Eq.3.24, Eq.3.25 and Eq.3.26.

$$\left| \phi^{(2)}_{01^\dagger 1^\dagger}(t) \right\rangle = |\psi_{01^\dagger 1^\dagger}(t)\rangle - |\psi_{01^\dagger 0}(t)\rangle - |\psi_{001^\dagger}(t)\rangle + |\psi_{000}(t)\rangle \tag{3.33}$$

With $P^{(3)}_{PE}(t)$, at a given population time, the absorptive 2D infrared spectrum could

doi:10.6342/NTU202404353

be obtained by taking Fourier-transformation with respect to τ and t

$$
\begin{aligned}
S(\omega_\tau, T, \omega_t) &\sim \int_{-\infty}^{\infty} d\tau \int_{-\infty}^{\infty} dt e^{-i\omega_\tau \tau} e^{i\omega_t t} \times iP^{(3)}(\tau, T, t) \\
S_R(\omega_\tau, T, \omega_t) &\sim \int_{0}^{\infty} d\tau \int_{0}^{\infty} dt e^{-i\omega_\tau \tau} e^{i\omega_t t} \times iP^{(3)}(\tau, T, t) \\
S_{NR}(\omega_\tau, T, \omega_t) &\sim \int_{-\infty}^{0} d\tau \int_{0}^{\infty} dt e^{-i\omega_\tau \tau} e^{i\omega_t t} \times iP^{(3)}(\tau, T, t)
\end{aligned}
\tag{3.34}
$$

where ω_τ is the coherence frequency and ω_t is the detection frequency. The subscripts R and NR respectively means rephasing and non-rephasing spectra. The rephasing spectrum has $\tau \geq 0$ pulse ordering, which is also known as the photon echo signal. In contrast, the non-rephasing spectrum has $\tau \leq 0$ pulse ordering.

doi:10.6342/NTU202404353

Chapter 4 Ar-tagged and N_2-tagged Hydronium Clusters

4.1 Systems

The hydronium clusters are composed of an H_3O^+ cation and three atoms/molecules attaching to the H-atoms. The cluster corresponds to a hydronium ion with its first solvation shell. According to the energy levels of bending overtones and stretching fundamental, we choose Ar-tagged and N_2-tagged hydronium to study. In Ar-tagged hydronium, we expect the signiture of the Fermi resonance is obvious. On the contrary, the N_2-tagged hydronium do not present the spectral features. Therefore, we choose the two clusters to study.

4.2 Vibrational energy and linear IR Spectrum

Before presenting our investigation of the 2D IR spectroscopy of Ar- and N_2-tagged hydroniums, we should confirm the validity of our effective Hamiltonian and the QLE approach. To this end, we calculated the energy levels of the bending and stretching vibrational states and stimulated linear IR spectra using the QLE approach. Comparing

doi:10.6342/NTU202404353

the experimental data allows us to validate the theoretical method and choose the proper friction coefficient that can reproduce the linewidth of peaks.

4.2.1 Energy levels

To clearly describe the model system we studied in this work, the energy levels presented here provide detailed information on our effective Hamiltonian, with a focus on the relevant states required to describe the vibrational dynamics and spectra in the O-H stretching region. Because the incorporation of stretching and bending modes is enough to depict the Fermi resonance occurring in the stretching fundamental spectral region of solvated hydronium, [25] we apply the two kinds of mode in our effective model containing five degrees of freedom. The vibrational energy levels of N_2- and Ar-tagged hydronium in our reduced effective model are presented in Fig. 4.1(b) and (c), respectively. In the figures, the left with orange marks denotes the stretching manifold, and the right with green and blue marks shows the bending and combination bands manifold, respectively. Furthermore, Purple marks in the middle represent the eigenstates that could be observed in the spectrum. The notation of $|b_x, S_y\rangle$ indicates the states containing x and y quanta in the bending and stretching manifolds. For Ar-tagged hydronium, the energy of $|b_0, S_1\rangle$ quite falls close to $|b_2, S_0\rangle$, both of which contain three states with A_1+E symmetry, with a strong anharmonic coupling between them, which results in splitting states($|D_1\rangle$ and $|D_2\rangle$) in the eigenbasis known as the Fermi resonance. The energy splitting in a Fermi resonance doublet with a perfect resonance equals the double anharmonic coupling strength, which helps to know the coupling strengths encoded in our effective Hamiltonian of 30$\sim$40 cm^{-1} between $|b_0, S_1\rangle$ and $|b_2, S_0\rangle$ in Ar-tagged hydronium. In the stretching overtone region, $|b_0, S_2\rangle$ having six states are separated into the upper part (U) and the lower part (L) with

doi:10.6342/NTU202404353

an energy difference of ∼100 cm^{-1}. $|b_0, S_2\rangle_L$ remains relatively unmixed in the eigenbasis. On the contrary, $|b_0, S_2\rangle_U$ mixes with $|b_2, S_1\rangle$ and $|b_4, S_0\rangle$ due to the close energy and the coupling between $|b_0, S_2\rangle_U$ and $|b_2, S_1\rangle$, and between $|b_2, S_1\rangle$ and $|b_4, S_0\rangle$, Both couplings in the stretching fundamental and overtone regions are all induced by cubic anharmonic coupling terms, characterized by Fermi resonance, in the potential energy surface. Therefore, it allows us to expect that the complicated distribution of transitions relating to this region could be observed in 2D IR spectra to reveal the complicated coupling information, which is difficult to obtain in linear IR spectra. For N_2-tagged hydronium, the energy of $|b_0, S_1\rangle$ and $|b_2, S_0\rangle$ are separated with $\sim$ 235 cm^{-1} compared to $\sim$ 15 cm^{-1} in Ar-tagged hydronium and form the unmixed eigenstates. In the two-photon manifold, $|b_0, S_2\rangle$, $|b_2, S_1\rangle$ and $|b_4, S_0\rangle$ remain unmixed similarly. In summary, the difference of energy levels between Ar- and N_2-tagged hydronium is shown in Fig. 4.1(b) and (c) which is encoded in our effective Hamiltonian, and the validity of this could be examined by simulated linear IR spectra shown in the following.

doi:10.6342/NTU202404353

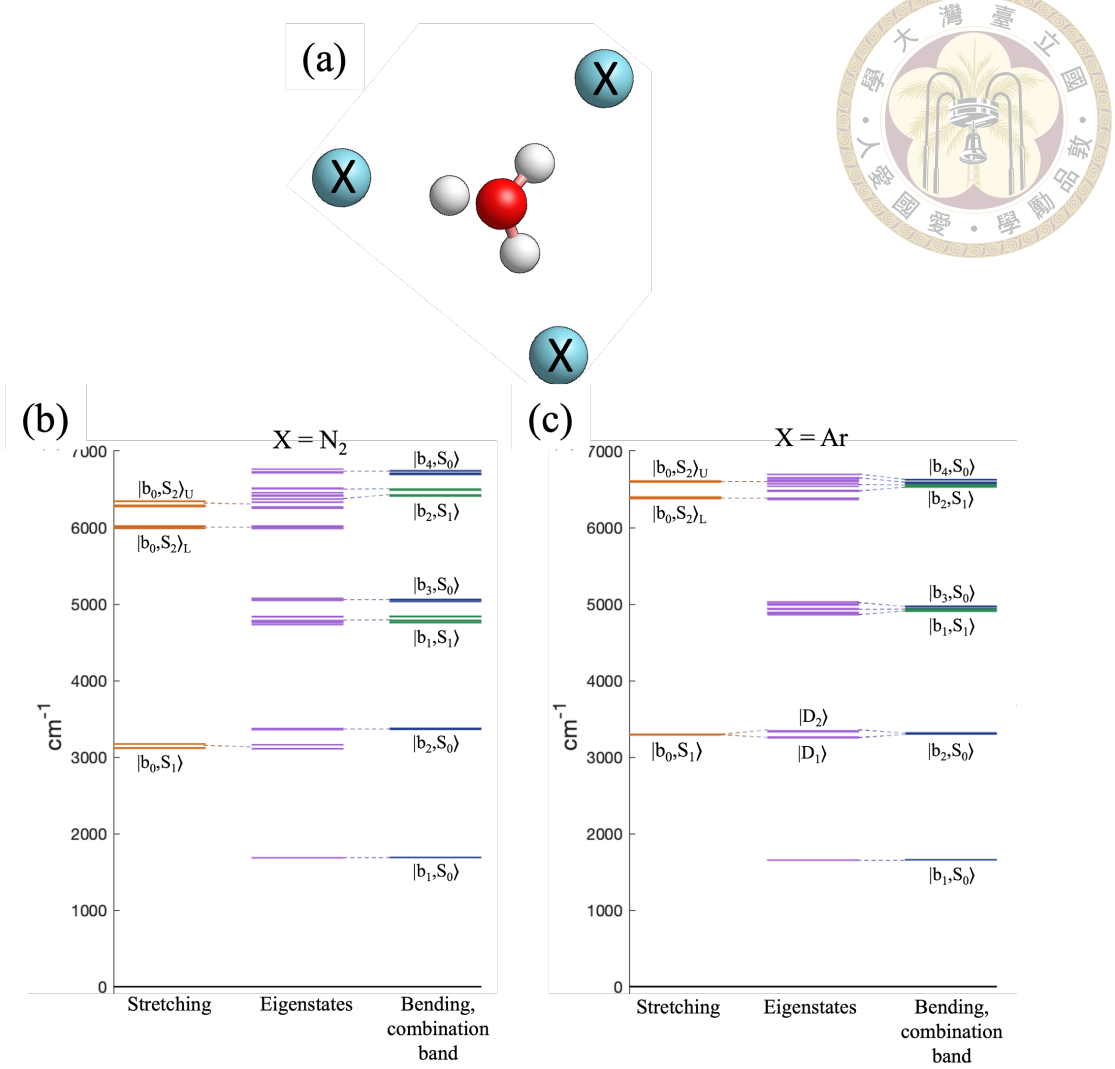

Figure 4.1: (a) The illustration of fully solvated hydronium in X (X = Ar, N_2). (b) Vibrational energy levels of N_2-tagged hydronium. (c) Vibrational energy levels of Ar-tagged hydronium. The states in stretching, bending and combination band manifold are indicated with orange, blue and green marks, respectively. In the middle of the figure, the eigenstates are shown with purple marks. The quanta in the bending and stretching manifolds contained in states are represented by the notation of $|b_x, S_y\rangle$, where x, y are the quanta number.

4.2.2 Linear IR spectra

In our theoretical model, the magnitude of the friction coefficient affects not only the relaxation rate of vibrational excited wave packets but also the linewidths in the spectra. To find the proper friction coefficient, we simulated the linear IR spectra compared with the

doi:10.6342/NTU202404353

experimental spectra carried out by the Fujii group.[24, 25] The simulated linear IR spectrum is calculated by propagating two auxiliary wavefunctions in Runge-Kutta 4 methods. The random forces are turned off to reduce the computational cost because it does not significantly affect spectra. Therefore, we only simulate spectrum with one trajectory. The simulated spectra in this thesis all calculated in the same way. In Fig.4.2, the simulated and experimental linear IR spectra of Ar- and N_2-tagged hydronium, in which the peaks are scaled with the same intensity and shifted to the roughly same position, are shown in orange and blue colors, respectively. With the friction coefficient set to $3.5 \times 10^{-3} fs^{-1}$, the full widths at half maximum (FWHM) of the peaks, located at 3224 and 3308 cm^{-1} in Fig.4.2 (a) and 3110 cm^{-1} in Fig.4.2 (b), are around $15\ cm^{-1}$. We could observe that the major peaks in the experimental data are captured in our simulated spectra, which indicates the validity of the effective Hamiltonian. To this end, we choose a proper magnitude of the friction coefficient to simulate the kinetics of vibrational relaxation in this experimental condition and use this value in the following spectroscopic simulation.

doi:10.6342/NTU202404353

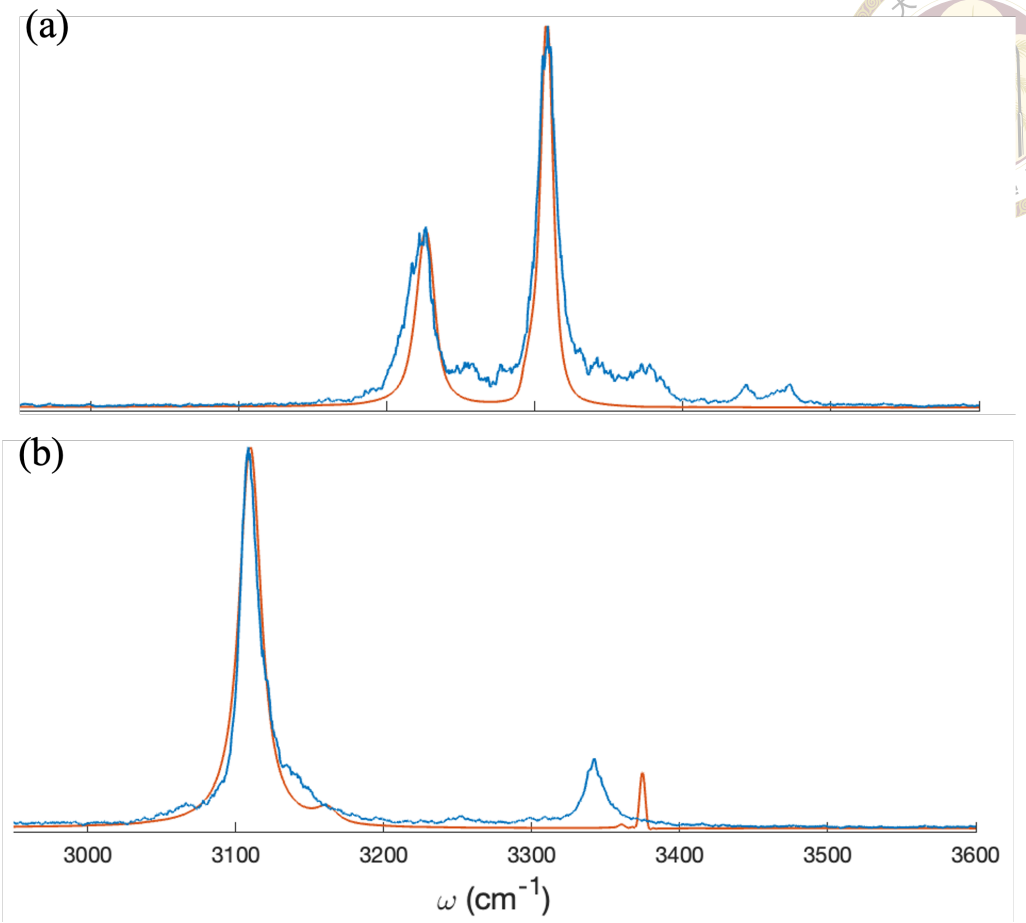

Figure 4.2: The theoretical linear IR spectra (orange line) and the experimental spectra (blue line) of (a) Ar-tagged and (b) N_2-tagged hydronium.[24, 25]The central frequency of laser pulses are set as 3250 cm^{-1} and 3110 cm^{-1} in (a) and (b), respectively. For Ar-tagged hydronium, the intensity of the peak of 3260 cm^{-1} is scaled 0.45 times, and the peak positions are red-shifted with 33 cm^{-1}.

4.3 2DIR spectra of N_2-tagged hydronium

We start from a simpler case of N_2-tagged hydronium to clearly present the result obtained from our theoretical model that we incoperate the dissiaptive dynamics in. As shown in Fig. 4.3, theoretical 2D IR spectra of N_2-tagged hydronium in the stretching region exhibit the diagonal D peak located at $(3107, 3107)\ cm^{-1}$ mainly corresponding to the transition in $|b_0, S_1\rangle$ with E symmetry, and the negative E1 and E2 peaks located at $(3103, 2895)\ cm^{-1}$ and $(3107, 3147)\ cm^{-1}$ relating to $|b_0, S_2\rangle$. Owing to the energy gap

doi:10.6342/NTU202404353

of $\sim 235\ cm^{-1}$ between $|b_0, S_1\rangle$ and $|b_2, S_0\rangle$, the peak related to $|b_2, S_0\rangle$ is more weak than the peaks related to the stretching modes, which seems like spectra only contain one mode. Moreover, although the peaks related to $|b_2, S_0\rangle$ is visible at $3380\ cm^{-1}$ in linear spectrum shown in Fig.4.2, it caused from the intensity in linear spectrum is proportional to the square of magnitude of transition dipole moments. However, due to the third-order light-matter interaction in 2DIR spectroscopy, the intensity in 2DIR spectrum is proportional to the magnitude of transition dipole moments to the power of four, resulting in the weaker intensity of peaks related to $|b_2, S_0\rangle$ on 2DIR spectra. This result demonstrates the validity that our simulation shows an expected result, which can be applied in more complicated system such as Ar-tagged hydronium in the following.

To comprehend the time evolution of spectra more closely, we take a vertical cut at a certain coherent frequency as a function of popualtion time T. Fig. 4.4 exhibits intensity decreasing in peaks reflecting the vibrational relaxation, which we approach with the quantum Langevin equation. The small fluctuation of intensity would be explained in the following section. In Fig. 4.4, we plot the amplitude evolution of the D, E1 and E2 peaks, clearly showing the vibrational relaxation from fundamental stretching modes with a lifetime of ~ 420 fs. In this end, the 2DIR spectra of N_2-tagged hydronium is shown to validate our theoretical method for simulating 2DIR spectroscopy.

doi:10.6342/NTU202404353

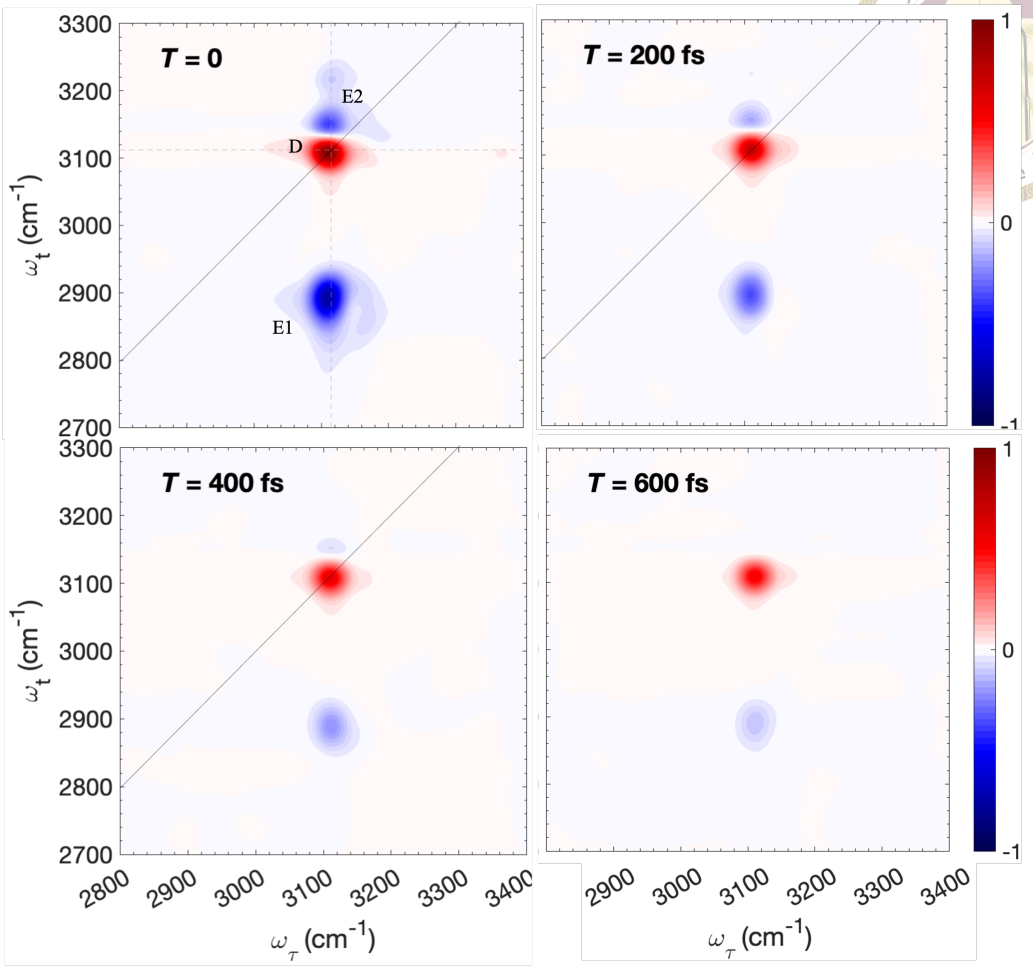

Figure 4.3: Theoretical absorptive 2DIR spectra of N_2-tagged hydronium in the stretching region at population times $T = 0, 200, 400$ and 1200 fs.

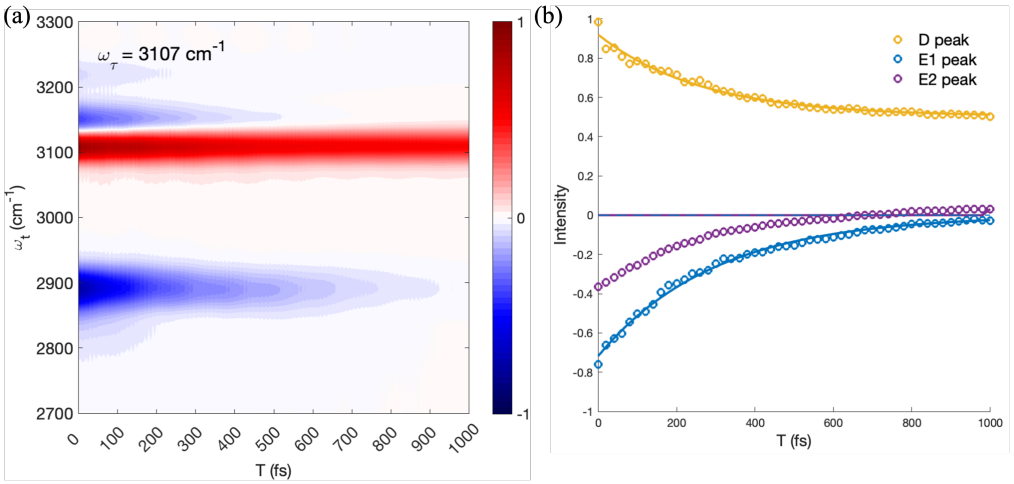

Figure 4.4: Amplitude of E1 peak in theoretical absorptive 2DIR spectra of N_2-tagged hydronium as a function of population time.

doi:10.6342/NTU202404353

4.4 2DIR spectra of Ar-tagged hydronium

4.4.1 Stretching region

To study the features of the Fermi resonance in 2DIR spectra, we simulated 2DIR spectra under the condition that central frequencies and FWHM of laser pulses are set to 3000 cm^{-1} and 5 fs respectively. The amplitudes in spectra are only presented with the real value in this work. Fig. 4.5 shows the theoretical 2DIR spectra in the stretching region of Ar-tagged hydronium at different population times, which are normalized to a peak of the largest amplitude at $T = 0$. Typically, the peaks along the diagonal exhibiting a positive signal reflect the involvement of ground state bleach (GSB) and stimulated emission (SE) in the Liouville pathways and the excited-state absorption (ESA) pathway as a negative signal which usually occurs at a lower detection frequency owing to the anharmonicity. The positive peaks observed in off-diagonal, named cross peaks, nearby the diagonal peaks forming a square pattern are contributed from GSB and SE pathways associated with different modes, which is able to reveal the latent coupling between vibrational modes. These spectra exhibit several complicated features. Although the positive peaks are interfered by negative peaks at $T = 0, 200$ and 400 fs, the diagonal and cross peaks are visible in the spectrum at $T = 600$ fs. The diagonal D1 and D2 peaks are located at $(3258, 3258)\ cm^{-1}$ and $(3335, 3335)\ cm^{-1}$ mainly contributed by the transition between the ground state and the Fermi resonance doublet states mixing with $|b_0, S_1\rangle$ and $|b_2, S_0\rangle$, both with E symmetry, also emerging in the linear IR spectrum. Second, the O1 and O2 cross peaks, located at $(3258, 3335)\ cm^{-1}$ and $(3339, 3253)\ cm^{-1}$, reflect the coupling between $|b_0, S_1\rangle$ and $|b_2, S_0\rangle$. This spectral feature of Fermi resonance has been explored in previous studies.[20, 37–40] Third, the negative E1 to E10 peaks relate to the excited-

doi:10.6342/NTU202404353

state absorption from the doublet states to the higher energy levels, and we will explain those peaks in the following.

2D IR spectra could display information on wealth about vibrational relaxation and coherence dynamics. The spectra in Fig. 4.5 clearly show relaxation and beating in peaks as a function of T. There are amplitude decreases in the time evolution. In particular, the E1 peak shows apparent beating in these amplitudes; the amplitudes are stronger at $T = 0$ and 400 fs and weaker at $T = 200$ fs. The other peaks display similar beating phenomena. The stem of beating in 2D spectra has been analyzed in the previous study that the beatings peaks are mainly contributed from the coherence Liouville pathway in non-rephasing and rephasing spectra, respectively, which could reveal the detailed information in coherence dynamics.[41] Therefore, we will inspect that further to focus on the signature of Fermi resonance in the following.

4.4.2 2DIR signatures of Fermi resonance

4.4.2.1 Square quartet pattern of ESA signals

We first investigate negative signals on the simulated 2DIR spectra of the Ar-tagged hydronium system, depicted in Fig.4.5. The negative signals are attributed to excited state absoprtion from doublet states and decrease in the timescale of $\sim 400\ fs$. In Fig.4.5 (a), ten negative ESA peaks are recognizable, and many square quartet could be identified. Let's focus first on the square quartet including the E1, E2, E7 and E6 peaks.

The square quartet of the E1, E2, E7 and E6 peaks located at the coheremt frequencies of $3261, 3339\ cm^{-1}$ and the detection frequencies of $3030, 3120\ cm^{-1}$, respectively. The coherent frequency and detection frequency provide clues of the formation of peaks.

doi:10.6342/NTU202404353

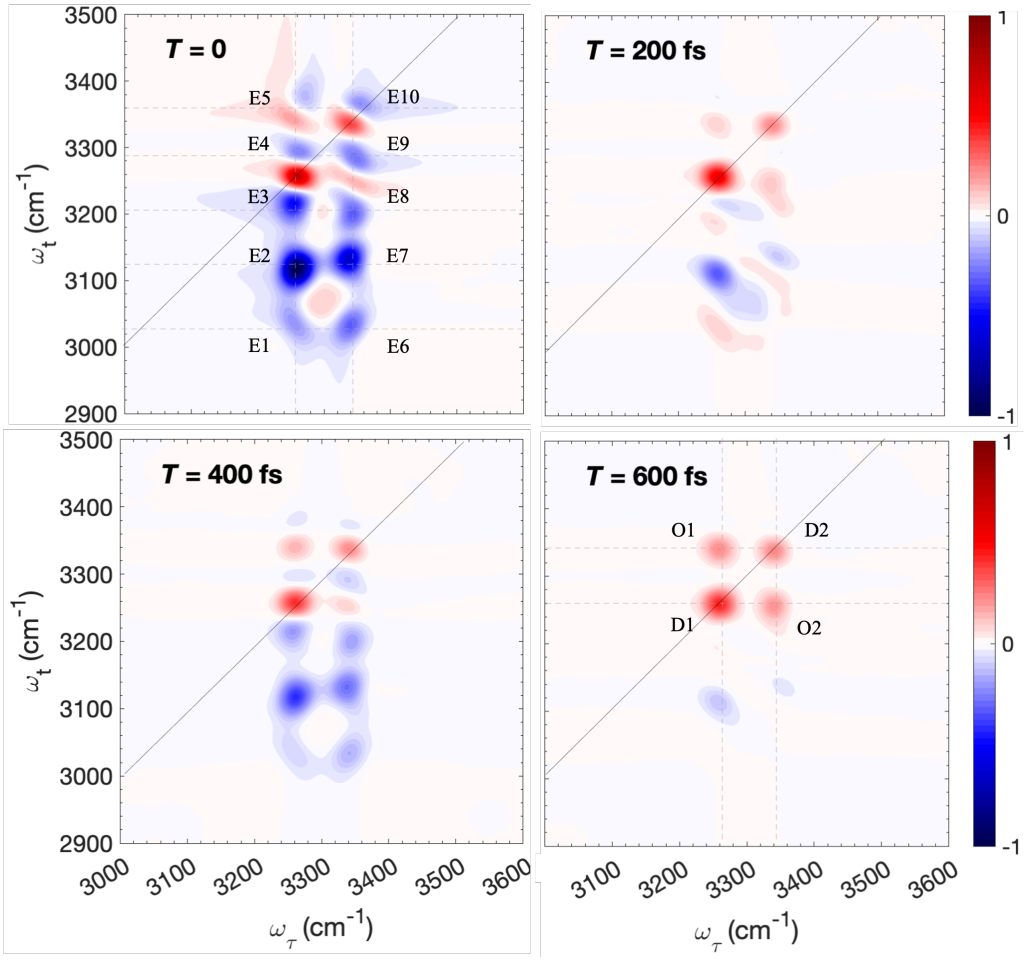

Figure 4.5: Theoretical absorptive 2DIR spectra of Ar-tagged hydronium in the stretching region at population times $T = 0, 200, 400$ and 600 fs.

doi:10.6342/NTU202404353

The coherent frequency, (ω_τ), indicates the allowed transition from the ground state induced from the first laser pulse, which occur at the doublet states associated with Fermi resonance. Therefore, the energy gap lying on the horizontal line of the square quartet corresponds to the energy gap between the doublet states. The detection frequencies, (ω_t), of ESA signals are associated with the emission resulting from transitions from overtones to doublet states. Consequently, ω_t of $3030\ cm^{-1}$ for E1 and E6 peak, and $3120\ cm^{-1}$ for E2 and E7 peak are related to the energy gaps between overtones and doublet states. Additionally, the detection frequenies approximately match the energy differences of 3040 and $3120\ cm^{-1}$ between $|b_0, S_2\rangle_L$ and $|D_2\rangle$, and between $|D_1\rangle$, respectively.

The square quartet, comprising E1, E2, E7 and E6 peak, results from the Fermi resonance that contributes the doublet states observable in linear IR spectra. Figure.4.6 (b) depicts Liouville pathways R_1, R_2, R_3 and R_4 which generate the dominant signal forming the quartet of the E1, E2, E7 and E6 peaks. The depicted arrows represent transition induced by light-matter interaction, where the solid and dotted lines symbolize the interactions with the ket and bra sides of the system density matrix, respectively. The sequence of light-matter interactions progresses from left to right, with the intervals between arrows corresponding to coherence time, population time and detection time, respectively. For instance, in the R_1 pathway, the first laser pulse interacts with the bra side of the system, inducing a transition from $|g\rangle$ to $|D_2\rangle$. The second and third laser pulses excite the ket side of system from $|g\rangle$ through $|D_1\rangle$ to $|b_0, S_2\rangle_L$. Finally, the emission occurs from $|b_0, S_2\rangle_L$ back to $|D_2\rangle$ upon interaction with the final laser pulse Hence, the R_2, in the rephasing pathway resulting in a diagonally elongated lineshape, contributes the formation of the E2 peak.

It's important to note that the transition from $|g\rangle$ to $|D_2\rangle$ correlates with the transi-

doi:10.6342/NTU202404353

tion from $|b_0, S_2\rangle_L$ to $|D_2\rangle$ in the R_2 pathway, manifesting in the E6 peak. However, in the non-rephasing pathway resulting in a elongated anti-diagoonal lineshape, the R_3 pathways exhibits a correlation between the transition from $|g\rangle$ to $|D_1\rangle$ and the transition from $|b_0, S_2\rangle_L$ to $|D_2\rangle$, which provides evidence for the E1 peak. Moreover, with the emission from the transition from $|b_0, S_2\rangle_L$ to $|D_1\rangle$, the E2 and E7 peaks appear align in ω_t of the energy of $|D_1\rangle$ and $|D_2\rangle$, respectively. Therefore, we conclude that the "Fermi resonance quartet" of the ESA peaks, composed of E1, E2, E6 and E7 peaks, is a distinctive spectral signature of Fermi resonance.

Although we do not discuss it in detail, transitions to $|b_2, S_1\rangle$ and $|b_0, S_2\rangle_U$ also contribute to the formation of the quartet comprising E3, E4, E8 and E9 peaks, and E4, E5, E9 and E10 peaks, respectively. In summary, we observe that the quartet of ESA peaks in the 2DIR spectra originates from Fermi resonance in our gas-phase simulation. 2DIR spectroscopy provides the potential to obtain a more complete understanding of the intricate vibrational overtone energy levels arising from the Fermi resonance. It is feasible to conduct 2DIR experiments in the gas phase with a better spectroscopic resolution, thus enabling a completed probing of overtone states.

4.4.2.2 Quantum beatings

The Beatings in 2DIR spectra arise from the evolution of the coherence in the population time period. The time evolution of vertical cuts at $\omega_\tau = 3270\ cm^{-1}$ and $\omega_\tau = 3348\ cm^{-1}$ shown in Fig. 4.7 provides a distinct visualization of the population dynamics and coherence dynamics. We observe, in the cut at $\omega_\tau = 3270\ cm^{-1}$, the D1 peak shows larger intensity at $T = 200$ fs and the E2 peak exhibits larger intensity at $T = 0, 400$ fs. Generally, the beating of positive peaks shows a same frequency but an opposite phase compared

doi:10.6342/NTU202404353

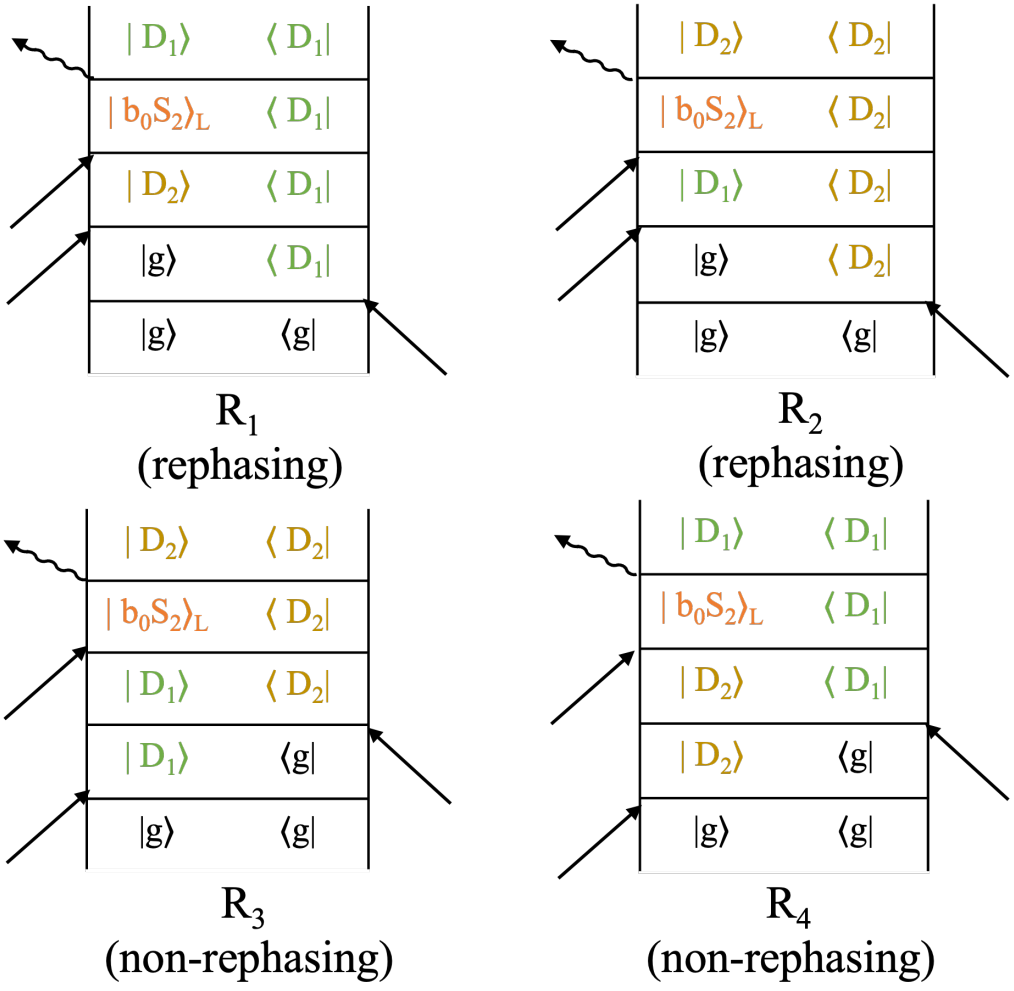

Figure 4.6: The explaination of Liouville pathways contributing to ESA peaks for the spectum of Ar-tagged hydronium. (a) the 2DIR spectrum of Ar-tagged hydronium at $T = 0$, which is the same as Fig.4.5 and (b) the Liouville pathways R_1 to R_4 depicted in energy level diagrams in which the arrows represents pulse absorption/emission, relating to ket and bra side of the system ploted with solid and dotted lines, respectively.

doi:10.6342/NTU202404353

Table 4.1: The table related to constructing the effective Hamiltonian from the simulated spectrum. The left column is the peak positions in simulated spectrum. The middle column is the corresponding eigenenergy from the FBR effective Hamiltonian. The right column is the assignment from the composition of the corresponding eigenenergy.

Peak positions in the Fig.4.13 (a) $(\omega_t, \omega_\tau + \omega_t)$ (cm^{-1})	The eigenenergy from the FBR matrix (cm^{-1})	The assignment
(3269,6372), (3334,6372)	6365, 6378, 6382	$\|b_0, S_2\rangle_L$
(3265,6486), (3342,6478)	6475, 6478, 6478, 6481, 6484	$\|b_2, S_1\rangle$
(3265,6547), (3347,6547)	6540, 6541	$\|b_2, S_1\rangle$
(3269,6624), (3351,6616)	6601, 6607	$\|b_0, S_2\rangle_U$
(3359,6718)	6695, 6696	$\|b_4, S_0\rangle$

with that of negative peaks in Fig.4.7. We analyze the behavior of peaks by executing a Fourier transfer along T in Fig.4.8 to obtain the energy gap within the coherence in the density matrix which results in the beating phenomenon on 2DIR spectra from the time evolution of the coherence. In Fig.4.8, although a few signals stem from the interference of positeive and negative siganls, the significant signals align on around $\omega_T = 80\ cm^{-1}$ that means the energy gaps within the coherence which corresponds to the energy difference between $|D_1\rangle$ and $|D_2\rangle$. To explain the Liouville pathways involving in the quantum beating, we present the pathways mainly contribute the beating signals in positive peaks in Fig.4.9. In the R_7 pathway contributing the signal in D1 peak, the firt pulse excites the ket side of $|D_1\rangle$ then the second pulse create the coherence composed of $|D_1\rangle$ and $\langle D_2|$ in the population period. Therefore, this coherence manifest the beating signals in D1 peak which oscillate in the period ~ 400 fs due to the energy difference between $|D_1\rangle$ and $\langle D_2|$. Moreover, in Fig.4.6, we can find the coherence in the population time period in the R_1 to R_4 pathways which all devote the beating in ESA peaks. Hence, we assign the quantum beating on 2DIR spectra as a feature of Fermi resonance. In contrast, the linear

doi:10.6342/NTU202404353

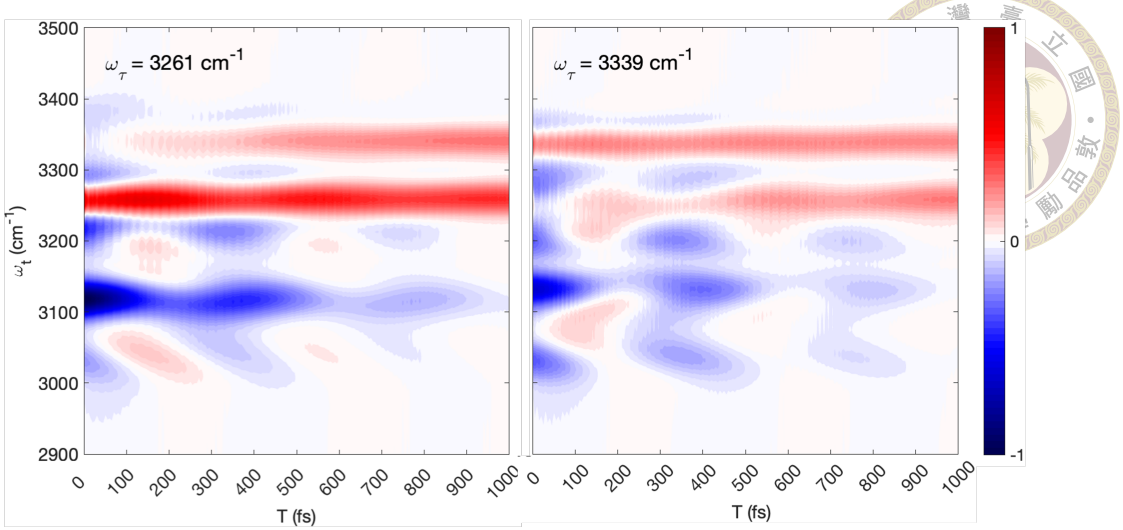

Figure 4.7: Time evolution of the vertical cut at (a)$\omega_\tau = 3270\ cm^{-1}$ (b)$\omega_\tau = 3348\ cm^{-1}$ of the 2DIR spectra of Ar-tagged hydronium in the stretching region.

IR spectrum remains relatively unclear enough about the Fermi resonance, which requires more effort to analyze spectra to obtain detailed information. In 2DIR spectra, apart from the cross peak in the off-diagonal to confirm the existence of Fermi resonance, the beating could be the signature to disentangle the Fermi resonance as observed in similar 2DIR experimental studies.[40]

4.4.3 Stretching-Bending Cross Region

In the cross region, detailed information on population transfer dynamics could be clearly obtained.[42] Figure. 4.10 presents the theoretical 2DIR spectra in the stretching-bending cross region of Ar-tagged hydronium at $T = 0, 200, 400, 600$ fs, which exhibits a complex pattern of peaks. Although peaks in this region are relatively weak, after enlarging the amplitudes, we could observe two negative E11 and E12 peaks in this region, $(3261, 1616)\ cm^{-1}$ and $(3347, 1661)\ cm^{-1}$, relating to the ESA of Liouville pathways associating with doublet states, $|b_1, S_1\rangle$ and $|b_3, S_0\rangle$. From the same reason, the cubic term in PES, contributing Fermi resonance, also couple the states of $|b_1, S_1\rangle$ and $|b_3, S_0\rangle$. In

doi:10.6342/NTU202404353

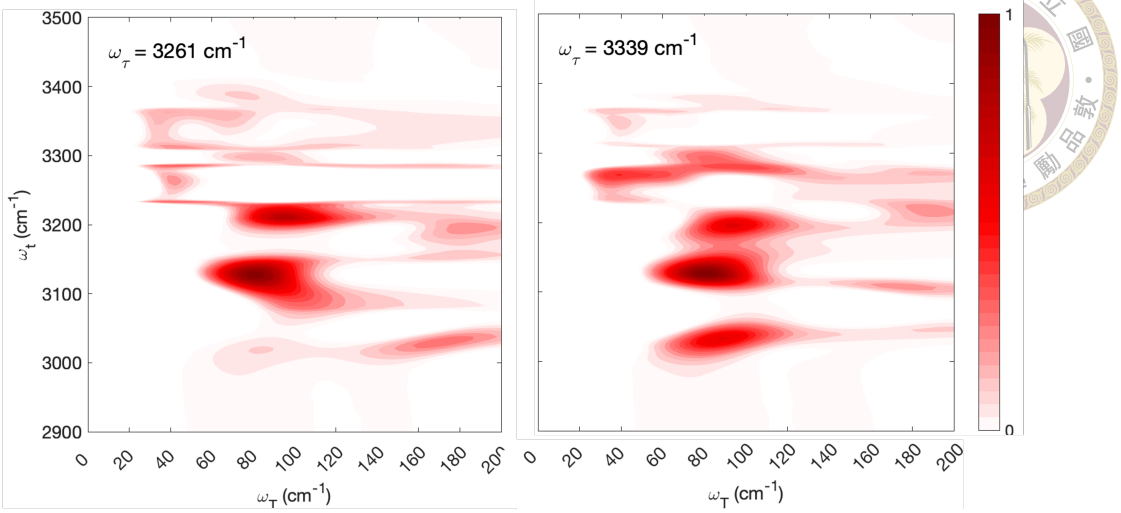

Figure 4.8: The power spectra obtained from the vertical cuts in Fig.4.7 with Fourier transforms along the population time T. The signals is shown in the absolute values.

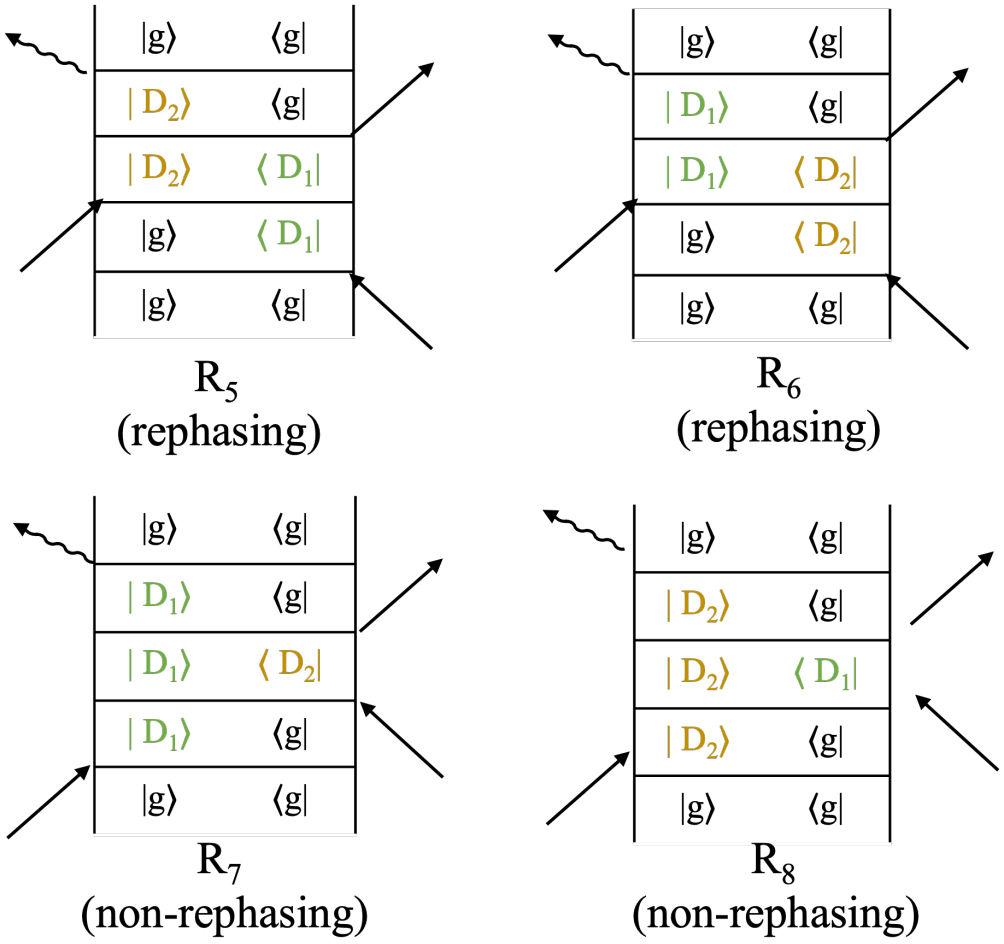

Figure 4.9: The Liouville pathways R_5 to R_8, illustrated in double-sided Feynnman diagrams, contribute to quantum beatings in positive peaks for the spectum of Ar-tagged hydronium.

doi:10.6342/NTU202404353

Fig. 4.11, the vertical cuts exhibit ultrafast quantum beatings in the population time evolution on E11 and E12 peaks. The coherences consist of $|b_1\rangle$ and $\langle D_1|$ presenting the ultrafast beating because of the energy gap of $\sim$ 1650 cm^{-1}, where the pathways are shown in Fig.4.12. However, depsite the vibratinal relaxation features in SE and ESA pathways, there is no signature of population transfer from stretching to bending overtone to bending fundamental. In previous studies about population transfer of O-H stretching and bending in water,[43–45] being similar to our system, they indicated the relaxations of excited stretching state involve the bending modes caused from the Fermi resonance between stretching and bending overtone, which we doesn't observe in our theoretical 2DIR spectra. The reason is that the Markovian limit is applied in our theoretical method resulting in no discrepancy in relaxation rates between states with different energy gaps. Furthermore, in our theoretical model, the relaxation of system is deriven by the displacement of the wavepacket from the equilibrium posiition on PES. The PES of bending modes is much like harmonic potential compared with the stretching modes, which results in the displacement on the PES of bending modes relative small then leading to a slow relaxation within the degrees of freedom of bending modes. In summary, the theoretical method of dissipative dynamics simulation could be further improved, which would be discuss in chapter 7 in detail.

4.5 The effective Hamiltonian extracted from 2DIR spectra

In this section, we present how 2DIR spectroscopy offers the advantage of extracting the effective Hamiltonian, particularly focusing on information about states in the near-

doi:10.6342/NTU202404353

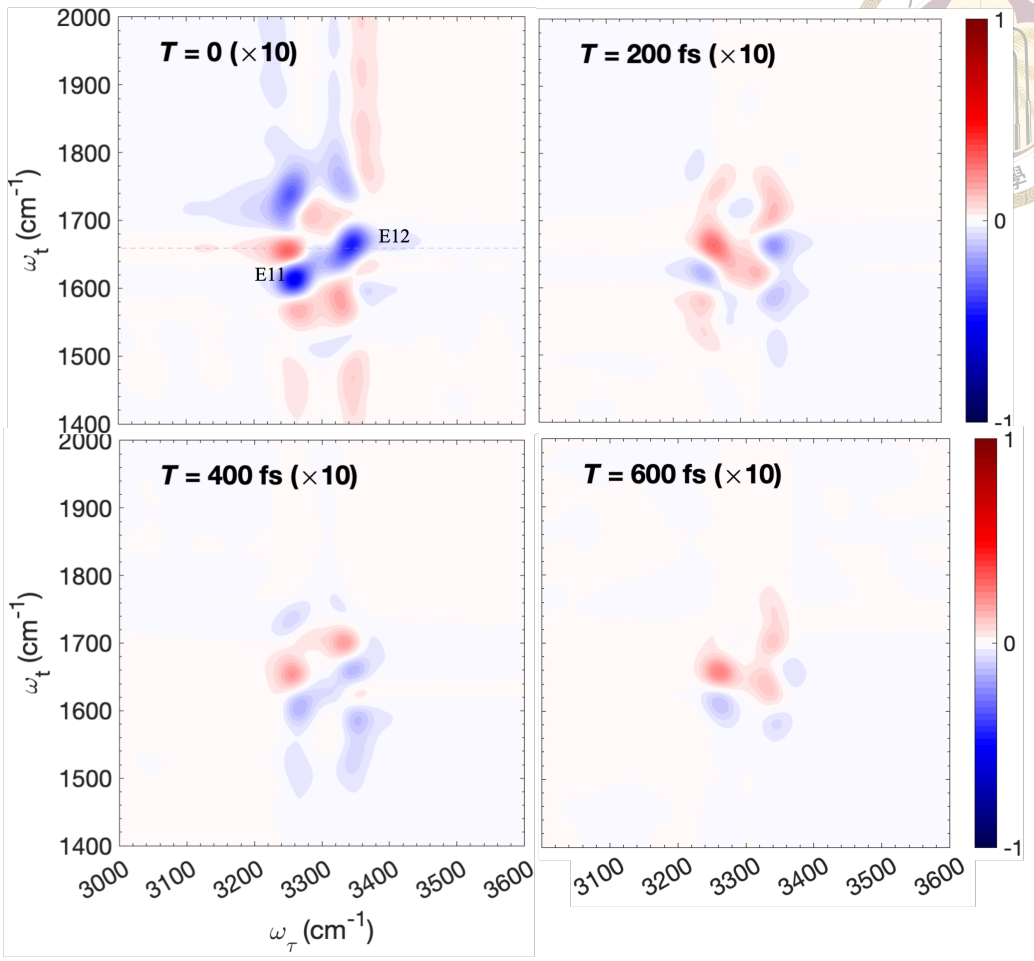

Figure 4.10: Theoretical absorptive 2DIR spectra of Ar-tagged hydronium in the stretching-bending cross region at the population times at $T = 0, 200, 400$ and 600 fs.

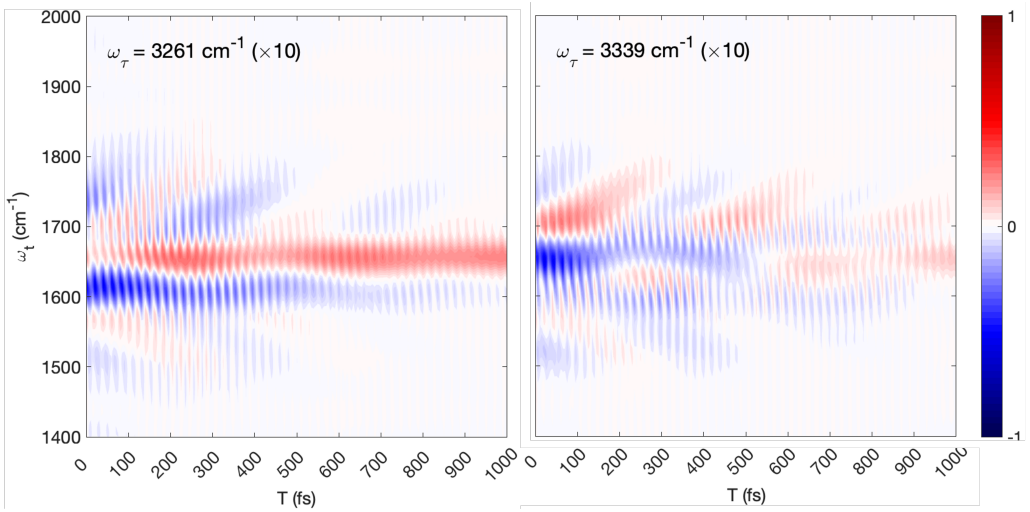

Figure 4.11: Time evolution of the vertical cut at (a)$\omega_\tau = 3257\, cm^{-1}$ (b)$\omega_\tau = 3335\, cm^{-1}$ of the 2D IR spectra of Ar-tagged hydronium in the stretching-bending cross region.

doi:10.6342/NTU202404353

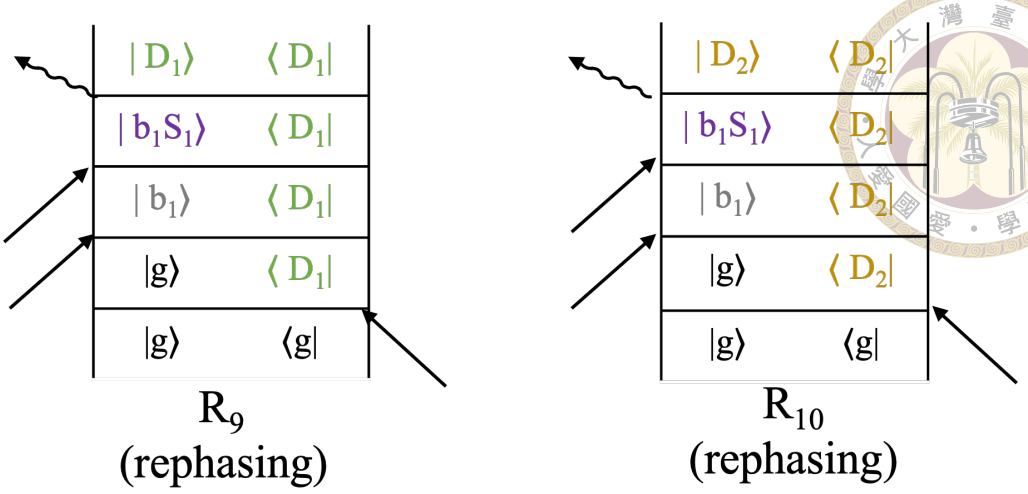

Figure 4.12: The Liouville pathways R_9 and R_{10}, illustrated in double-sided Feynnman diagrams, contribute to quantum beatings in negative E11 and E12 peaks, respectively, for the spectum in the cross region of Ar-tagged hydronium.

infrared energy region hardly probed by linear spectrosocpy. The procedure is illustrated as follows. First, positive peaks along the diagonal in Fig.4.5 are observed, indicating states excited from the ground state with a one-quantum change, related to the peaks seen in linear spectra. Consequently, we identify states at approximately 3258 and 3335 cm^{-1}, which correspond to $|D_1\rangle$ and $|D_2\rangle$ encoded in our effective Hamiltonian. Subsequently, the states transitioning from $|D_1\rangle$ and $|D_2\rangle$ are discerned from the ESA peaks.

The absorptive spectrum contains signals from both rephasing and non-rephasing pathways, and we suggest utilizing only rephasing spectrum to more efficiently reveal state information in the near-IR region. Considering the Liouville pathways shown in Fig.4.6 (b), the two rephasing pathways (R_1 and R_2) each involves the same D-manifold state ($|D_1\rangle$ in R_1 and $|D_2\rangle$ in R_2) in the interaction with the first (excitation) and last (emission) pulses. As a result, the energy of the corresponding Near-IR state ($|b_0, S_2\rangle_L$) equals the sum of the energy of the excitation and emission pulses ($E_{NIR} = \omega_\tau + \omega_t$). However, the two non-rephasing pathways (R_3 and R_4) each involves different D-manifold states in the excitation and emission pulses. Therefore, the relation doesn't hold true in the non-

doi:10.6342/NTU202404353

rephasing signals ($E_{NIR} \neq \omega_\tau + \omega_t$). Hence, we propose that utilizing rephasing spectra offers a efficient way to unveiling the states in the near-IR region.

We introduce the figure with the x-axis denoted by ω_τ and the y-axis by $\omega_\tau + \omega_t$, representing the signals from rephasing pathways, shown in Fig.4.13 (a) in the absolute value, to clearly assign near-IR states. At $\omega_\tau = 3258\ cm^{-1}$, four peaks are observed at $\omega_\tau + \omega_t$ of $6372, 6486, 6547$ and $6624\ cm^{-1}$. These peaks correspond to the near-IR states transitioning from $|D_1\rangle$, which primarily composed of $|b_0, S_2\rangle_L$, $|b_2, S_1\rangle$, $|b_2, S_1\rangle$ and $|b_0, S_2\rangle_U$, respectively. It's worth noting that the slight shift of state energy between from the spectrum and from the effective Hamiltonian are due to the interference of peaks. In addition, at $\omega_\tau = 3335\ cm^{-1}$, five peaks are detected at $\omega_\tau + \omega_t$ of $6372, 6478, 6547, 6616$ and $6718\ cm^{-1}$. These peaks predominantly consist of $|b_0, S_2\rangle_L$, $|b_2, S_1\rangle$, $|b_2, S_1\rangle$, $|b_0, S_2\rangle_U$ and $|b_4, S_0\rangle$, respectively.

In the end, by utilizing the figures with the y-axis denoted by $\omega_\tau + \omega_t$, we distinguish the near-IR states from the diagonalized matrix from the FBR effective Hamiltonian to validate the procedure. We construct a new effective Hamiltonian that includes 22 selected states based on the simulated 2DIR spectrum, whose energy diagram is plotted in Fig.4.13 (b). In Fig.4.14 (b), we present the 2DIR spectrum calculated from this effective Hamiltonian, which exhibits spectral feature nearly identical to those in Fig.4.14 (a). Ultimately, 2DIR spectroscopy is advantageous in extracting the effective Hamiltonian, specially the states in the near-IR region, providing a comprehensive view to chemical systems.

doi:10.6342/NTU202404353

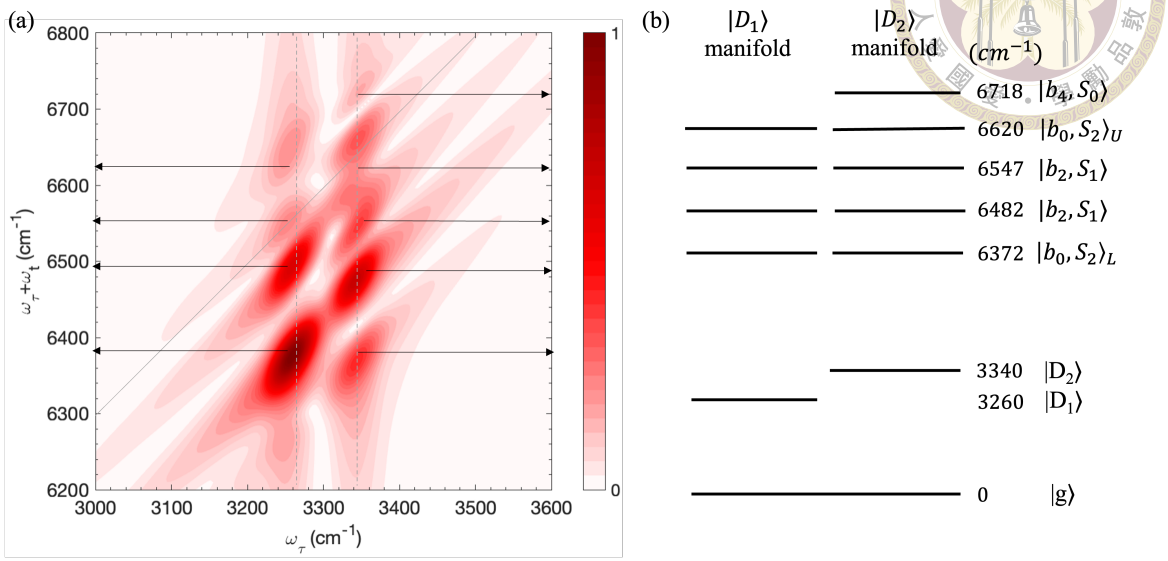

Figure 4.13: Theoretical absorptive 2DIR rephasing spectra in absolute value of Ar-tagged hydronium in the stretching region at $T = 0$. The spectra is extracted from the spectrum in Fig.4.5.

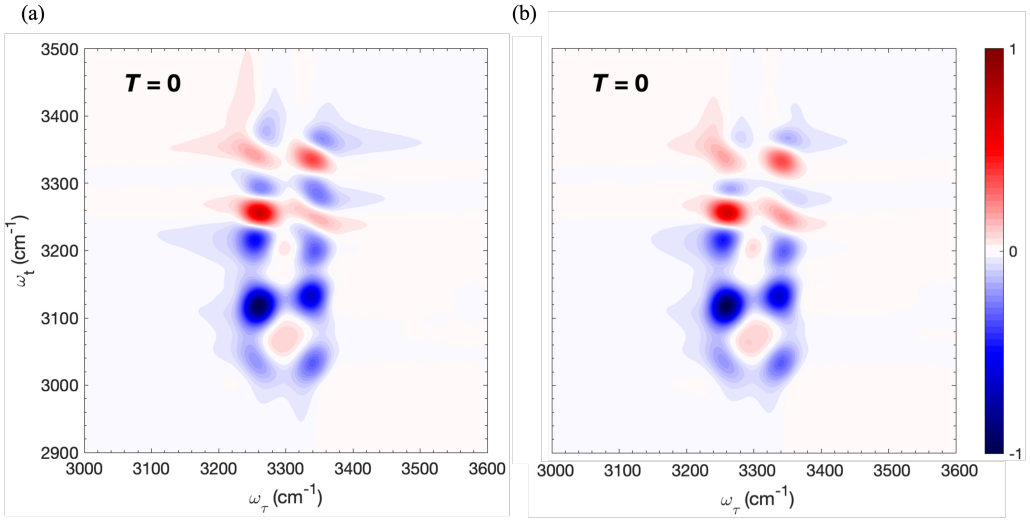

Figure 4.14: (a)the 2DIR spectrum of Ar-tagged hydronium at $T = 0$ (b)the reproduced 2DIR spectrum of Ar-tagged hydronium at $T = 0$ from the effective Hamiltonian based on (a).

doi:10.6342/NTU202404353

Chapter 5 HBr-tagged and HCl-tagged Methylammonium Clusters

5.1 Systems

We describe the solvated methylammonium clusters to provide a comprehensive understanding of the systems. The tagged molecules are hydrogen halide, hydrogen bromide and hydrogen chlorine (HBr and HCl), which exhibits a similar peak positions compared with the FTIR spectra of $MAPbX_3$. We expected the difference between HBr-tagged and HCl-tagged MA can be probed by the 2DIR spectra. The is because the hydrogen bonds between MA and tagged molecules are different in these cases, where the hydrogen bonds are stronger in HBr-tagged than HCl-tagged MA systems. Furthermore, the mixed lead-halide perovskites also are important systems for the study related to the microscopic environment of MA in the perosvskite. Hence, we also discuss the mixed hydrogen halide-tagged MA in the following section. In the following simulation, we include ten vibrational modes in our effective Hamiltonian: four rocking modes, three NH_4^+ bending modes and three N-H stretching modes. With a focus on the Fermi resonance, the ten modes enough capture the spectral pattern. Therefore, we choose those vibrational modes

doi:10.6342/NTU202404353

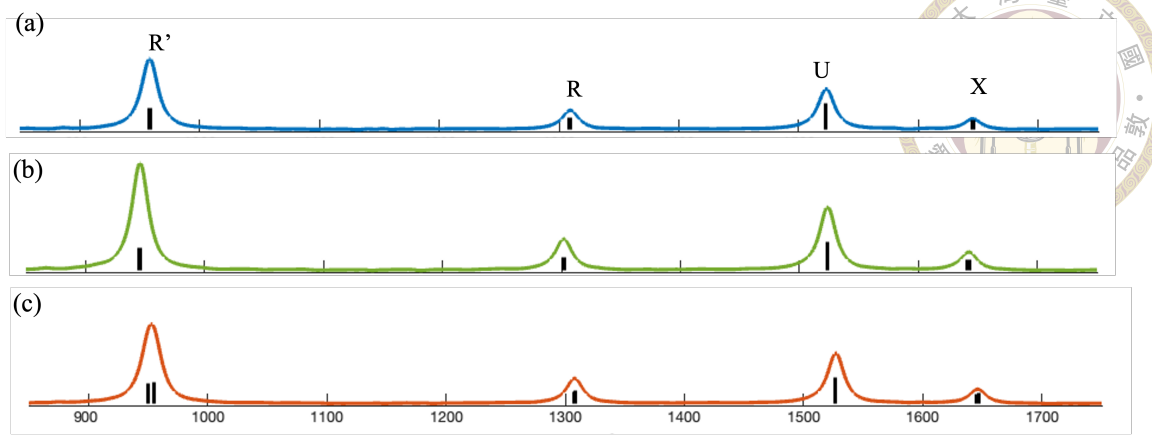

Figure 5.1: The theoretical FTIR spectra in the bending region of (a)$(HBr)_3$-tagged, (b) $(HCl)_3$-tagged and (c)$(HBr)_1(HCl)_2$-tagged.

to simulate linear and 2DIR spectra.

5.2 Linear spectra

We discuss the linear spectra of $(HBr)_3$-tagged, $(HCl)_3$-tagged and $(HBr)_1(HCl)_2$-tagged MA to provide comprehensive pictures of solvated methylammonium systems. The spectra in the bending region are shown in Fig.5.1. The peaks in the region correspond to four rocking modes and bending modes. For the three cases, the peaks are nearly in the same position due to the insensitivity of the hydrogen bond strength in rocking and bending modes. Therefore, we think that the spectra in the bending region are not suitable to probe the microscopic environment of MA in pervoskites.

Fig.5.2 depicts the linear spectra in the stretching region. Between 2500 and 3300 cm^{-1}, the combination tones involving one quanta of rocking and bending modes, as well as the overtones of bending modes, are clearly separated as the lables. According the previous study,[18] due to the anharmonic couplings, these combination tones and overtones are recognizable, with intensity borrowing from the stretching fundamentals. Also, the

doi:10.6342/NTU202404353

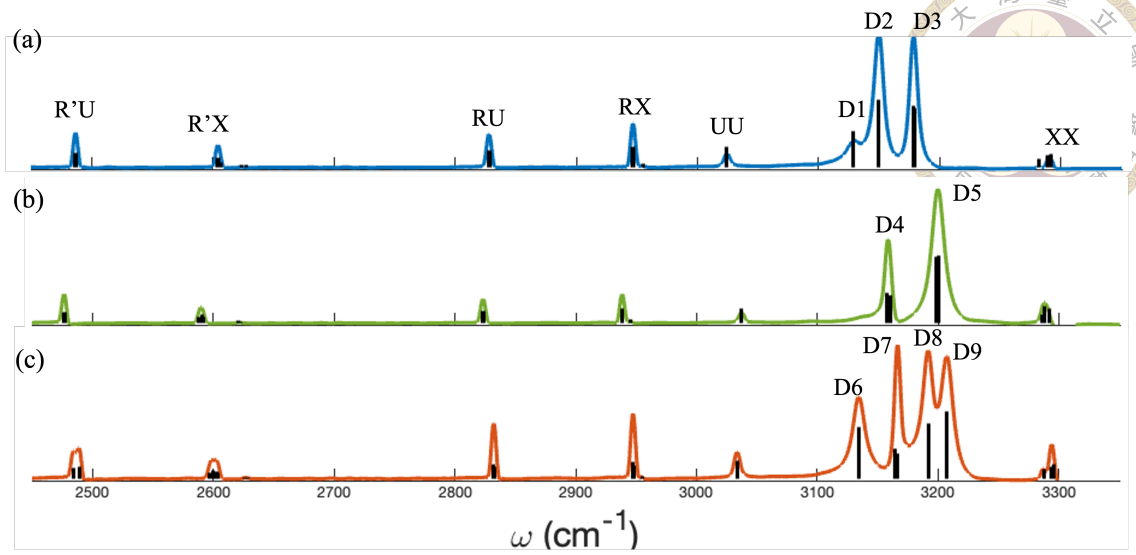

Figure 5.2: The theoretical FTIR spectra in the stretching region of (a)$(HBr)_3$-tagged, (b) $(HCl)_3$-tagged and (c)$(HBr)_1(HCl)_2$-tagged.

main difference located at around 3150 cm^{-1} are contributed from the Fermi resonance between $|S_1\rangle$ and $|UX\rangle$.[18] The nine peaks from D1 to D9 are labeled. Here, with a focus on the assignment of experiments, we assume the results of the Femri resonance from the anharmonic *ab initio* calculation are unknown. The spectral features related to the nine peaks are important in the 2DIR spectra because we already have the spectral signatures of the Fermi resonance obtained from chapter 5. It is important that the nine peaks are stemmed from whether independently uncoupled vibrational modes, coupled vibrational fundamental modes or the Fermi resonance. Therefore, we would focus on the assignment or phyiscal meaning of the nine peaks in the following.

5.3 Comparision between experimental and theoretical spectra

To reinforce the credibility of our theoretical approach, we simulate the 2DIR spectra of hydrogen halide-tagged MA comparing with the experimental 2DIR spectra of pure and

doi:10.6342/NTU202404353

mixed MA lead-halide perovskites.[33] They examined the spectra to study the rotation motion of MA in the pervskite. Hoewver, we state the 2DIR spectra in their study lack the structure which help us to know the microscopic environment of MA in perovskites because they only care about the spectra in bending modes. Fig.5.3 depicts the 2DIR spectra in the NH_3^+ umbrella mode (U) of MA in $T = 300$ fs, where upper part is the experimental spectra and lower part is our theoretical spectra. Here, we simulate theoretical spectra with the Gaussian laser profile with the center frequency of 1500 cm^{-1} and FWHM of 150 fs with a focus on the spectral region of U.

The spectra exhibits signatures of single vibrational modes, where the positive peak is related to fundamental transition and negative peak is related to the transition with the overtone state of U mode. In the experimental spectra, $MAPb(Cl)_3$ shows higher frequency than $MAPb(Br)_3$, and $MAPb(Br:Cl)_3$ lies in the middle of these two, which indicates the homogeneous composition in the mixed lead-halide perovskite. In our simulation, $(HCl)_3$-tagged and $(HBr)_3$-tagged MA are at nearly the same position due to the slightly change of magnitude in the hydrogen bonds. The difference between the two cases is due to the anharmonicity of the bending overtones, which has twice the impact. In mixed tagged MA, the peaks presents slightly higher frequency. Moreover, due to the observation of mixed lead-halide MA perovskite, we tune a larger friction coefficient to mimic the spectra signature of that, which indicates the different dissipative dynamics in MA perovskite is captured by our theoretical method. In summary, our simulation catch overall spectral pattern in U region comparing with the experimental spectra beside slight peaks shiftings and examine the difference of dissipative dynamics in the pure and mixed lead-halide MA perovskite.

doi:10.6342/NTU202404353

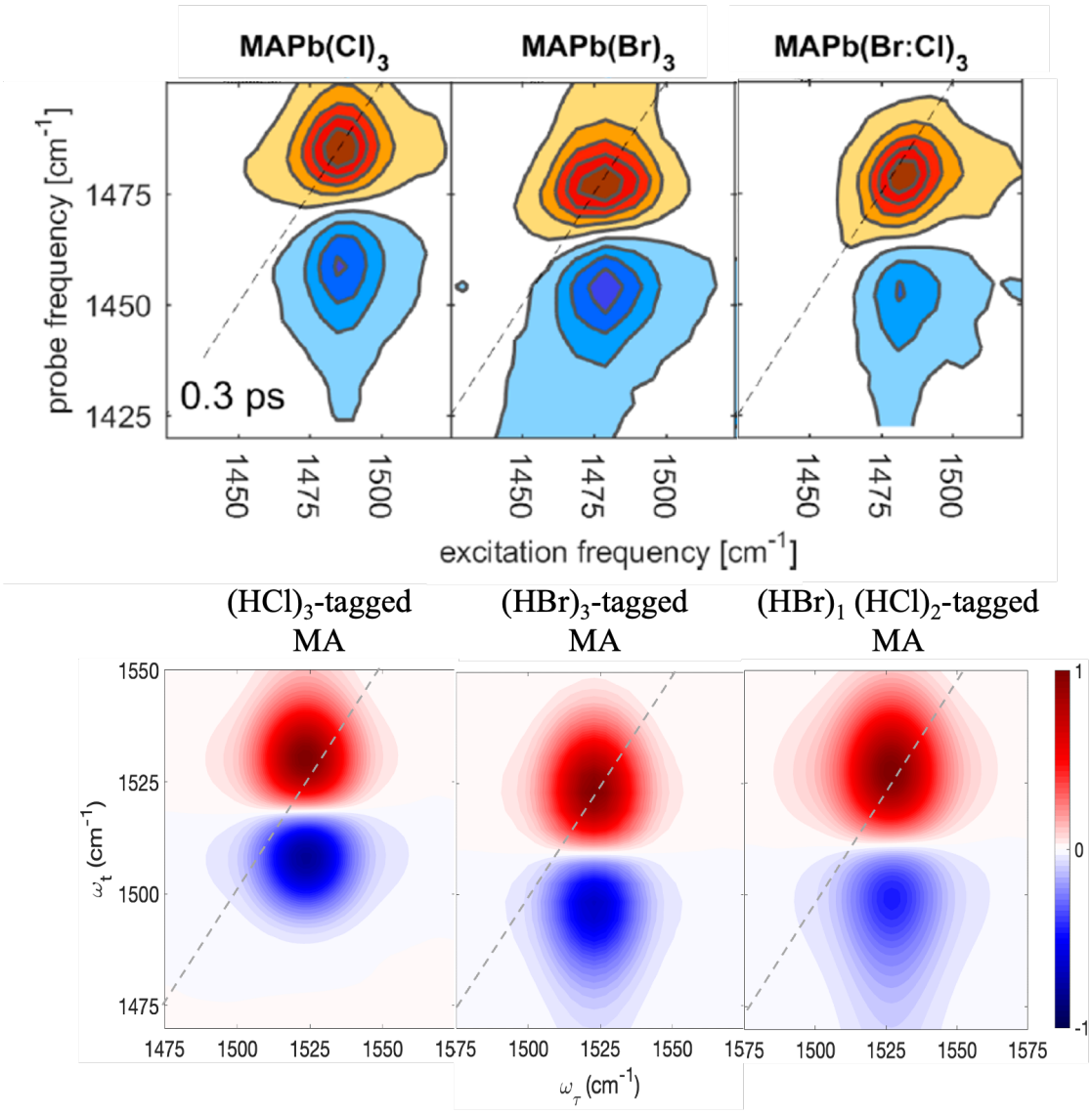

Figure 5.3: (a)Experimental 2DIR spectra of $MAPb(Cl)_3$, $MAPb(Br)_3$ and $MAPb(Cl_0.6Br_0.4)_3$, respectively.[33] (b)Theoretical 2DIR spectra of $(HCl)_3$-tagged, $(HBr)_3$-tagged and $(HBr)_1(HCl)_2$-tagged methylammonium with the friction coefficients of 0.001, 0.0008 and 0.0018 fs^{-1}, respectively.

doi:10.6342/NTU202404353

5.4 2DIR spectra of $(HBr)_3$-tagged MA

In the following section, we will closely examine the spectral signatures of the three hydrogen halide-tagged MA cases. Our focus will be on emphasizing the Fermi resonance signatures and coherence Liouville pathways as probes for the microscopic environment of MA. Fig.5.4 illustrates the theoretical 2DIR spectra of $(HBr)_3$-tagged MA in the bending and stretching region. The Gaussian laser profile with the center frequency of 2250 cm^{-1} and FWHM of 5 fs, where tha frequency region covers the whole mid-IR region.

5.4.1 Bending region

First, we discuss the 2DIR spectrum in the bending region in Fig.5.4 (b). The diagonal peaks exhibits negative signal at the expected position from the FTIR spectrum. However, except for the R' peak, no positive signal is observed. The negative peaks show a non-rephasing spectral lineshape, characterized by an anti-diagonal orientation. We also observe the off-diagonal peaks perform negative and non-rephasing features. To understand the reason causing those unfamiliar features, we conduct a diagonal cut in the following, which depicts the diagonal signals along population time period.

The diagonal cut provide a clear view into time evolution of the coherence evolving in the population time period. Fig.5.5 (a) illustrates the diagonal cut. The diagonal cut shows ultrafast beatings in all diagonal peaks in the bending region. We conduct the Fourier transform along population time from the diagonal cut to clear know the frequency corresponding to ultrafast beating. Hence, we observed a progression from 1600 to 2400 cm^{-1}, which corresponds the energy difference between the strongest peaks, comprising

doi:10.6342/NTU202404353

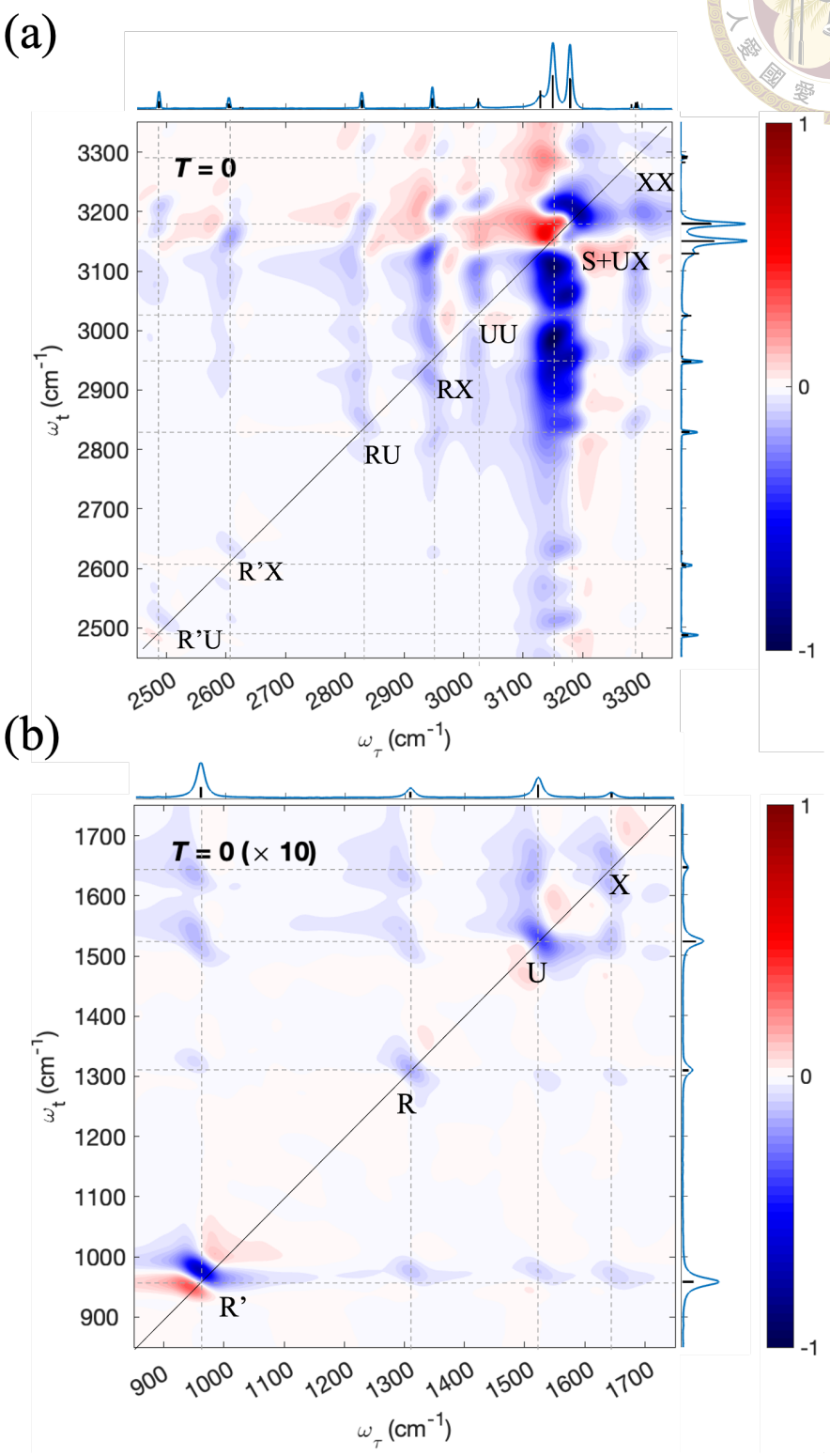

Figure 5.4: The theoretical 2DIR spectra of $(HBr)_3$-tagged MA in (a)the bending region and (b)the stretching region with FWHM of 5 fs in the laser pulses.

doi:10.6342/NTU202404353

$|S_1\rangle$, in the stretching region and states in the bending region. For example, the U peak located at around 1520 cm^{-1} plus 1700 cm^{-1} in Fig.5.5 (b)equals the 3220 cm^{-1} which corresponds to the energy of prominent peaks in the stretching region observed in the FTIR spectrum.

Liouville pathways visualize the light-matter interaction in the 2DIR spectrocopy which can clear assign the origin of peaks in spectra. In the following, we use the U peak to provide further explanation. According the observation, the coherence created by the first and second laser pulse contains $|U\rangle$ and $|S_1\rangle$ in the population time period. Subsequently, the non-rephasing pulse sequence is choosed due to the anti-diagonal lineshape observed in the U peak in Fig.5.4 (b). Therefore, we found the two coherence pathways, R_1 and R_2 ploted in Fig.5.5 (c) contribute the signal in the U peak. Particularly, the signal stemming from R_2 is dominant, which is related to the excited state absorption with combination tone including one quanta U and S.

Here, we discuss the advantages of the phenomenon. The main reason contributing to this phenomenon is the ultrashort laser pulse (5 fs) we use, which covers a broad range of frequencies. Namely, if the ultrashort laser pulse is used, we can easilier observe the states with a small transition dipole moment, where the intensity borrowing occurs. Therefore, the coherence pathways play an important role not only when the Fermi resonance occurs but also when we apply the ultrashort laser pulse. However, despite the advantage, we consider it is difficult to discuss the fine structure in the bending region such cross peaks and excited state absorptions related to overtones.

In Fig.5.6, we plot the spectrum in the bending region with FWHM of 40 fs and center frequency of 1300 cm^{-1} of laser pulses, which only cover the energy in the bending

doi:10.6342/NTU202404353

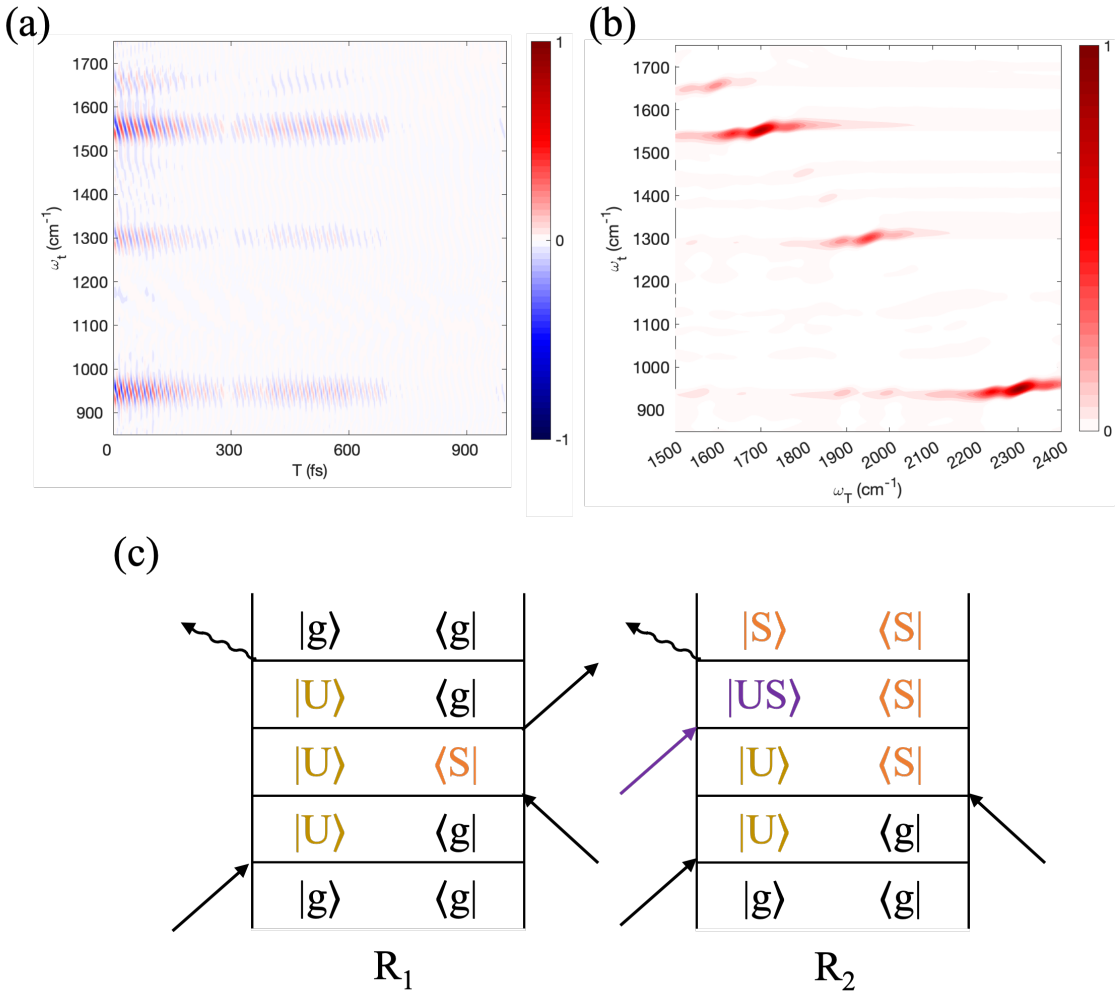

Figure 5.5: (a)The diagonal cut of 2DIR spectra of $(HBr)_3$-tagged MA in the bending region, (b)the power spectrum obtained from (a) and (c)the Liouville pathway explaining the ultrafast beating signals

doi:10.6342/NTU202404353

region. The signal of the spectrum is maximized 500 times compared to the signal of the dominant peak in the stretching region, which echos the previos statement above. The spectrum exhibits familiar spectral features such as peaks with Lorentzian lineshapes. The clear pairs of peaks in diagonal can be observed related to $|R'\rangle$ and $|U\rangle$, $D_{R'}$, $E_{R'}$, D_U and E_U due to larger transition dipoles. Except the peaks lie around diagonal, we observe cross peaks between every rocking and bending peaks, such as $C_{R',U}$ and $C_{R',U}$. In the following, we discuss the detailed meaning manifested from this spectrum.

It is interesting that, $E_{R'}$ peak lies above $D_{R'}$ peak, which indicates the energy of excited state absorption is higher than that of fundamental transition. Moreover, the cross peaks is observable because we includes the anharmonicity in our effective Hamiltonian, meaning that the anharmonicity is necessary for simulating 2DIR spectra. By Examining carefully, we find that the cross peaks between rocking (R' and R) and scissoring mode (X) are different with other cross peaks. For instance, $C_{R',X}$ peak exhibits only a negative signal and $C_{R',U}$ peak shows a pair of negative and positive signals. We states that this phenomenon comes from the anharmonic coupling between rocking and scissoring mode due to the same E symmetry. In summary, the cross peaks in the spectrum indicate the necessity for anharmonic calculations, and the anharmonic coupling between vibrational modes can be identified.

5.4.2 Stretching region

In the stretching region, the sensitivity of N-H stretching to the intermolecular hydrogen bonds offers a insight in the difference of those MA systems. The nine unassigned peaks of D1 to D9 in Fig.5.2 also can be identified by the 2DIR spectra. Fig.5.4 (a) depicts the 2DIR spectra in the N-H stretching region. The spectrum exhibits complex spectra pat-

doi:10.6342/NTU202404353

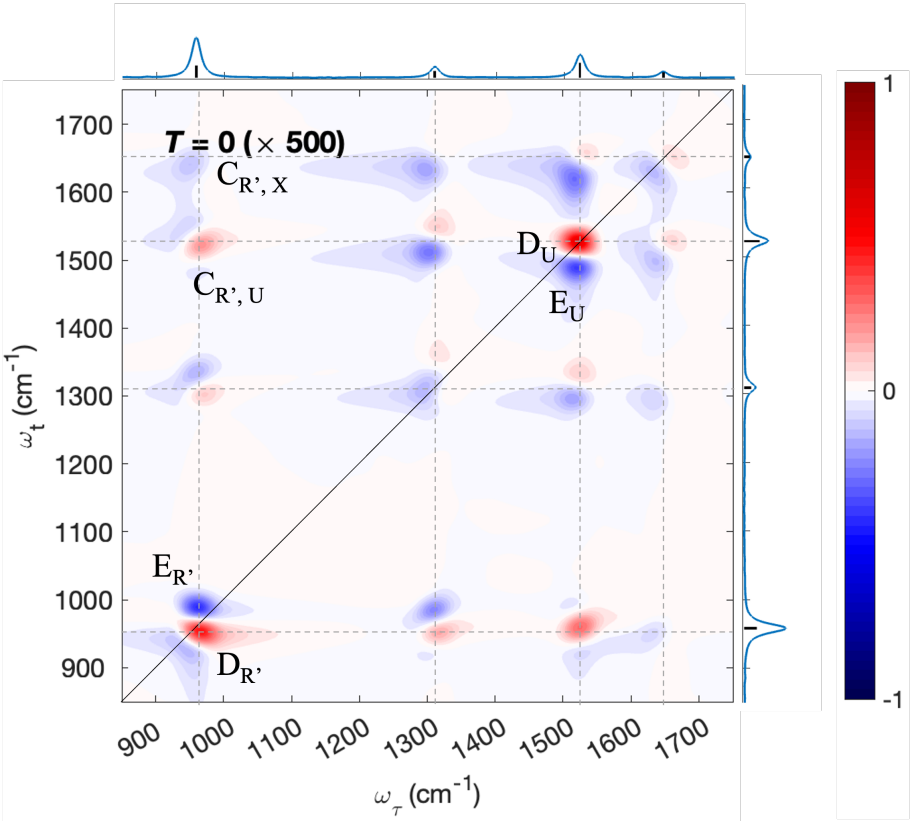

Figure 5.6: The theoretical 2DIR spectra of $(HBr)_3$-tagged MA in the bending region with FWHM of 40 fs in the laser pulses.

doi:10.6342/NTU202404353

terns compared with the spectrum in the bending region. We assign carefully to provide completed understanding of the spectrum. First, we inspect the diagonal peaks.

The diagomal peaks are identified by the peak positions in FTIR spectrum. From the diagonal peaks, we can look into the meaning of ESA and cross peaks. Due to the tranistion dipoles to the fourth power in 2DIR spectroscopy, the combination tones and the overtones exhibits weak intensities in the diagonal peaks. The prominent peaks around 3150 cm^{-1} present complex pattern because of interferences with ESA peaks, where the N-H stretching fundamentals, $|S_1\rangle$, are expected.

Subsequently, the cross peaks and the ESA peaks provide detailed understanding of anharmonic couplings within MA systems. In the upper left of the spectrum, the cross peaks between prominent peaks and combination tones are identified. We speculate the intensity are stemmed from the one quanta transition within the N-H stretching modes.

For example, the Liouville pathways related to the positive $C^{+}_{R'X,D}$ peak are considered as GSB and SE pathways involving both $|R'X\rangle$ and $|S_1\rangle$. The negative $C^{-}_{R'X,D}$ are caused from the excited state absorption related to the combination tones compring rocking, scissoring and stretching modes, $|R'XS\rangle$. The position of positive and negative peaks are slightly different due to the anharmonic effect included in our effective Hamiltonian. The complementary peak $C^{-}_{D,R'X}$ located at the lower right of the spectra, which comes from the same mechanism of $C^{-}_{R'X,D}$ peak. Finally, the peak $D^{-}_{R'X}$ are stemmed from the coherence pathway, where the coherence comprising $|R'X\rangle$ and $|S_1\rangle$.

Therefore, we can plot a square consist of $D^{-}_{R'X}$, $C^{-}_{R'X,D}$ and $C^{-}_{R'X,D}$ that corresponds to the square quartet we introduce in the chapter 5. The square quartet is relatively large compared to those in hydronium systems and lies close to the positions of the positive cross

doi:10.6342/NTU202404353

and diagonal peaks. Here, we state that, because the energy of $|R'XS\rangle$ nearly equals to the energy of prominent peaks plus $|R'X\rangle$, the resonance condition of the Fermi resonance between $|R'X\rangle$ and $|S_1\rangle$ is not perfect due to the large energy gap. This offer a technique to identify the vibrational modes coupled to each other by ploting the square quartet of negative peaks.

The tail of ESA peaks along around $\omega_\tau = 3150$ cm^{-1}, which corresponds to the position of D1, D2 and D3 peaks, are observed. We observe that the peaks lie on the ω_τ axis at the position related to the D1 peak, but with weaker intensity. However, the pattern of ESA peaks are similar with that of the ESA peaks related to D2 and D3. Namely, the vibrational modes is similar with D2 and D3. Therefore, we assign that D1 peak belongs to symmetric N-H stretching according the ESA 2DIR spectrum. Subsequently, the ESA peaks form many small square quartets along the ω_τ axis at positions related to the D2 and D3 peaks with nearly equal intensity. Hence, the D2 and D3 are the doublet states caused from the Fermi resonance between anti-symmetric N-H stretching and bending overtones, $|UX\rangle$, in a perfect resonance condition.

5.5 2DIR spectra of $(HCl)_3$-tagged MA and $(HBr)(HCl)_2$-tagged MA

In this section, we discuss the difference of the 2DIR spectra between $(HBr)_3$-tagged, $(HCl)_3$-tagged and $(HBr)(HCl)_2$-tagged methylammoniumm to give a insight in the interaction between MA and the microscopic environment. Here, the three cases are compared at the same time to offer a completed picture in the difference.

doi:10.6342/NTU202404353

5.5.1 Bending region

The 2DIR spectra in the bending region are simulated with a Gaussian laser profile with a center frequency of 1300 cm^{-1} and a FWHM of 40 fs, as depicted in Fig.5.7. Fig.5.7 (a), (b) and (c) are $(HBr)_3$-tagged, $(HCl)_3$-tagged and $(HBr)_1(HCl)_2$-tagged MA, respectively. The assignment of $(HBr)_3$-tagged MA (Fig.5.7 (a)) can be found at Fig.5.6. The spectra of $(HCl)_3$-tagged and $(HBr)_1(HCl)_2$-tagged MA are nearly the same with $(HBr)_3$-tagged MA, which corresponds to our statement that the spectra in the bending region can't offer a meaningful insight of the intermolecular interactions. Despite the symmetry breaking in $(HBr)_1(HCl)_2$-tagged MA, the splittings of the rocking and bending fundamental peaks cannot be identified because the magnitude change from HBr to HCl is only slight.

The slight differences are in the $E_{U,X}$ peaks, which corresponds to the Fermi resonance in the prominent peaks in the stretching region we expected. However, due to the weaker magnitude of transition dipole moment of scissoring modes, the ESA peaks lack a meaningful structure to assign. The similarity of the spectra are expected. We consider that the comparsion of 2DIR spectra in the stretching region provide more information because the N-H stretchings are sensitive to intermolecular interactions. Therefore, we examine the spectra in the stretching region in the next subsection.

5.5.2 Stretching region

The 2DIR spectra in the stretching region are simulated using a Gaussian laser profile with a central frequency of 3000 cm^{-1} and a full width at half maximum (FWHM) of 5 fs, as shown in Fig.5.8. Figures ref2DIR MA 0 S (a), (b), and (c) correspond to

doi:10.6342/NTU202404353

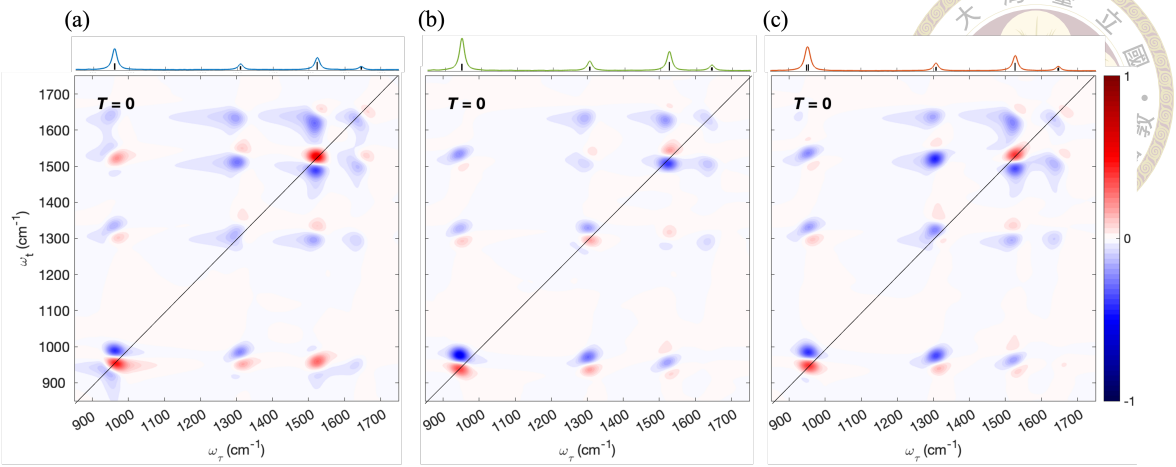

Figure 5.7: The theoretical 2DIR spectra of (a)$(HBr)_3$-tagged, (b)$(HCl)_3$-tagged and (a) $(HBr)_1(HCl)_2$-tagged MA at $T = 0$ in the bending region with FWHM of 40 fs in the laser pulses.

$(HBr)_3$-tagged, $(HCl)_3$-tagged, and $(HBr)_1(HCl)_2$-tagged MA, respectively. The spectral assignment for $(HBr)_3$-tagged MA, depicted in Fig.5.8 (a), can be found in Fig.5.6. We observe similar ESA tails and cross peaks between prominent peaks and combination tones, indicating that the relative energies in the states around the first excited stretching states do not significantly change. Moreover, the spectral features of the Fermi resonance are identified in the three cases. The most notable difference in the spectra is the peaks along $\omega_\tau = 3150$ cm^{-1}. We will examine this region in detail in the following sections.

To provide clear understanding, the energy levels of stretching $|S_2\rangle$ and combination tones $|b_2S_1\rangle$ are illustrated in Fig.5.9, which are important states related to the ESA tails. In Fig.5.8 (a), the ESA tail with identical intensities along positions of D2 and D3 peaks indicates the perfect the Fermi resonance condition we have mentioned in above. The spectrum of $(HCl)_3$-tagged MA, depicted in Fig.5.8 (b), presents an ESA tail with more intensity on the right-hand side, which agrees with the energy of the excited state transition related to stretching overtones. Therefore, the D4 peak is assigned with anti-symmetric N-H stretching modes and D3 peak is assigned with symmetric N-H stretching mode and

doi:10.6342/NTU202404353

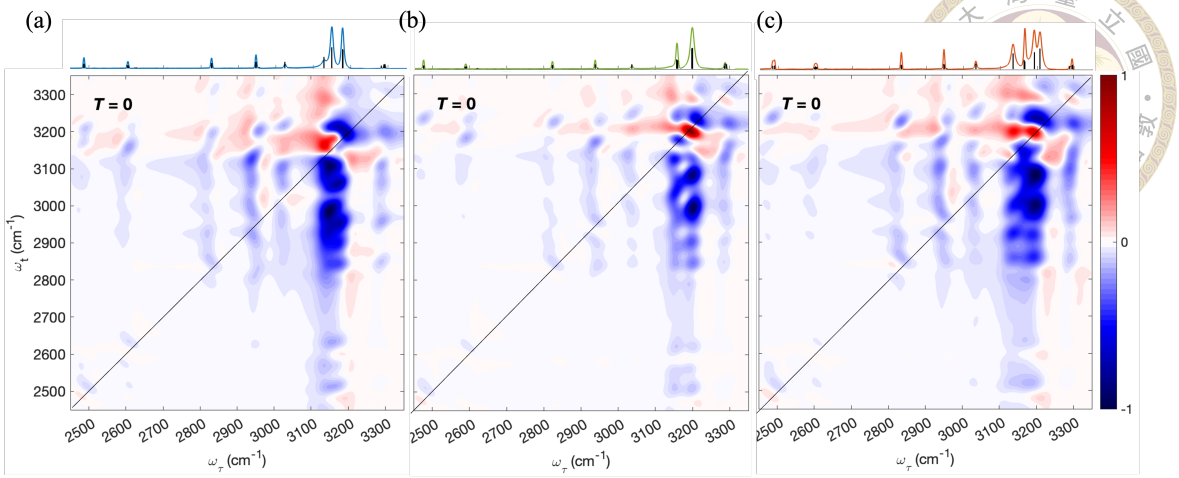

Figure 5.8: The theoretical 2DIR spectra of (a)$(HBr)_3$-tagged, (b)$(HCl)_3$-tagged and (a) $(HBr)_1(HCl)_2$-tagged MA at $T = 0$ in the stretching region with FWHM of 40 fs in the laser pulses.

bending overtones, $|UX\rangle$.

Here, we obtain the rough positions of stretching fundamentals, which are tuned by the hydrogen bondings beteen hydrogen hailde and NH_3^+ moiety, from theoretical 2DIR spectra in stretching region. The energy of the N-H stretching fundamental is higher in $(HCl)_3$-tagged MA system than that in $(HBr)_3$-tagged MA system. The phenomenon indicates the hydrogen bondings between HCl and NH_3^+ moiety are stronger than the between HBr and NH_3^+ moiety. The results mean that we are able to use 2DIR in the N-H stretching region to identify qualitatively the interactions related to MA molecules, the microscopic environment related to MA molecules.

The spectra of $(HBr)_1(HCl)_2$-tagged MA depicted in Fig.5.8 (c) also exhibits the ESA peaks with more intensity in the right-hand side. However, in this spectral resolution, because the ESA and coherence signals are dominant, we can't assign the D6, D7, D8 and D9 peaks clearly. Because vibrational relaxation, we suggest that the spectra at longer population time are able to distinguish $(HBr)_1(HCl)_2$-tagged MA with the other systems.

doi:10.6342/NTU202404353

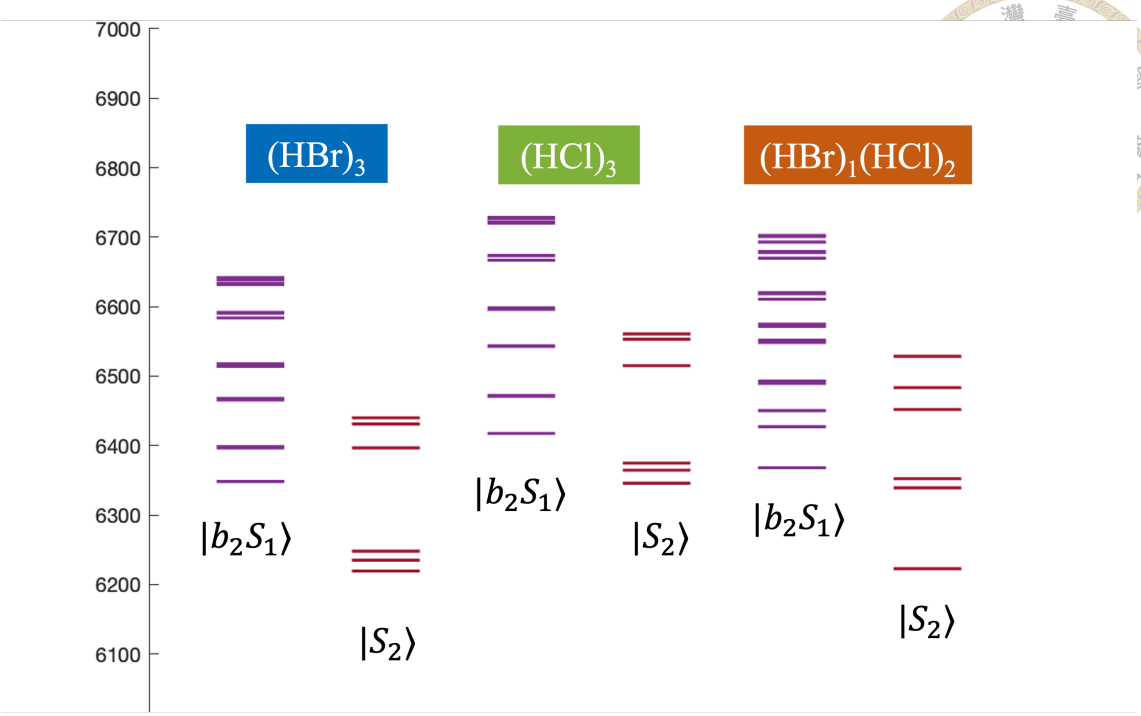

Figure 5.9: The energy levels of stretching overtones ($|S_2\rangle$) and combination tones ($|b_2S_1\rangle$) of $(HBr)_3$-tagged (left), $(HCl)_3$-tagged (middle) and $(HBr)_1(HCl)_2$-tagged MA (right).

Fig.5.10 depicts the 2DIR spectra at $T = 1000$ fs. In those spectra, the positive peaks are clearly indentified because the viberational relaxation induces the intensity decreasing of ESA and coherence signals. The spectrum of $(HBr)_1(HCl)_2$-tagged MA are shows broader square quartets around 3150 cm^{-1} at diagonal with small peaks located at 3120 cm^{-1} related to D6 peak. Therefore, we assign D6 peak as the symmetric N-H stretching, which is the most important spectral features in this case because the symmetric breaking in mixed hydrogen halide-tagged MA causes the significant dipole change in the vibrational mode. Namely, based on our results, the mixed lead-halide MA perovskite should be observed the intensity increasing related to the pure lead-halide MA peroskite. Moreover, we assign the D7 peak as the bending overtones, $|UX\rangle$, and D8 and D9 peaks as the anti-symmetric N-H stretching according to the peaks intensity in the 2DIR spectrum. The spectra at $T = 1000$ fs also offer good distinguishment of $(HBr)_3$-tagged and $(HCl)_3$-tagged MA by the intensity distribution of square quartet of positive peaks. There-

doi:10.6342/NTU202404353

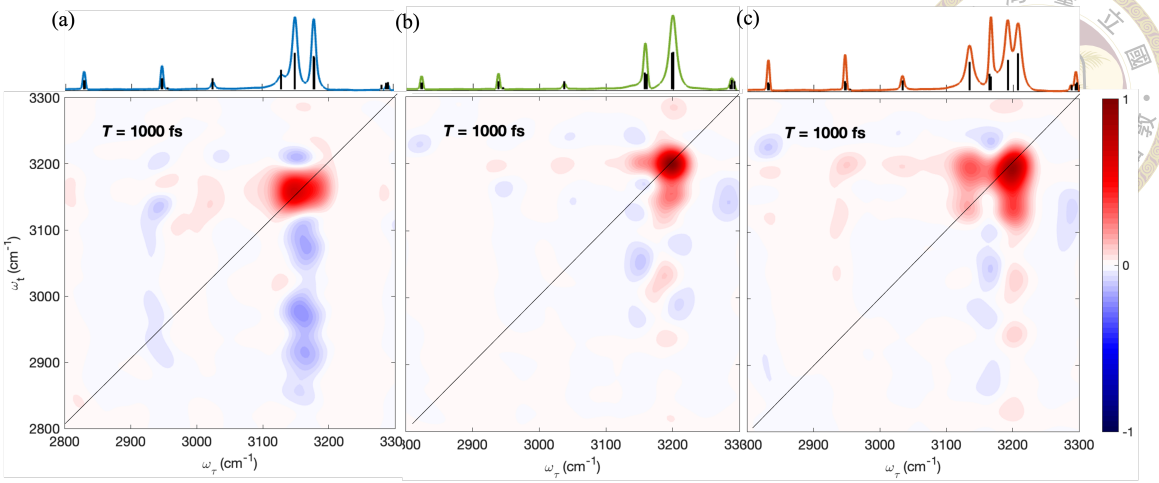

Figure 5.10: The theoretical 2DIR spectra of (a)$(HBr)_3$-tagged, (b)$(HCl)_3$-tagged and (a) $(HBr)_1(HCl)_2$-tagged MA at $T = 1000$ in the stretching region with FWHM of 40 fs in the laser pulses.

fore, from 2DIR spectra in the stretching region, the three systems have different spectral patterns but it is similar in the spectra in bending region.

In this section, we provide an example for the use of the spectral signatures of the Fermi resonance, which is applied on methylammonium systems. We suggest that the spectra of hydrogen halide-tagged MA can offer insight in the microsocpic environment of MA in the lead-halide perovskite. Therefore, we simulate the 2DIR spectra in the umbrella mode region to compare with the experimental spectra. The lineshape and dissipative dynamics manifested in the ESA peak intensity are consistent with both simulation and experimental results. However, the 2DIR spectra lack meaningful structure to provide detailed information about the microscopic environment in the perovskite. With confidence in our theoretical method, we proceed to simulate the 2DIR spectra in both the bending and stretching regions. In our results, the coherence pathways enhancing signals in the bending region and the similar spectral pattern in the three cases, $(HBr)_3$-tagged, $(HCl)_3$-tagged and $(HBr)_1(HCl)_2$-tagged MA, are observed. Subsequently, the spectra in stretching region offer the meaningful information of intermolecular interactions related

doi:10.6342/NTU202404353

to the Fermi resonance occuring in stretching fundamental and bending overtones. The difference of strength of hydrogen bondings between $(HBr)_3$-tagged and $(HCl)_3$-tagged MA is identified. Furthermore, the mixed case, $(HBr)_1(HCl)_2$-tagged MA, also exhibits significant signal in the symmetric N-H stretching that is unrecognizable in pure hydrogen halide-tagged cases. In summary, the results suggest our expectation in the 2DIR spectra in the stretching region provide insight in the microscopic environment of MA in perovskite.

doi:10.6342/NTU202404353

doi:10.6342/NTU202404353

Chapter 6 Non-Markovian Quantum Langevin Equation Approach

In the previous sections, we apply our theoretical approach of the Markovian quantum Schrödinger-Langevin equation on fully solvated hydronium and methylammonium systems. In Chapter 4, we treat the O-H stretching and bending modes of fully solvated hydronium as the reduced system, while treating the other vibrational modes as a Markovian bath. However, given that the Markovian approximation presumes the surrounding evolves much faster than the system, this assumption may not be reasonable for our specific system. The other vibrational modes, such as the hindered rotation and stretching of hydrogen bonds, evolve more slowly than the O-H stretching and bending modes. Therefore, the implement of non-Markovian quantum Schrödinger-Langevin equation is necessary.

6.1 Systems

In this section, with a focus on the validation of our approach under non-Markovian condition, we simulate dissipative dynamics, linear spectra and 2DIR spectra within single

doi:10.6342/NTU202404353

harmonic oscillator. In subsequent simulations, units are scaled according to the harmonic frequency of the system, ω_0. For 2DIR simulations, the anharmonicity causing overtone energy shifts set to $0.1\omega_0$ to clearly observe positive and negative signals in spectra.

6.2 Linear coupling model

In chpater 2, we have derived the quantum Langevin equation in the independent-oscillator (IO) model. However, we do not use the equation derived in chpater 2. The reason we will discuss in 6.2.3. In this chpater, we modify the independent-oscillator model to the linear coupling (LC) model. In LC model, we derive the quantum of motion in the Hamiltonian picture, which is similar with the quantum Langevin equation. The total Hamiltonian of LC model is written as

$$H = \frac{p^2}{2m} + V(x) + \sum_\alpha [\frac{p_\alpha^2}{2m_\alpha} + \frac{1}{2} m_\alpha \omega_\alpha^2 q_\alpha^2] + x \sum_\alpha \lambda_\alpha q_\alpha \tag{6.1}$$

where $x \sum_\alpha \lambda_\alpha q_\alpha$ represents that the system and bath modes are attached by springs.

By solving time derivative of operators in the Heisenberg picture, the equation of motion of the system can be denoted by the variables in the system degrees of freedom only.

$$\begin{aligned} m\frac{d^2x(t)}{dt^2} + V'(x) = &\sum_\alpha [g_\alpha m_\alpha \omega_\alpha^2 \cos(\omega_\alpha t) q_\alpha(0) + g_\alpha \omega_\alpha \sin(\omega_\alpha t) p_\alpha(0)] \\ &+ \int_0^t \sum_\alpha g_\alpha^2 m_\alpha \omega_\alpha^3 \sin(\omega_\alpha (t-\tau)) x(\tau) d\tau \end{aligned} \tag{6.2}$$

doi:10.6342/NTU202404353

Here, we assign the damping kernel $\Gamma(t)$ and the random force term $f(t)$.

$$f(t) = \sum_{\alpha} [g_\alpha m_\alpha \omega_\alpha^2 \cos(\omega_\alpha t) q_\alpha(0) + g_\alpha \omega_\alpha \sin(\omega_\alpha t) p_\alpha(0)]$$
$$\Gamma(t) = \sum_{\alpha} g_\alpha^2 m_\alpha \omega_\alpha^3 \sin(\omega_\alpha(t)) \tag{6.3}$$

We adopt Eq.6.2 for the following simulations.

$$m\frac{d^2x(t)}{dt^2} + V'(x) = f(t) + \int_0^t \Gamma(t-\tau)x(\tau)d\tau \tag{6.4}$$

To describe a stochastic process properly, we would introduce the time-correlation function of random forces $C_{ff}(t_2, t_1)$ and spectral density $J(\omega)$. By the definition,

$$\begin{aligned} C_{ff}(t_2,t_1) = \langle f(t_2)f(t_1)\rangle &= \sum_{\alpha} g_\alpha^2 m_\alpha^2 \omega_\alpha^4 \cos(\omega_\alpha t_2)\cos(\omega_\alpha t_1)\langle q_\alpha^2(0)\rangle \\ &+ \sum_{\alpha} g_\alpha^2 \omega_\alpha^2 \sin(\omega_\alpha t_2)\sin(\omega_\alpha t_1)\langle p_\alpha^2(0)\rangle \\ &+ \sum_{\alpha} g_\alpha^2 m_\alpha \omega_\alpha^3 \cos(\omega_\alpha t_2)\sin(\omega_\alpha t_1)\langle q_\alpha(0)p_\alpha(0)\rangle \\ &+ \sum_{\alpha} g_\alpha^2 m_\alpha \omega_\alpha^3 \sin(\omega_\alpha t_2)\cos(\omega_\alpha t_1)\langle p_\alpha(0)q_\alpha(0)\rangle \end{aligned} \tag{6.5}$$

Here, the averages of initial position and momentum operators need to be solved. For simplification, we only show the detailed derivation of $\langle q_\alpha^2(0)\rangle$. With the ladder operator adopted in a harmonic oscillator system, the position and momentum operator rewritten

doi:10.6342/NTU202404353

as $q_\alpha = \sqrt{\frac{\hbar}{2m_\alpha\omega_\alpha}}(b_\alpha^\dagger + b_\alpha)$, $p_\alpha = i\sqrt{\frac{\hbar m_\alpha\omega_\alpha}{2}}(b_\alpha^\dagger - b_\alpha)$. Then,

$$\begin{aligned}
\langle q_\alpha^2(0)\rangle &= \frac{\hbar}{2m_\alpha\omega_\alpha}\langle[(b_\alpha^\dagger(0) + b_\alpha(0))(b_\alpha^\dagger(0) + b_\alpha(0))]\rangle \\
&= \frac{\hbar}{2m_\alpha\omega_\alpha}\langle[b_\alpha^\dagger(0)b_\alpha^\dagger(0) + b_\alpha^\dagger(0)b_\alpha(0) + b_\alpha(0)b_\alpha^\dagger(0) + b_\alpha(0)b_\alpha(0)]\rangle \\
&= \frac{\hbar}{2m_\alpha\omega_\alpha}[\overline{n}_\alpha + \overline{n}_\alpha + 1] \\
&= \frac{\hbar}{2m_\alpha\omega_\alpha}(2\overline{n}_\alpha + 1)
\end{aligned} \tag{6.6}$$

where $\overline{n}_\alpha$ is the average occupation number of the bath mode α in the thermal equilibrium state. For $\overline{n}_\alpha = \frac{1}{e^{\beta\hbar\omega_\alpha}-1}$ derived from the Boltzmann distribution,

$$\begin{aligned}
\langle q_\alpha^2(0)\rangle &= \frac{\hbar}{2m_\alpha\omega_\alpha}\coth\left(\frac{\beta\hbar\omega_\alpha}{2}\right) \\
\langle p_\alpha^2(0)\rangle &= \frac{\hbar m_\alpha\omega_\alpha}{2}\coth\left(\frac{\beta\hbar\omega_\alpha}{2}\right) \\
\langle q_\alpha(0)p_\alpha(0)\rangle &= -\langle p_\alpha(0)q_\alpha(0)\rangle = \frac{1}{2}i\hbar
\end{aligned} \tag{6.7}$$

Due to the property, time translation invariance, of time correlation. the time-correlation function can be further simplified as

$$\begin{aligned}
C_{ff}(t_2, t_1) &= C_{ff}(t_2 - t_1, 0) = C_{ff}(\tau, 0) \\
&= \sum_\alpha \frac{\hbar}{2}g_\alpha^2 m_\alpha\omega_\alpha^3\cos(\omega_\alpha\tau)\coth\left(\frac{\beta\hbar\omega_\alpha}{2}\right) \\
&- \sum_\alpha \frac{i\hbar}{2}g_\alpha^2 m_\alpha\omega_\alpha^3\sin(\omega_\alpha\tau)
\end{aligned} \tag{6.8}$$

Then, we define the spectral density.

$$J(\omega) = \sum_\alpha g_\alpha^2 m_\alpha\omega_\alpha^3\delta(\omega - \omega_\alpha) \tag{6.9}$$

Finally, the damping kernel and the time-correlation function of random forces can be

doi:10.6342/NTU202404353

represented by the spectral density.

$$C_{ff}(t) = \int_0^\infty \frac{\hbar}{2} J(\omega)\cos(\omega t)\coth\left(\frac{\beta\hbar\omega}{2}\right)d\omega - \int_0^\infty \frac{i\hbar}{2} J(\omega)\sin(\omega t)d\omega$$
$$\Gamma(t) = \int_0^\infty J(\omega)\sin(\omega t)d\omega \tag{6.10}$$

In addition, the result shows the imaginary part of the time-correlation function of random forces is related to the friction kernel.

The Drude-Lorentz spectral density is widely adopted,

$$J_{DL}(\omega) = m\gamma\omega\frac{\omega_c^2}{\omega^2+\omega_c^2} \tag{6.11}$$

where γ and ω_c represent the coupling strength and the cut-off frequency, respectively. Here, we apply Drude-Lorentz spectral density to investigate the dissipative dynamics in the following simulation. Therefore, the friction kernel can be written as

$$\begin{aligned}\Gamma(t) &= \int_0^\infty J(\omega)\sin(\omega t)d\omega \\ &= \frac{m\gamma\omega_c^2\pi}{2} sgn(\tau)e^{-\omega_c\tau}\end{aligned} \tag{6.12}$$

According to 2.20, the non-Markovian Schrödinger-Langevin equation is shown

$$i\hbar\frac{\delta\psi(x,t)}{\delta t} = [H + \sum_i F_i(t)]\psi(x,t) \tag{6.13}$$

where H and $F_i(t)$ denote the system Hamiltonian and friction operator in the ith dimension. The friction operator is cast by the random forces and dampling kernel, and the displacement of the wavepacket.

$$F_i(t) = [-f_i(t) - \int_0^t \Gamma_i(t-\tau)\langle x_i\rangle(\tau)d\tau](x_i - \langle x_i\rangle(t)) \tag{6.14}$$

doi:10.6342/NTU202404353

6.2.1 Dissipative dynamics

To inspect rationality of our theoretical approach, we simulate the dissipative dynamics in a harmonic oscilltor. In Fig.6.1, the simulated dissipative dynamics in a harmonic oscillator are shown, where the initial state is set as a superposition of first and second excited states, $|e_1\rangle + |e_2\rangle$. The cutoff frequencies are set to 1 and 0.1 , and the coupling strengths are set to 0.001 and 0.05 in Fig.6.1 (a) and (b), respectively, demonstrating the effect of energy matching and mismatching between the system and bath modes. The friction coefficient is set to 9×10^{-4} in the Markovian case. The values of coupling strengths and friction coefficient are set based on the same timescales in vibrational relxations.

The interpretation of dissipative dynamics provide us the information of the physical picture included in our theoretical method. Aside from the minor fluctuation in the population of second excited state, the trends of dissipative dynamics remain consistent across three cases in Fig.6.1(a), (b) and (c). The minor fluctuation results from the coherence between first and second excited states induced by bath modes. The major feature of the dynamics is the consecutive relaxation pathway. It is important to note that the larger value of coupling strength is adopted in $omega_c = 0.1$ case because the energy mismatching between bath mode and the system, which means the reasonance energy transfer is included in our method. In summary, the dynamics induced from non-Markovian bath exhibit reasonable relaxation behavior, which indicate the validity of our theoretical approach.

6.2.2 Linear spectrum

The simulated linear spectrum provides insights into not only the relaxation dynamics but also the potential energy surface (PES) of the system. Fig.6.2 illustrates the simulated

doi:10.6342/NTU202404353

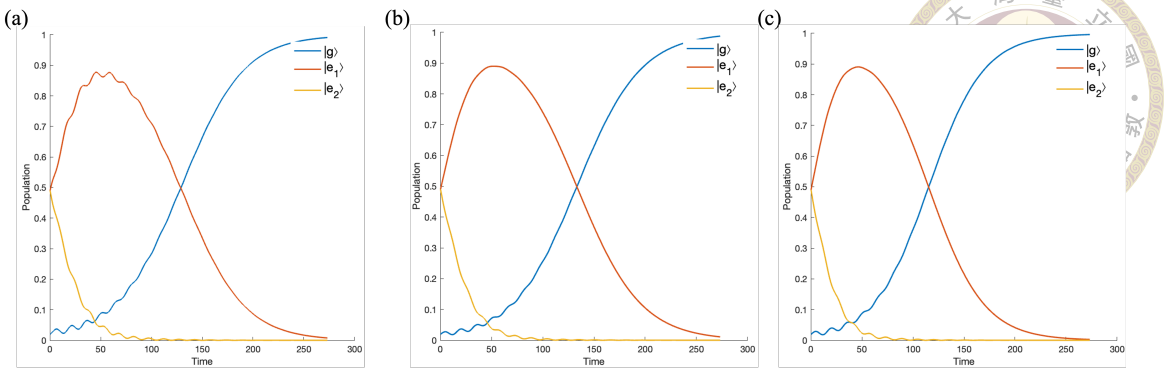

Figure 6.1: The dissipative dynamics in a harmonic oscillator model(a)for a non-Markovian case $\omega_c = 1$(b)for a non-Markovian case $\omega_c = 0.1$ (c)for a Markovian case

linear spectra for non-Markovian and Markovian baths, respectively. For same reasons, in Fig.6.2 (a) and (b), the cutoff frequencies for the non-Markovian bath are set to 1 and 0.1, respectively, while the coupling strengths are adjusted to 0.005 and 0.25. In the Markovian limit, the friction coefficient is set to 0.005, as shown in Fig.6.2 (c).

The lineshapes and peak positions offer the detailed information on relaxation dynamics. In Fig.6.2, the linewidths remain approximately the same in our simulation, owing to the adopted coupling strengths. The peak position of Fig.6.2 (a) exhibits a red shift of about 0.002 ω_0 which indicates the reorganization of the PES of the harmonic oscillator model caused by the system-bath coupling. We contend that the energy matching between bath modes and system results a significant reorganization effect observable in the simulated linear spectra. However, an asymmetric lineshape, which is typically expected in non-Markovian dynamics, was not observed in our simulation, possibly due to its subtle manifestation. In summary, the simulations of dissipative dynamics and linear spectra roughly shows expected features that indicate the rationality of our theoretical approach. In the following section, we plan to simulate the real system of N_2-tagged hydronium, as the infrared spectra approximately exhibit characteristics of a single-mode feature.

doi:10.6342/NTU202404353

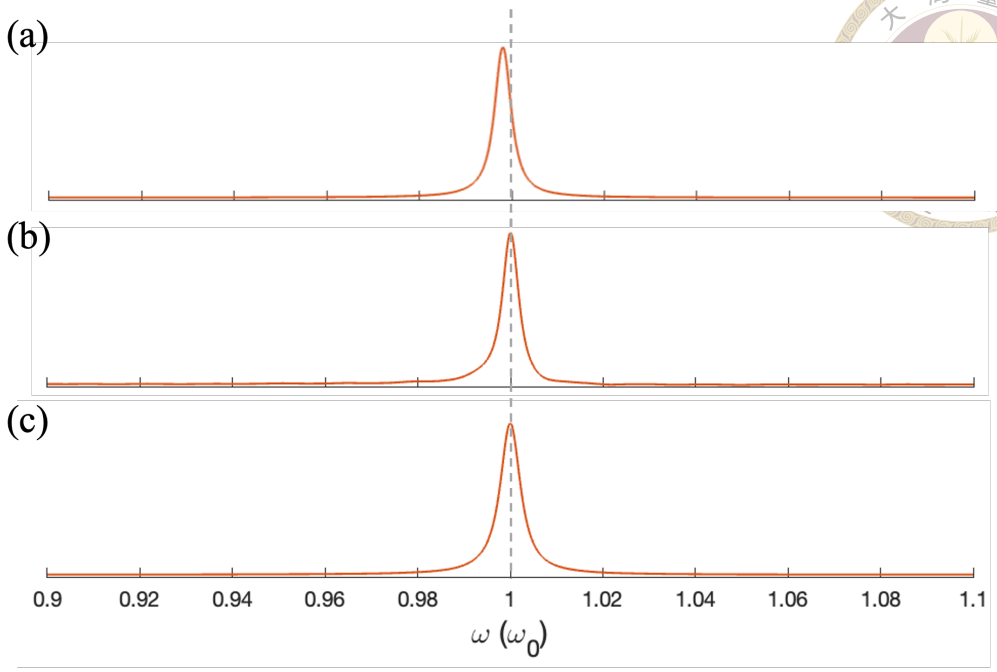

Figure 6.2: The linear spectra in a harmonic oscillator model(a)for a non-Markovian case $\omega_c = 1$(b)for a non-Markovian case $\omega_c = 0.1$ (c)for a Markovian case

6.2.3 Independent oscillator model

The independent oscillator (IO) model plays an important role in deriving the Langevin equation and provides a macroscopic description of a system coupled with a heat bath.[35, 36] Ford et al. proposed that the IO model is a simple and general model that can also be incorporated into many other models, such as the velocity-coupling model.[36] Moreover, they stated that the linear-coupling (LC) model is not passive, which is a serious problem in thermodynamics. It's worth discussing why we chose the linear-coupling model instead of the independent oscillator model. Therefore, in this subsection, we demonstrate the reasons to rationalize the theoretical method we established.

In Fig.6.3, we simulate the dissipative dynamics and linear spectrum using the quantum Schrödinger-Langevin equation (QSLE) derived from IO model in Eq.2.20 with a cutoff frequency of 0.1 and a coupling strength of 0.05, as a comparision with Fig.6.1 (b)

doi:10.6342/NTU202404353

and Fig.6.2 (b). In the dissipative dynamics, the population of $|e_1\rangle$ and $|e_2\rangle$ shows a faster vibrational relxation compared with 6.1 (b). Moreover, in this QSLE, employing the same cutoff frequency and coupling strength results in a more significant system-bath coupling, leading to coherence between $|e_1\rangle$ and $|e_2\rangle$, which is manifested by oscillating features in the early-period dynamics. For the linear spectum, the lineshape exhibits roughly the same feature compared with Fig.6.2 (b). However, the significant blue shift is observed in Fig.6.3 (b), which indicates the counter term, reorganize the fundamental frequency of the system, manifesting on the linear spectrum.

Tracing back to the assumption of our theoretical method, we treat the other vibrational modes, such as the stretching of hydrogen bonds, as the surrounding with a focus on the modes contributing the Fermi resonance. The effective Hamiltonian is constructed from the *ab initio* calculation. Nevertheless, the *ab initio* calculation should include the energy shifting induced from the anharmonic couplings between vibrational modes. Therefore, we didn't utilize the independent oscillator model in our simulation. We only consider the dissipative part caused from other vibrational modes, where we adopt the bilinear coupling term incoded in the linear-coupling model.

6.3 2DIR spectra in one vibrational mode

The 2DIR spectra provide information in both the frequency and time domains. We can use the center line slope (CLS) to extract the memory effect encoded in our non-Markovian SQLE approach.[46] The center line is determined from the maximum of ω_τ

doi:10.6342/NTU202404353

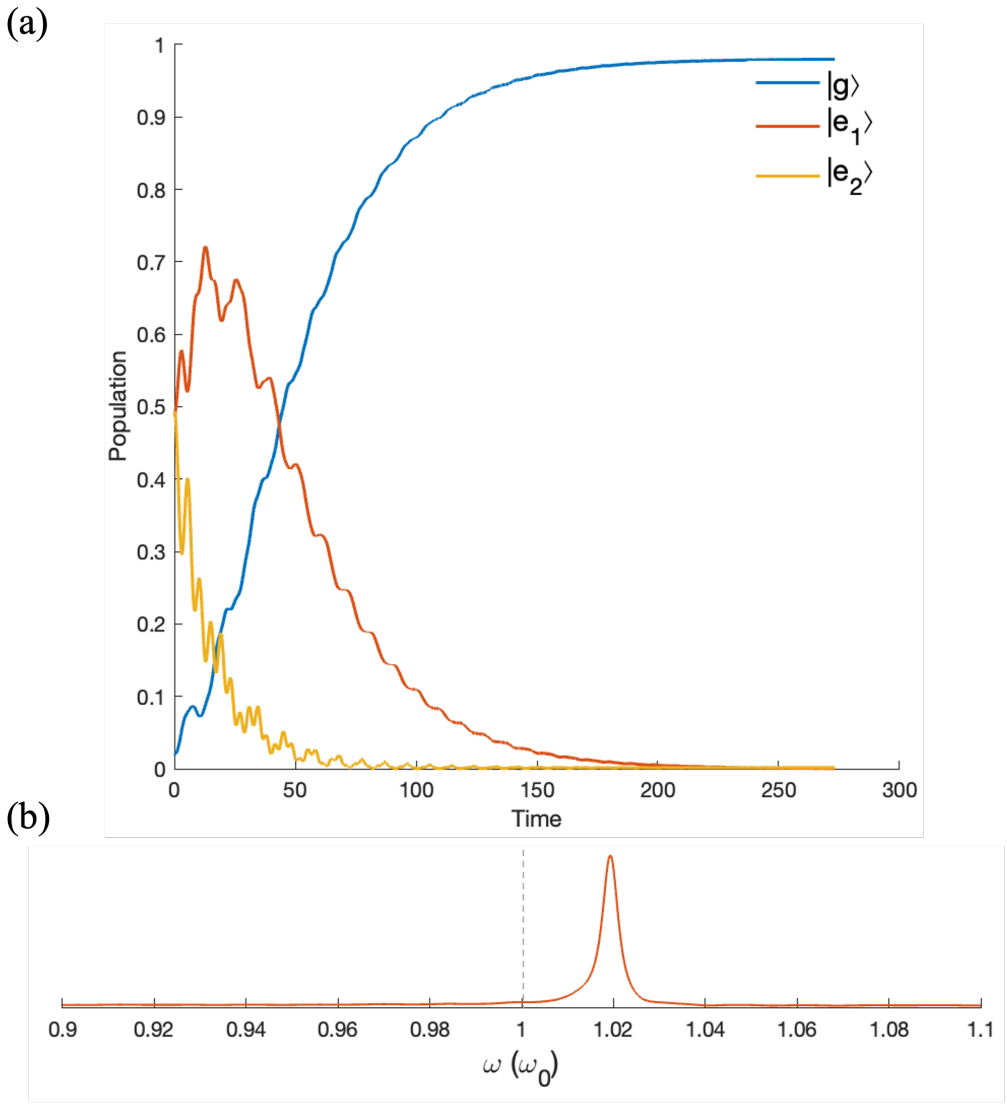

Figure 6.3: (a)The dissipative dynamics in a harmonic oscillator model with the QSLE from IO model $\omega_c = 0.1$ (b)The theoretical linear spectrum in a harmonic oscillator model with the QSLE from IO model ω_c are set to 0.1 in the both simulations.

doi:10.6342/NTU202404353

at each ω_t. The slope of center line, $S(T)$, can expressed as follow

$$S(T) = \frac{1}{C_1^N(T)}$$
$$C_1^N(T) = \frac{\langle \delta\omega(T)\delta\omega(0)\rangle}{C_1(0)} \tag{6.15}$$

where the ω is the transition frequency corresponding to the peak and $C_1^N(T)$ is normalized frequency-frequency correlation function (FFCF). Specifically, CLS is inversely proportional to FFCF. For instance, in the Markovian limit, the CLS is infinite due to the memoryless nature of FFCF. In the following, we carefully examine the theoretical 2DIR spectra simulted from the non-Markovian SQLE approach in Fig.6.5 and 6.6. We treat the spectra simulated from Markovian SQLE approach as the control group. Therefore, we don't detaily elaborate the Fig.6.4.

The system we chose is a single vibrational mode, where the potential energy surface (PES) consists of a harmonic quadratic term plus anharmonic terms that cause overtone energy shifts. Fig.6.5 depicts the theoretical 2DIR spectra at several population times. The cutoff frequency and coupling strength are set to 0.02 and 1, respectively.

The 2DIR spectra at $T = 0$ in Fig.6.5 shows red and blue peaks that corresponding to the transition of ground states to first excited state and first excited state to sencond excited state, respectively. Those peaks exhibits Lorentzian lineshape with a star pattern and a vertical center line. Additionally, the peak intensities decrease over a timescale of approximately 100 fs at different population times. However, we do not observe a decrease in the center line slope, which would reveal the memory information. We speculate that this is because the friction force is coupled with the position operator of the system, resulting in insignificant energy fluctuations. Consequently, the center lines of these peaks remain vertical in our simulations.

doi:10.6342/NTU202404353

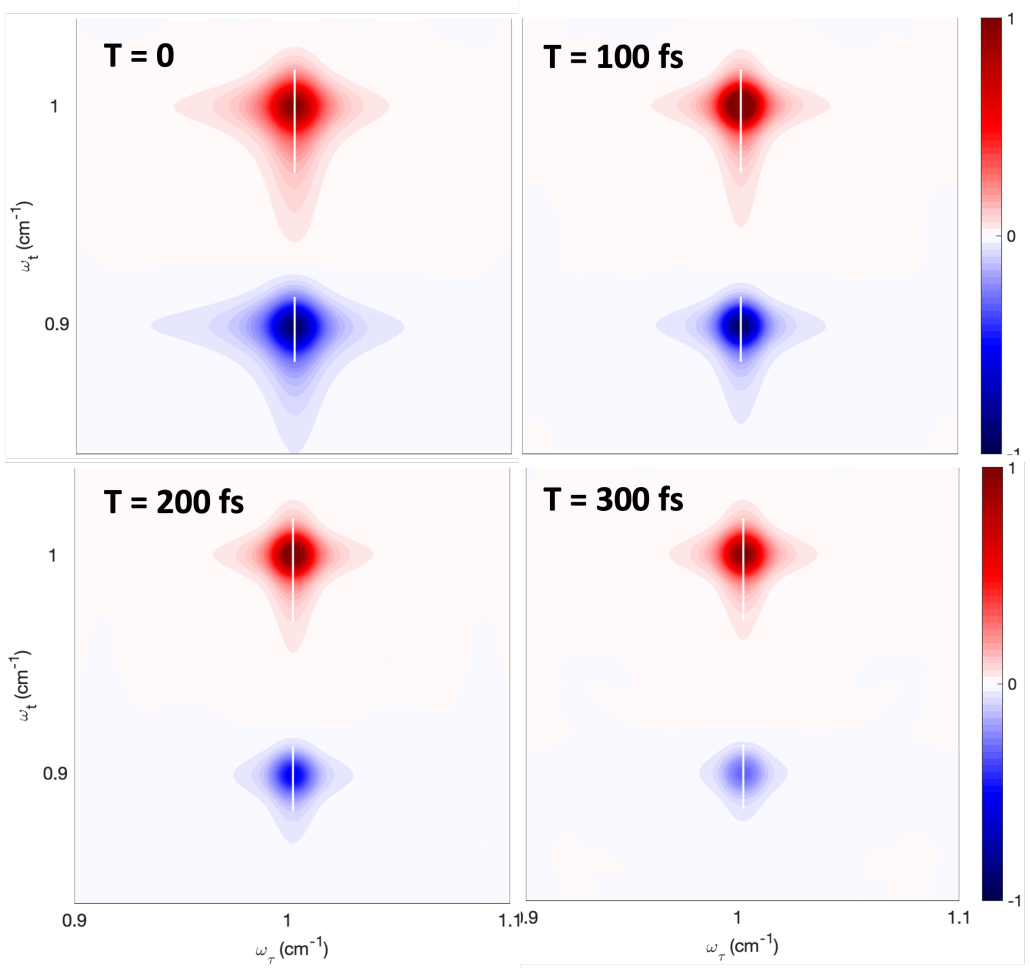

Figure 6.4: The simulated 2DIR at T=0, 100, 200, 300, respectively, with the SQLE of the Markovian form. The friction coefficient is set to 0.01.

doi:10.6342/NTU202404353

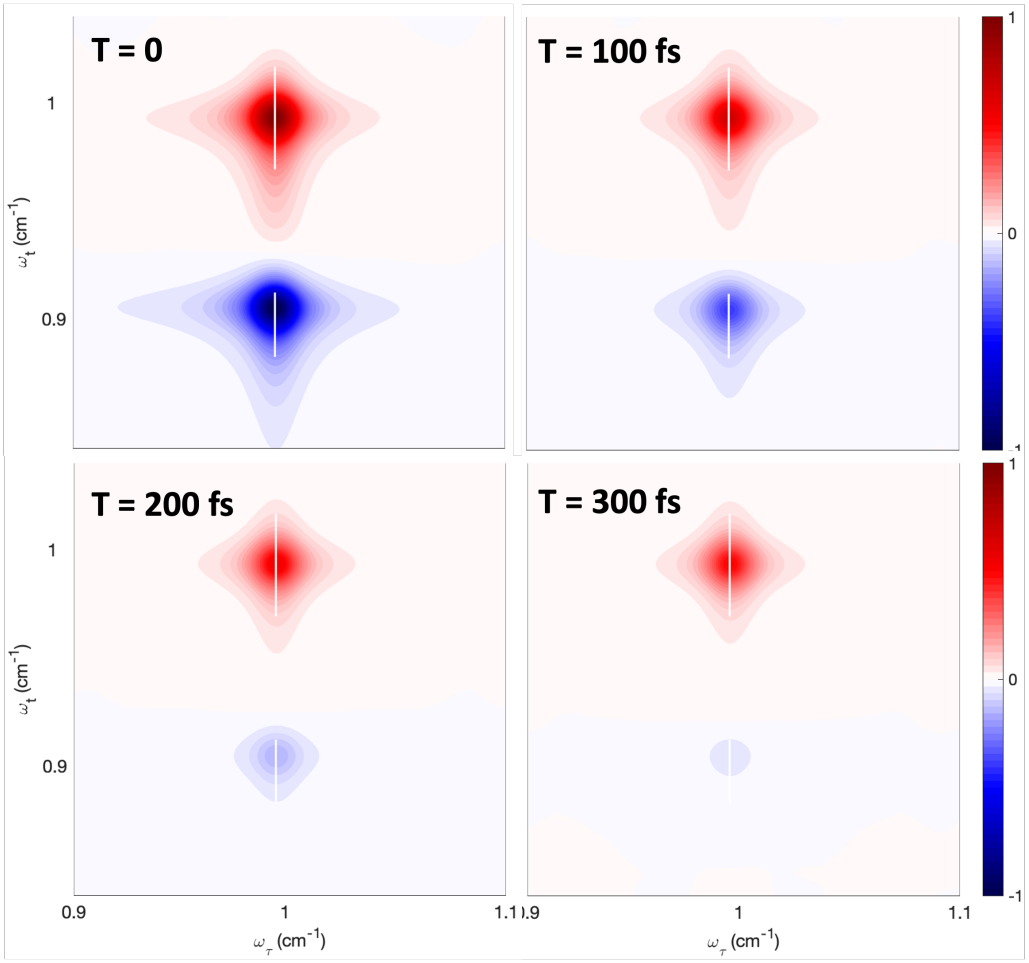

Figure 6.5: The simulated 2DIR at T=0, 100, 200, 300, respectively, with the SQLE of the Markovian form. The cutoff frequency and coupling strength are set to 0.02 and 1,respectively.

doi:10.6342/NTU202404353

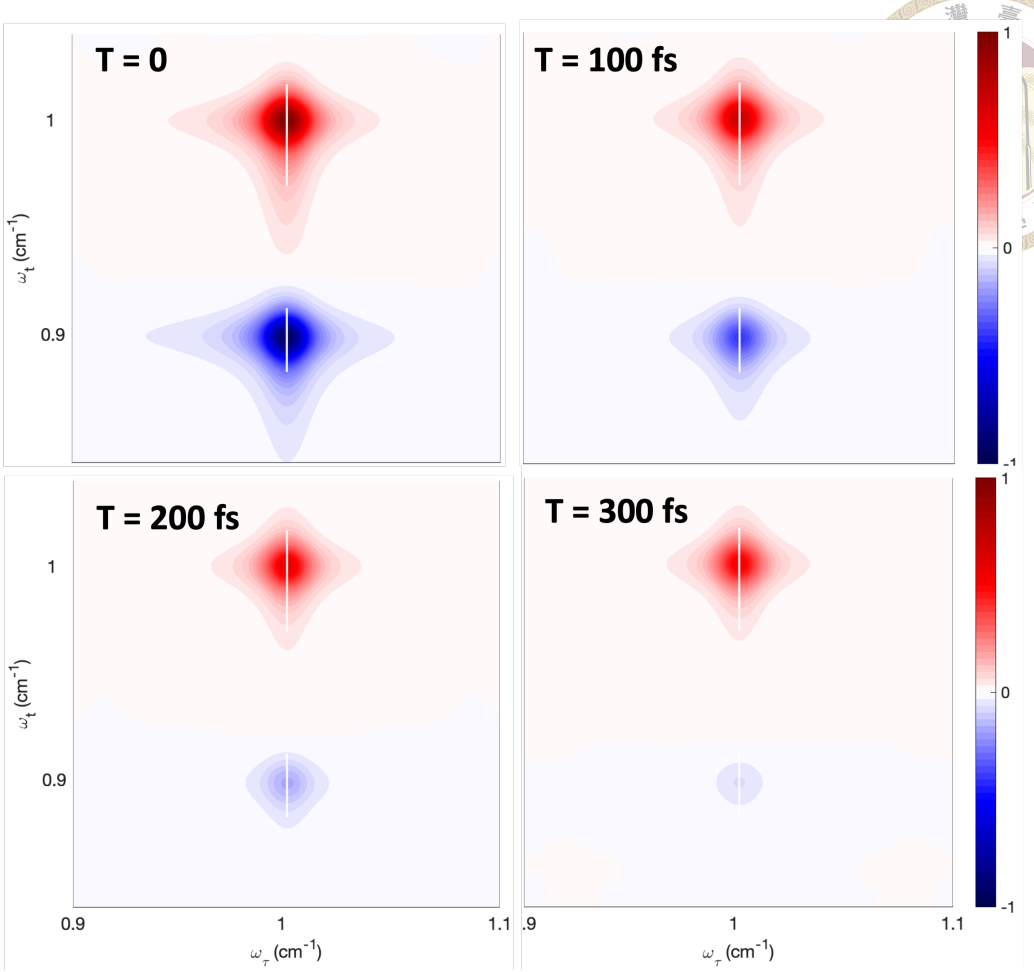

Figure 6.6: The simulated 2DIR at T=0, 100, 200, 300, respectively, with the SQLE of the Markovian form. The cutoff frequency and coupling strength are set to 1 and 0.1,respectively.

In Fig.6.6, the theoretical 2DIR spectra at different population time are illustrated. The cutoff frequency and coupling strength are set to 1 and 0.1, respectively. Compared to Fig.6.5, where the coupling strength is increased to a significant value to induce vibrational relaxation within the same timescale, which we also mentioned in the FTIR part, the spectra present an almost identical pattern. This similarity suggests that we still do not observe the memory effect in our simulations. Consequently, we discuss future work in the following paragraph.

In this chapter, we validate our non-Markovian SQLE approach derving from the linear-coupling model by simulating dissipative dynamics, FTIR and 2DIR spectra in a

doi:10.6342/NTU202404353

vibrational mode. In those simulation, we observe vibrational relaxation processes. However, we do not observe the asymmetric lineshape in FTIR and 2DIR spectra and the relxation of center line slope in 2DIR, which represents we are not sure that we have incorporated non-Markovian dynamics in our simulation. About the future work, we need to re-examine the friction operator we cast in SQLE and carefully review the approximation using in our theoretical approach.

doi:10.6342/NTU202404353

doi:10.6342/NTU202404353

Chapter 7 Conclusion

In the thesis, the application of 2DIR spectroscopic simulation on the Fermi resonance systems, solvated hydronium and methylammonium, are conducted by the theoretical method combining the Schrödinger-Langevin Equation and *ab initio* calculation. The spectral signitures, square quartets and quantum beating, of the Fermi resonance on 2DIR spectra are identified. Moreover, the microscopic envionment of molecules can be probed by the Fermi resonance which we have investigated in hydrogen halide-tagged methylammonium systems. Finally, the theoretical method is improved by apply the non-Markovian form of the quantum Langevin equation. The further investigation and validation are required in the future work.

In chapter 1, we review the development of vibrational spectroscopy with a fous on solute-solvent complex. The experiment and theoretical approach of 2DIR is introduced to point out the necessity of our method with perturbation scheme and wavefuntion-based propagation, which benefits exactly wavepacket dynamics on a complex potential energy surface. Subsequently, the importance of the Fermi resonance is discussed from the aspect of signitures on 2DIR spectrum. Finally, We examine the evolvement on solvated hydronium and methylammonium systems to study and provide a perspective related to microscopic envionment of molecules in a crystal.

doi:10.6342/NTU202404353

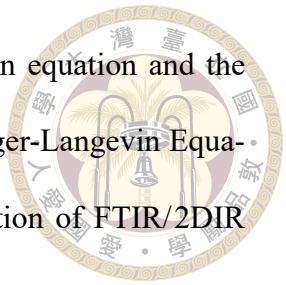

In chapter 2, we start from the derivation of quantum Langevin equation and the Gaussian wavepacket approximation to exactly explain the Schrödinger-Langevin Equation that we use in all simulations. Then, in chapter 3, the simulation of FTIR/2DIR spectroscopy is detailly introduced.

The 2DIR spectra of solvated hydronium are discuessed in chpater 4. From the comparision between Ar-tagged and N_2-tagged hydroniums, we identify the signatures of the Fermi resonance, square quartets and quantum beatings. In chapter 5, the examine the 2DIR spectra of pure and mixed hydrogen halide-tagged methylammonium. With the known spectral features of the Fermi resonance, we can qualitatively observe the interaction between methylammonium and surrounding atoms or molecules.

Lastly, we validate the theoretical method in non-Markovian condition in a harmonic mode in chapter 6. Because the common features of non-Markovian dynamics are not observed, the further investigation and study are necessary in the future work.

doi:10.6342/NTU202404353

References

[1] Levering, L. M.; Sierra-Hernandez, M. R.; Allen, H. C. Observation of Hydronium Ions at the air- aqueous acid Interface: vibrational spectroscopic studies of aqueous HCl, HBr, and HI. *J. Phys. Chem. C* **2007**, *111*, 8814–8826.

[2] Sherman, S. L.; Fischer, K. C.; Garand, E. Conformational changes induced by methyl side-chains in protonated tripeptides containing glycine and alanine residues. *J. Phys. Chem. A* **2022**, *126*, 4036–4045.

[3] Li, J.-W.; Morita, M.; Takahashi, K.; Kuo, J.-L. Features in vibrational spectra induced by Ar-tagging for H_3O^+ Arm, m= 0–3. *J. Phys. Chem. A* **2015**, *119*, 10887–10892.

[4] Kim, Y. S.; Hochstrasser, R. M. Chemical exchange 2D IR of hydrogen-bond making and breaking. *PNAS* **2005**, *102*, 11185–11190.

[5] Fournier, J. A.; Carpenter, W. B.; Lewis, N. H.; Tokmakoff, A. Broadband 2D IR spectroscopy reveals dominant asymmetric $H_5O_2^+$ proton hydration structures in acid solutions. *Nat. Chem* **2018**, *10*, 932–937.

[6] Zheng, J.; Kwak, K.; Fayer, M. Ultrafast 2D IR vibrational echo spectroscopy. *Acc. Chem. Res.* **2007**, *40*, 75–83.

doi:10.6342/NTU202404353

[7] Khalil, M.; Demirdöven, N.; Tokmakoff, A. Coherent 2D IR spectroscopy: Molecular structure and dynamics in solution. *J. Phys. Chem. A* **2003**, *107*, 5258–5279.

[8] Zheng, J.; Kwak, K.; Asbury, J.; Chen, X.; Piletic, I. R.; Fayer, M. D. Ultrafast dynamics of solute-solvent complexation observed at thermal equilibrium in real time. *Sci.* **2005**, *309*, 1338–1343.

[9] Maiti, K. S. Ultrafast N–H vibrational dynamics of hydrogen-bonded cyclic amide reveal by 2DIR spectroscopy. *Chem. Phys.* **2018**, *515*, 509–512.

[10] Feng, C.-J.; Tokmakoff, A. The dynamics of peptide-water interactions in dialanine: An ultrafast amide I 2D IR and computational spectroscopy study. *J. Chem. Phys.* **2017**, *147*.

[11] Greve, C.; Nibbering, E. T.; Fidder, H. Hydrogen-bonding-induced enhancement of Fermi resonances: A linear IR and nonlinear 2D-IR study of aniline-d_5. *J. Phys. Chem. B* **2013**, *117*, 15843–15855.

[12] Hamm, P.; Zanni, M. *Concepts and methods of 2D infrared spectroscopy*; Cambridge University Press, 2011.

[13] Wu, T.; Yang, L.; Zhang, R.; Shao, Q.; Zhuang, W. Modeling the thermal unfolding 2DIR spectra of a β-hairpin peptide based on the implicit solvent MD simulation. *J. Phys. Chem. A* **2013**, *117*, 6256–6263.

[14] Carr, J.; Buchanan, L.; Schmidt, J.; Zanni, M.; Skinner, J. Structure and dynamics of urea/water mixtures investigated by vibrational spectroscopy and molecular dynamics simulation. *J. Phys. Chem. B* **2013**, *117*, 13291–13300.

doi:10.6342/NTU202404353

[15] Gelin, M. F.; Egorova, D.; Domcke, W. Efficient method for the calculation of time- and frequency-resolved four-wave mixing signals and its application to photon-echo spectroscopy. *J. Chem. Phys.* **2005**, *123*, 164112.

[16] Wong, M. T.; Cheng, Y.-C. A quantum Langevin equation approach for two-dimensional electronic spectra of coupled vibrational and electronic dynamics. *J. Chem. Phys.* **2021**, *154*, 154107.

[17] Fournier, J. A.; Johnson, C. J.; Wolke, C. T.; Weddle, G. H.; Wolk, A. B.; Johnson, M. A. Vibrational spectral signature of the proton defect in the three-dimensional $H^+(H_2O)_{21}$ cluster. *Sci.* **2014**, *344*, 1009–1012.

[18] Lin, C.-K.; Huang, Q.-R.; Hayashi, M.; Kuo, J.-L. An ab initio anharmonic approach to IR, Raman and SFG spectra of the solvated methylammonium ion. *Phys. Chem. Chem. Phys* **2021**, *23*, 25736–25747.

[19] Fermi, E. Über den ramaneffekt des kohlendioxyds. *J. Phys.* **1931**, *71*, 250–259.

[20] Nydegger, M. W.; Rock, W.; Cheatum, C. M. 2D IR spectroscopy of the C–D stretching vibration of the deuterated formic acid dimer. *Phys. Chem. Chem. Phys* **2011**, *13*, 6098–6104.

[21] Olesen, S. G.; Gausco, T. L.; Weddle, G. H.; Hammerum, S.; Johnson, M. A. Vibrational predissociation spectra of the Ar-tagged [$CH_4 \cdot H_3O^+$] binary complex: spectroscopic signature of hydrogen bonding to an alkane. *Mol. Phys.* **2010**, *108*, 1191–1197.

[22] McCoy, A. B.; Guasco, T. L.; Leavitt, C. M.; Olesen, S. G.; Johnson, M. A. Vibrational manifestations of strong non-Condon effects in the $H_3O^+ \cdot X_3$ (X= Ar, N_2, CH_4,

doi:10.6342/NTU202404353

H_2O) complexes: A possible explanation for the intensity in the "association band" in the vibrational spectrum of water. *Phys. Chem. Chem. Phys* **2012**, *14*, 7205–7214.

[23] Tan, J. A.; Li, J.-W.; Chiu, C.-c.; Liao, H.-Y.; Huynh, H. T.; Kuo, J.-L. Tuning the vibrational coupling of H_3O^+ by changing its solvation environment. *Phys. Chem. Chem. Phys* **2016**, *18*, 30721–30732.

[24] Huang, Q.-R.; Nishigori, T.; Katada, M.; Fujii, A.; Kuo, J.-L. Fermi resonance in solvated H_3O^+: A counter-intuitive trend confirmed via a joint experimental and theoretical investigation. *Phys. Chem. Chem. Phys* **2018**, *20*, 13836–13844.

[25] Huang, Q.-R.; Li, Y.-C.; Nishigori, T.; Katada, M.; Fujii, A.; Kuo, J.-L. Vibrational coupling in solvated H_3O^+: Interplay between Fermi resonance and combination band. *J. Phys. Chem. Lett.* **2020**, *11*, 10067–10072.

[26] Weber, D. $CH_3NH_3PbX_3$, ein Pb(II)-system mit kubischer perowskitstruktur $CH_3NH_3PbX_3$, a Pb (II)-system with cubic perovskite structure. *Z. Naturforsch. B* **1978**, *33*, 1443–1445.

[27] Manser, J. S.; Christians, J. A.; Kamat, P. V. Intriguing optoelectronic properties of metal halide perovskites. *Chem. Rev.* **2016**, *116*, 12956–13008.

[28] Brenner, T. M.; Egger, D. A.; Kronik, L.; Hodes, G.; Cahen, D. Hybrid organic—inorganic perovskites: low-cost semiconductors with intriguing charge-transport properties. *Nat. Rev. Mater.* **2016**, *1*, 1–16.

[29] Glaser, T.; Müller, C.; Sendner, M.; Krekeler, C.; Semonin, O. E.; Hull, T. D.; Yaffe, O.; Owen, J. S.; Kowalsky, W.; Pucci, A., et al. Infrared spectroscopic study of vibrational modes in methylammonium lead halide perovskites. *J. Phys. Chem. Lett.* **2015**, *6*, 2913–2918.

doi:10.6342/NTU202404353

[30] Pérez-Osorio, M. A.; Milot, R. L.; Filip, M. R.; Patel, J. B.; Herz, L. M.; Johnston, M. B.; Giustino, F. Vibrational properties of the organic–inorganic halide perovskite $CH_3NH_3PbI_3$ from theory and experiment: factor group analysis, first-principles calculations, and low-temperature infrared spectra. *J. Phys. Chem. C* **2015**, *119*, 25703–25718.

[31] Schuck, G.; Többens, D. M.; Koch-Müller, M.; Efthimiopoulos, I.; Schorr, S. Infrared spectroscopic study of vibrational modes across the orthorhombic–tetragonal phase transition in methylammonium lead halide single crystals. *J. Phys. Chem. C* **2018**, *122*, 5227–5237.

[32] Bakulin, A. A.; Selig, O.; Bakker, H. J.; Rezus, Y. L.; Müller, C.; Glaser, T.; Lovrincic, R.; Sun, Z.; Chen, Z.; Walsh, A., et al. Real-time observation of organic cation reorientation in methylammonium lead iodide perovskites. *The journal of physical chemistry letters* **2015**, *6*, 3663–3669.

[33] Selig, O.; Sadhanala, A.; Muller, C.; Lovrincic, R.; Chen, Z.; Rezus, Y. L.; Frost, J. M.; Jansen, T. L.; Bakulin, A. A. Organic cation rotation and immobilization in pure and mixed methylammonium lead-halide perovskites. *J. Am. Chem. Soc.* **2017**, *139*, 4068–4074.

[34] Jackson, J. M.; Brucia, P. L.; Messina, M. An approach towards a simple quantum Langevin equation. *Chem. Phys. Lett.* **2011**, *511*, 471–481.

[35] Ford, G.; Kac, M. On the quantum Langevin equation. *J. Stat. Phys.* **1987**, *46*, 803–810.

[36] Ford, G. W.; Lewis, J. T.; O' Connell, R. Quantum langevin equation. *Phys. Rev. A* **1988**, *37*, 4419.

doi:10.6342/NTU202404353

[37] Edler, J.; Hamm, P. Two-dimensional vibrational spectroscopy of the amide I band of crystalline acetanilide: Fermi resonance, conformational substates, or vibrational self-trapping? *J. Chem. Phys.* **2003**, *119*, 2709–2715.

[38] De Marco, L.; Ramasesha, K.; Tokmakoff, A. Experimental evidence of Fermi resonances in isotopically dilute water from ultrafast broadband IR spectroscopy. *J. Phys. Chem. B* **2013**, *117*, 15319–15327.

[39] Rodgers, J. M.; Abaskharon, R. M.; Ding, B.; Chen, J.; Zhang, W.; Gai, F. Fermi resonance as a means to determine the hydrogen-bonding status of two infrared probes. *Phys. Chem. Chem. Phys* **2017**, *19*, 16144–16150.

[40] Costard, R.; Tyborski, T.; Fingerhut, B. P. Anharmonicities and coherent vibrational dynamics of phosphate ions in bulk H2 O. *Phys. Chem. Chem. Phys* **2015**, *17*, 29906–29917.

[41] Cheng, Y.-C.; Fleming, G. R. Coherence quantum beats in two-dimensional electronic spectroscopy. *J. Phys. Chem. A* **2008**, *112*, 4254–4260.

[42] Woutersen, S.; Mu, Y.; Stock, G.; Hamm, P. Subpicosecond conformational dynamics of small peptides probed by two-dimensional vibrational spectroscopy. *PNAS* **2001**, *98*, 11254–11258.

[43] Lindner, J.; Vöhringer, P.; Pshenichnikov, M. S.; Cringus, D.; Wiersma, D. A.; Mostovoy, M. Vibrational relaxation of pure liquid water. *Chem. Phys. Lett.* **2006**, *421*, 329–333.

[44] Dahms, F.; Costard, R.; Nibbering, E. T.; Elsaesser, T. Ultrafast vibrational energy flow in water monomers in acetonitrile. *Chem. Phys. Lett.* **2016**, *652*, 50–55.

doi:10.6342/NTU202404353

[45] Seifert, G.; Patzlaff, T.; Graener, H. Comprehensive investigation of vibrational relaxation of non-hydrogen-bonded water molecules in liquids. *J. Chem. Phys.* **2006**, *125*, 154506.

[46] Kwak, K.; Park, S.; Finkelstein, I. J.; Fayer, M. D. Frequency-frequency correlation functions and apodization in two-dimensional infrared vibrational echo spectroscopy: A new approach. *J. Chem. Phys.* **2007**, *127*.

[47] Light, J.; Hamilton, I.; Lill, J. Generalized discrete variable approximation in quantum mechanics. *J. Chem. Phys.* **1985**, *82*, 1400–1409.

[48] Carter, S.; Bowman, J. M.; Handy, N. C. Extensions and tests of "multimode": a code to obtain accurate vibration/rotation energies of many-mode molecules. *Theor. Chem. Acc.* **1998**, *100*, 191–198.

[49] Dickinson, A.; Certain, P. Calculation of matrix elements for one-dimensional quantum-mechanical problems. *J. Chem. Phys.* **1968**, *49*, 4209–4211.

doi:10.6342/NTU202404353

doi:10.6342/NTU202404353

Appendix A — The detailed description in constucting the effective Hamiltonian

In the appendix, we provide a brief description of the method for calculating the Hamiltonian of solvated hydroniums and methylammonium, which is established from Prof. Kuo's group.[24, 25] The molecules is optimized by MP2/aug-cc-pVDZ to obtain equilibrium structures and frequencies of each normal modes. Subsequently, we construct the potential energy suface (PES) and dipole moment surface (DMS) in each normal mode directions at CCSD/aug-ccpVTZ quality, which is based on Gauss-Hermite dicrete variable representation (DVR) method.[47] With the direct product of eigenvectors of vibraional modes as the basis sets, which is known as Finite Basis Representation (FBR), we transform the DVR Hamiltonian into FBR Hamiltonian. Finally, we calucate the spectral signals with the FBR Hamiltonian. In the following, we explain the detailed calculation setting in the solvated hydronium and methylammonium.

For the hydronium system, with a focus on the Fermi resonance occuring in O-H stretching region, we includes 5 degrees of freedom (DoF): 2 O-H bending modes and 3 O-H stretching modes. The PES and DMS were computed using DVR grids, each containing 7 grid points per mode. To reduce the computational cost, a mixed-level PES approach and n-mode representation (nMR) approach were utilized,[48] incorporating 1MR/

doi:10.6342/NTU202404353

2MR at the CCSD/aug-cc-pVTZ level. Then we use the 3MR/4MR at the MP2/aug-cc-pVDZ level, which has already demonstrated good agreement with experimentally observed spectra.[24, 25] Furthermore, the resulting DVR Hamiltonian was recast using the 39x39 (FBR) basis function described in the main text.

For the methylammonium system, with a focus on the Fermi resonance, we includes 10 degrees of freedom (DoF): 4 rocking modes, 3 bending modes and 3 N-H stretching modes. The PES and DMS were computed using DVR grids, each containing 9 grid points per mode. To reduce the computational cost, a mixed-level PES approach and n-mode representation (nMR) approach were utilized,[18] incorporating 1MR/2MR at the CCSD/aug-cc-pVTZ level. Then we use the 3MR/4MR at the MP2/aug-cc-pVDZ level, which has already demonstrated good agreement with experimentally observed spectra.,[18] Furthermore, the resulting DVR Hamiltonian was recast using the 2485x2485 (FBR) basis function described in the main text.

To calculate the spectral in a reasonable computational cost, we employ an approach by truncating the eigenbasis of our effective Hamiltonian of solvated methylammonium systems. Initially, we presume that the system remains in the ground state before interacting with the lasers. Consequently, we select eigenstates with a sufficiently strong transition dipole moment with respect to the ground state. Subsequently,we apply the same procedure to choose the remaining eigenstates, considering the transitions from the previously selected eigenstates, Finally, we set the threshold of the magnitudes of transition dipole moments at one-tenth. The sizes of truncated Hamiltonians are around 300x300 in these solvated methylammonium systems.

In the DVR basis, dipole moment operators are expressed on the diagonal elements

doi:10.6342/NTU202404353

with the dipole moment for each geometry, and can be transformed to the FBR basis straightforwardly. Similarly, for position and momentum operators, we can write down their expressions for each vibration mode in the FBR basis using similar steps. These operators can be easily evaluated in the harmonic oscillator basis, which is precisely the weighted spectral basis in GH-DVR:

$$
\begin{aligned}
x_{mn} &= \langle m|\hat{x}|n\rangle = \sqrt{\frac{\hbar}{2m\omega}}(\sqrt{n+1}\delta_{m,n+1} + \sqrt{n}\delta_{m_n-1}) \\
p_{mn} &= \langle m|\hat{p}|n\rangle = i\sqrt{\frac{m\omega\hbar}{2}}(\sqrt{n+1}\delta_{m,n+1} - \sqrt{n}\delta_{m_n-1})
\end{aligned}
\tag{A.1}
$$

In this case, we can directly obtain the matrix element in position basis by diagonalizing position operators,[49] which is precisely the transform matrix between the harmonic oscillator basis and DVR position basis. Thus, we can transform these operators to the position basis and recast them into the 39x39 FBR basis.

doi:10.6342/NTU202404353

doi:10.6342/NTU202404353

Appendix B — Matrices of effective Hamiltonians and dipole opertators

B.1 Ar-tagged Hydronium cluster

B.1.1 Effective Hamiltonian

doi:10.6342/NTU202404353

Table B.1: The effective Hamiltonian in the unit of wavenumber, where $|b_x, s_y\rangle$ indicates x and y vibrational quanta in bending and stretching modes, respectively.

	$\|0,0\rangle$	$\|1,0\rangle$		$\|0,1\rangle$			$\|2,0\rangle$			$\|0,2\rangle$						$\|2,1\rangle$								
$\|0,0\rangle$	2.5	0.0	-0.2	37.1	7.6	4.0	-54.5	0.0	0.0	41.1	30.4	12.2	7.7	0.1	-0.5	35.1	-6.4	5.0	7.2	37.8	-7.8	3.8	-9.1	-34.8
$\|1,0\rangle$	0.0	1660.9	0.0	1.0	-5.8	1.4	0.0	4.2	0.1	7.5	-11.3	4.7	-0.6	-8.9	18.4	2.4	-12.8	-1.1	-13.4	-3.6	5.9	3.4	-8.1	-0.8
	-0.2	0.0	1660.9	-0.1	-1.6	-5.7	-0.4	0.0	-4.8	5.2	-1.3	-13.8	-1.1	17.4	9.5	0.2	1.0	11.7	-3.5	-6.8	1.3	-13.1	0.9	-4.7
$\|0,1\rangle$	37.1	1.0	-0.1	3292.0	2.5	1.3	35.1	-6.4	5.0	-20.4	-9.5	-3.1	46.7	1.0	-1.6	-78.1	3.1	-3.0	2.3	-9.7	3.8	1.2	0.5	7.5
	7.6	-5.8	-1.6	2.5	3297.0	0.2	7.2	37.8	-7.8	10.7	-22.6	1.0	7.5	-5.2	24.2	2.3	-9.7	3.8	-88.9	0.0	-11.5	0.1	13.0	7.5
	4.0	1.4	-5.7	1.3	0.2	3297.7	3.8	-9.1	-34.8	3.6	1.2	-25.6	3.2	22.7	5.7	1.2	0.5	7.5	0.1	13.0	7.5	-89.2	-3.1	14.5
$\|2,0\rangle$	-54.5	0.0	-0.4	35.1	7.2	3.8	3304.3	-0.1	-0.1	39.3	29.2	11.7	7.3	0.2	-0.5	106.4	-12.2	9.3	21.8	72.1	-15.0	11.7	-17.4	-66.6
	0.0	4.2	0.0	-6.4	37.8	-9.1	-0.1	3317.1	0.0	-16.3	26.1	-10.3	-0.3	-4.5	6.0	-12.2	104.8	0.7	72.1	22.2	-3.8	-17.4	15.2	0.6
	0.0	0.1	-4.8	5.0	-7.8	-34.8	-0.1	0.0	3317.4	11.1	-3.2	-29.8	0.5	-5.9	-2.5	9.3	0.7	105.8	-15.0	-3.8	21.1	-66.6	0.6	7.6
$\|0,2\rangle$	41.1	7.5	5.2	-20.4	10.7	3.6	39.3	-16.3	11.1	6378.9	0.4	0.1	-8.8	-0.1	2.6	-19.1	20.8	-12.3	10.0	-26.9	10.6	3.3	-1.5	9.8
	30.4	-11.3	-1.3	-9.5	-22.6	1.2	29.2	26.1	-3.2	0.4	6392.5	0.0	-6.2	1.1	-4.6	-8.9	-21.7	2.8	-21.2	-13.4	-10.7	1.2	15.5	18.2
	12.2	4.7	-13.8	-3.1	1.0	-25.6	11.7	-10.3	-29.8	0.1	0.0	6398.1	-2.3	-5.2	-1.1	-2.9	4.4	19.1	1.0	10.9	12.8	-23.9	-9.4	23.7
	7.7	-0.6	-1.1	46.7	7.5	3.2	7.3	-0.3	0.5	-8.8	-6.2	-2.3	6600.1	0.6	1.1	44.2	3.4	-1.4	7.1	-23.5	5.4	3.1	3.5	17.0
	0.1	-8.9	17.4	1.0	-5.2	22.7	0.2	-4.5	-5.9	-0.1	1.1	-5.2	0.6	6596.7	0.0	1.1	-18.0	-25.7	-5.0	26.5	13.8	21.5	-20.8	23.7
	-0.5	18.4	9.5	-1.6	24.2	5.7	-0.5	6.0	-2.5	2.6	-4.6	-1.1	1.1	0.0	6606.6	-1.6	15.7	-6.9	23.0	21.1	-26.4	5.4	30.9	17.5
$\|2,1\rangle$	35.1	2.4	0.2	-78.1	2.3	1.2	106.4	-12.2	9.3	-19.1	-8.9	-2.9	44.2	1.1	-1.6	6546.9	7.3	-6.8	7.0	-22.3	7.8	3.7	2.2	18.5
	-6.4	-12.8	1.0	3.1	-9.7	0.5	-12.2	104.8	0.7	20.8	-21.7	4.4	3.4	-18.0	15.7	7.3	6559.3	0.0	-22.3	6.9	0.2	2.2	3.5	0.0
	5.0	-1.1	11.7	-3.0	3.8	7.5	9.3	0.7	105.8	-12.3	2.8	19.1	-1.4	-25.7	-6.9	-6.8	0.0	6559.7	7.8	0.2	7.3	18.5	0.0	4.0
	7.2	-13.4	-3.5	2.3	-88.9	0.1	21.8	72.1	-15.0	10.0	-21.2	1.0	7.1	-5.0	23.0	7.0	-22.3	7.8	6531.2	-2.1	-20.7	0.4	23.6	14.9
	37.8	-3.6	-6.8	-9.7	0.0	13.0	72.1	22.2	-3.8	-26.9	-13.4	10.9	-23.5	26.5	21.1	-22.3	6.9	0.2	-2.1	6543.2	0.0	23.6	0.2	-0.2
	-7.8	5.9	1.3	3.8	-11.5	7.5	-15.0	-3.8	21.1	10.6	-10.7	12.8	5.4	13.8	-26.4	7.8	0.2	7.3	-20.7	0.0	6543.1	14.9	-0.2	0.7
	3.8	3.4	-13.1	1.2	0.1	-89.2	11.7	-17.4	-66.6	3.3	1.2	-23.9	3.1	21.5	5.4	3.7	2.2	18.5	0.4	23.6	14.9	6531.2	-5.2	27.2
	-9.1	-8.1	0.9	0.5	13.0	-3.1	-17.4	15.2	0.6	-1.5	15.5	-9.4	3.5	-20.8	30.9	2.2	3.5	0.0	23.6	0.2	-0.2	-5.2	6542.7	0.0
	-34.8	-0.8	-4.7	7.5	7.5	14.5	-66.6	0.6	7.6	9.8	18.2	23.7	17.0	23.7	17.5	18.5	0.0	4.0	14.9	-0.2	0.7	27.2	0.0	6543.8

doi:10.6342/NTU202404353

B.2 N_2-tagged Hydronium cluster

B.2.1 Effective Hamiltonian

doi:10.6342/NTU202404353

Table B.2: The effective Hamiltonian in the unit of wavenumber, where $|b_x, s_y\rangle$ indicates x and y vibrational quanta in bending and stretching modes, respectively.

	$\|0,0\rangle$	$\|1,0\rangle$		$\|0,1\rangle$			$\|2,0\rangle$			$\|0,2\rangle$						$\|2,1\rangle$								
$\|0,0\rangle$	2.0	0.0	0.0	-4.0	0.0	-33.0	-55.0	0.0	0.0	-45.0	-23.0	0.0	0.0	-1.0	0.0	-3.0	0.0	36.0	0.0	-39.0	0.0	-32.0	0.0	-4.0
$\|1,0\rangle$	0.0	1691.0	0.0	0.0	3.0	0.0	0.0	4.0	0.0	-1.0	3.0	-28.0	-19.0	2.0	0.0	-1.0	5.0	0.0	10.0	0.0	-3.0	0.0	11.0	1.0
	0.0	0.0	1691.0	3.0	0.0	0.0	0.0	0.0	-4.0	13.0	-24.0	-3.0	-2.0	-20.0	2.0	9.0	1.0	2.0	1.0	4.0	0.0	0.0	1.0	-9.0
$\|0,1\rangle$	-4.0	0.0	3.0	3118.0	0.0	1.0	-3.0	0.0	36.0	-9.0	14.0	0.0	0.0	25.0	4.0	-89.0	0.0	13.0	0.0	15.0	0.0	1.0	0.0	6.0
	0.0	3.0	0.0	0.0	3121.0	0.0	0.0	-39.0	0.0	0.0	0.0	18.0	24.0	0.0	0.0	0.0	15.0	0.0	-89.0	0.0	-12.0	0.0	-10.0	0.0
	-33.0	0.0	0.0	1.0	0.0	3172.0	-32.0	0.0	-4.0	-7.0	-6.0	0.0	0.0	0.0	46.0	1.0	0.0	6.0	0.0	-10.0	0.0	-77.0	0.0	-2.0
$\|2,0\rangle$	-55.0	0.0	0.0	-3.0	0.0	-32.0	3365.0	0.0	0.0	-43.0	-22.0	0.0	0.0	-1.0	1.0	-10.0	0.0	68.0	0.0	-73.0	0.0	-95.0	0.0	-8.0
	0.0	4.0	0.0	0.0	-39.0	0.0	0.0	3376.0	0.0	0.0	0.0	35.0	-7.0	0.0	0.0	0.0	-14.0	0.0	-73.0	0.0	4.0	0.0	-94.0	0.0
	0.0	0.0	-4.0	36.0	0.0	-4.0	0.0	0.0	3377.0	14.0	-27.0	0.0	0.0	3.0	0.0	68.0	0.0	-6.0	0.0	4.0	0.0	-8.0	0.0	-95.0
$\|0,2\rangle$	-45.0	-1.0	13.0	-9.0	0.0	-7.0	-43.0	0.0	14.0	5991.0	-1.0	0.0	0.0	-3.0	-8.0	-8.0	0.0	34.0	0.0	-16.0	0.0	-7.0	0.0	7.0
	-23.0	3.0	-24.0	14.0	0.0	-6.0	-22.0	0.0	-27.0	-1.0	6012.0	0.0	0.0	5.0	-5.0	13.0	0.0	-9.0	0.0	-27.0	0.0	-6.0	0.0	-18.0
	0.0	-28.0	-3.0	0.0	18.0	0.0	0.0	35.0	0.0	0.0	0.0	6021.0	6.0	0.0	0.0	0.0	-15.0	0.0	16.0	0.0	21.0	0.0	19.0	0.0
	0.0	-19.0	-2.0	0.0	24.0	0.0	0.0	-7.0	0.0	0.0	0.0	6.0	6275.0	0.0	0.0	0.0	42.0	0.0	22.0	0.0	-29.0	0.0	31.0	0.0
	-1.0	2.0	-20.0	25.0	0.0	0.0	-1.0	0.0	3.0	-3.0	5.0	0.0	0.0	6289.0	1.0	23.0	0.0	27.0	0.0	35.0	0.0	0.0	0.0	-29.0
	0.0	0.0	2.0	4.0	0.0	46.0	1.0	0.0	0.0	-8.0	-5.0	0.0	0.0	1.0	6345.0	4.0	0.0	14.0	0.0	-18.0	0.0	43.0	0.0	0.0
$\|2,1\rangle$	-3.0	-1.0	9.0	-89.0	0.0	1.0	-10.0	0.0	68.0	-8.0	13.0	0.0	0.0	23.0	4.0	6413.0	0.0	28.0	0.0	30.0	0.0	4.0	0.0	18.0
	0.0	5.0	1.0	0.0	15.0	0.0	0.0	-14.0	0.0	0.0	0.0	-15.0	42.0	0.0	0.0	0.0	6423.0	0.0	30.0	0.0	0.0	0.0	4.0	0.0
	36.0	0.0	2.0	13.0	0.0	6.0	68.0	0.0	-6.0	34.0	-9.0	0.0	0.0	27.0	14.0	28.0	0.0	6424.0	0.0	0.0	0.0	18.0	0.0	4.0
	0.0	10.0	1.0	0.0	-89.0	0.0	0.0	-73.0	0.0	0.0	0.0	16.0	22.0	0.0	0.0	0.0	30.0	0.0	6416.0	0.0	-23.0	0.0	-25.0	0.0
	-39.0	0.0	4.0	15.0	0.0	-10.0	-73.0	0.0	4.0	-16.0	-27.0	0.0	0.0	35.0	-18.0	30.0	0.0	0.0	0.0	6427.0	0.0	-25.0	0.0	0.0
	0.0	-3.0	0.0	0.0	-12.0	0.0	0.0	4.0	0.0	0.0	0.0	21.0	-29.0	0.0	0.0	0.0	0.0	0.0	-23.0	0.0	6427.0	0.0	0.0	0.0
	-32.0	0.0	0.0	1.0	0.0	-77.0	-95.0	0.0	-8.0	-7.0	-6.0	0.0	0.0	0.0	43.0	4.0	0.0	18.0	0.0	-25.0	0.0	6491.0	0.0	-5.0
	0.0	11.0	1.0	0.0	-10.0	0.0	0.0	-94.0	0.0	0.0	0.0	19.0	31.0	0.0	0.0	0.0	4.0	0.0	-25.0	0.0	0.0	0.0	6502.0	0.0
	-4.0	1.0	-9.0	6.0	0.0	-2.0	-8.0	0.0	-95.0	7.0	-18.0	0.0	0.0	-29.0	0.0	18.0	0.0	4.0	0.0	0.0	0.0	-5.0	0.0	6503.0

doi:10.6342/NTU202404353

B.3 (HBr_3)-tagged methylammonium cluster

B.3.1 Effective Hamiltonian

doi:10.6342/NTU202404353

Table B.3: The effective Hamiltonian in the unit of wavenumber, where $|r'_x, r_y, b_z, s_q\rangle$ indicates x and y, z and q vibrational quanta in rocking R'and R, bending and stretching modes, respectively.

	$\|0,0,0,0\rangle$	$\|1,0,0,0\rangle$		$\|0,1,0,0\rangle$		$\|0,0,1,0\rangle$		
$\|0,0,0,0\rangle$	29.0	2.5	-1.3	3.8	-1.0	-22.5	-1.0	0.0
$\|1,0,0,0\rangle$	2.5	1013.7	0.3	-5.2	-4.1	-0.7	24.4	18.4
	-1.3	0.3	1013.1	3.7	-5.5	-0.3	18.9	-23.6
$\|0,1,0,0\rangle$	3.8	-5.2	3.7	1352.9	0.7	-0.8	-6.8	-22.9
	-1.0	-4.1	-5.5	0.7	1353.1	0.2	-22.3	7.1
$\|0,0,1,0\rangle$	-22.5	-0.7	-0.3	-0.8	0.2	1563.6	0.1	-0.1
	-1.0	24.4	18.9	-6.8	-22.3	0.1	1674.5	-0.2
	0.0	18.4	-23.6	-22.9	7.1	-0.1	-0.2	1676.0

doi:10.6342/NTU202404353

Table B.4: The effective Hamiltonian in the unit of wavenumber, where $|r'_x, r_y, b_z, s_q\rangle$ indicates x and y, z and q vibrational quanta in rocking R'and R, bending and stretching modes, respectively.

	$\|1,0,1,0\rangle$						$\|0,1,1,0\rangle$					$\|0,0,2,0\rangle$	$\|0,0,0,1\rangle$			$\|0,0,2,0\rangle$				
$\|1,0,1,0\rangle$	2561.0	0.2	6.0	0.1	-0.3	5.6	1.8	0.0	3.4	0.5	0.1	-3.6	2.1	-12.6	-22.4	-65.6	25.9	0.9	-0.2	-0.5
	0.2	2560.4	0.1	-6.0	5.6	-0.3	0.5	-3.0	-0.5	3.5	3.5	0.6	2.9	-29.5	-58.4	24.9	12.7	-9.9	0.2	-0.4
	6.0	0.1	2661.9	-0.3	-0.7	0.1	-2.6	-1.9	-7.8	-1.0	-0.2	0.0	-0.4	-5.8	-13.2	-36.7	1.8	1.5	-35.5	-16.9
	0.1	-6.0	-0.3	2661.6	0.1	0.3	-2.0	2.8	-0.9	6.2	0.1	0.0	0.0	16.2	33.7	-15.2	1.1	16.3	-17.0	25.4
	-0.3	5.6	-0.7	0.1	2663.4	1.0	2.2	-2.7	-0.2	0.0	-7.7	-1.3	0.0	-17.2	-32.5	14.8	0.6	-10.7	-7.5	-24.3
	5.6	-0.3	0.1	0.3	1.0	2662.8	-2.6	-2.4	0.1	0.0	-0.7	6.5	0.5	-8.2	-12.2	-37.1	0.6	2.4	13.6	-17.4
$\|0,1,1,0\rangle$	1.8	0.5	-2.6	-2.0	2.2	-2.6	2892.6	0.8	2.6	0.7	0.5	-2.8	1.8	-12.0	-22.2	-45.9	-22.7	0.0	-0.2	-0.7
	0.0	-3.0	-1.9	2.8	-2.7	-2.4	0.8	2892.6	0.7	-2.6	-2.8	-1.0	-3.9	20.5	41.1	-24.8	7.0	6.4	-0.4	0.5
	3.4	-0.5	-7.8	-0.9	-0.2	0.1	2.6	0.7	2999.3	-0.1	-0.3	0.0	-0.5	-5.2	-5.9	-30.8	1.3	-0.1	29.6	5.9
	0.5	3.5	-1.0	6.2	0.0	0.0	0.7	-2.6	-0.1	2999.1	0.9	-0.1	0.1	0.3	-0.9	-9.9	30.6	-0.9	-9.7	21.5
	0.1	3.5	-0.2	0.1	-7.7	-0.7	0.5	-2.8	-0.3	0.9	2999.3	0.1	-0.1	0.5	-3.8	30.8	9.6	0.6	1.8	21.3
$\|0,0,2,0\rangle$	-3.6	0.6	0.0	0.0	-1.3	6.5	-2.8	-1.0	0.0	-0.1	0.1	3000.5	1.0	0.5	-0.4	-30.6	-9.3	-0.1	11.3	-10.4
$\|0,0,0,1\rangle$	2.1	2.9	-0.4	0.0	0.0	0.5	1.8	-3.9	-0.5	0.1	-0.1	1.0	3000.7	-0.3	-2.1	-10.0	30.4	-0.2	0.5	0.0
	-12.6	-29.5	-5.8	16.2	-17.2	-8.2	-12.0	20.5	-5.2	0.3	0.5	0.5	-0.3	3097.0	40.6	1.4	3.0	-0.2	17.3	7.2
	-22.4	-58.4	-13.2	33.7	-32.5	-12.2	-22.2	41.1	-5.9	-0.9	-3.8	-0.4	-2.1	40.6	3106.7	0.2	0.5	-0.6	-12.1	16.8
$\|0,0,2,0\rangle$	-65.6	24.9	-36.7	-15.2	14.8	-37.1	-45.9	-24.8	-30.8	-9.9	30.8	-30.6	-10.0	1.4	0.2	3144.9	0.1	-2.8	7.4	6.1
	25.9	12.7	1.8	1.1	0.6	0.6	-22.7	7.0	1.3	30.6	9.6	-9.3	30.4	3.0	0.5	0.1	3147.2	10.9	0.0	0.3
	0.9	-9.9	1.5	16.3	-10.7	2.4	0.0	6.4	-0.1	-0.9	0.6	-0.1	-0.2	-0.2	-0.6	-2.8	10.9	3355.5	0.0	0.1
	-0.2	0.2	-35.5	-17.0	-7.5	13.6	-0.2	-0.4	29.6	-9.7	1.8	11.3	0.5	17.3	-12.1	7.4	0.0	0.0	3308.4	1.9
	-0.5	-0.4	-16.9	25.4	-24.3	-17.4	-0.7	0.5	5.9	21.5	21.3	-10.4	0.0	7.2	16.8	6.1	0.3	0.1	1.9	3315.1

doi:10.6342/NTU202404353

B.4 (HCl_3)-tagged methylammonium cluster

B.4.1 Effective Hamiltonian

doi:10.6342/NTU202404353

Table B.5: The effective Hamiltonian in the unit of wavenumber, where $|r'_x, r_y, b_z, s_q\rangle$ indicates x and y, z and q vibrational quanta in rocking R'and R, bending and stretching modes, respectively.

	$\|0,0,0,0\rangle$	$\|1,0,0,0\rangle$		$\|0,1,0,0\rangle$		$\|0,0,1,0\rangle$		
$\|0,0,0,0\rangle$	30.6	-0.5	-0.4	1.7	-0.8	-20.2	-0.1	0.6
$\|1,0,0,0\rangle$	-0.5	1004.5	-0.3	-6.8	-8.0	-0.3	-29.3	0.8
	-0.4	-0.3	1004.0	7.9	-6.9	-0.1	0.6	29.3
$\|0,1,0,0\rangle$	1.7	-6.8	7.9	1347.5	0.5	-0.3	17.3	15.6
	-0.8	-8.0	-6.9	0.5	1346.3	-0.1	15.6	-17.2
$\|0,0,1,0\rangle$	-20.2	-0.3	-0.1	-0.3	-0.1	1566.5	0.1	-0.1
	-0.1	-29.3	0.6	17.3	15.6	0.1	1673.1	-0.2
	0.6	0.8	29.3	15.6	-17.2	-0.1	-0.2	1675.4

doi:10.6342/NTU202404353

Table B.6: The effective Hamiltonian in the unit of wavenumber, where $|r'_x, r_y, b_z, s_q\rangle$ indicates x and y, z and q vibrational quanta in rocking R'and R, bending and stretching modes, respectively.

	$\|1,0,1,0\rangle$						$\|0,1,1,0\rangle$					$\|0,0,2,0\rangle$	$\|0,0,0,1\rangle$			$\|0,0,2,0\rangle$				
$\|1,0,1,0\rangle$	2555.2	-0.3	6.0	0.1	-0.3	5.6	1.8	0.0	3.4	0.5	0.1	-3.6	2.1	-12.6	-22.4	-65.6	25.9	0.9	-0.2	-0.5
	-0.3	2554.6	0.1	-6.0	5.6	-0.3	0.5	-3.0	-0.5	3.5	3.5	0.6	2.9	-29.5	-58.4	24.9	12.7	-9.9	0.2	-0.4
	6.0	0.1	2649.2	-0.5	-0.2	0.6	2.6	-2.3	-7.8	-1.0	-0.2	0.0	-0.4	-5.8	-13.2	-36.7	1.8	1.5	-35.5	-16.9
	0.1	-6.0	-0.5	2649.7	0.6	-0.2	-2.5	-2.5	-0.9	6.2	0.1	0.0	0.0	16.2	33.7	-15.2	1.1	16.3	-17.0	25.4
	-0.3	5.6	-0.2	0.6	2652.7	-0.1	2.0	2.7	-0.2	0.0	-7.7	-1.3	0.0	-17.2	-32.5	14.8	0.6	-10.7	-7.5	-24.3
	5.6	-0.3	0.6	-0.2	-0.1	2651.2	3.0	-2.2	0.1	0.0	-0.7	6.5	0.5	-8.2	-12.2	-37.1	0.6	2.4	13.6	-17.4
$\|0,1,1,0\rangle$	1.8	0.5	2.6	-2.5	2.0	3.0	2889.9	0.5	2.6	0.7	0.5	-2.8	1.8	-12.0	-22.2	-45.9	-22.7	0.0	-0.2	-0.7
	0.0	-3.0	-2.3	-2.5	2.7	-2.2	0.5	2888.7	0.7	-2.6	-2.8	-1.0	-3.9	20.5	41.1	-24.8	7.0	6.4	-0.4	0.5
	3.4	-0.5	-7.8	-0.9	-0.2	0.1	2.6	0.7	2990.7	0.5	-0.3	0.0	0.4	-0.7	32.5	-4.0	-0.3	-0.1	29.6	5.9
	0.5	3.5	-1.0	6.2	0.0	0.0	0.7	-2.6	0.5	2989.3	0.0	-0.2	0.2	3.5	4.5	31.9	0.0	-0.9	-9.7	21.5
	0.1	3.5	-0.2	0.1	-7.7	-0.7	0.5	-2.8	-0.3	0.0	2993.1	0.5	0.2	1.3	-4.0	-31.8	-0.2	0.6	1.8	21.3
$\|0,0,2,0\rangle$	-3.6	0.6	0.0	0.0	-1.3	6.5	-2.8	-1.0	0.0	-0.2	0.5	2992.0	-0.4	-2.1	32.4	-4.0	0.0	-0.1	11.3	-10.4
$\|0,0,0,1\rangle$	2.1	2.9	-0.4	0.0	0.0	0.5	1.8	-3.9	0.4	0.2	0.2	-0.4	3109.6	-42.9	-1.6	1.8	0.2	-0.2	0.5	0.0
	-12.6	-29.5	-5.8	16.2	-17.2	-8.2	-12.0	20.5	-0.7	3.5	1.3	-2.1	-42.9	3142.0	0.2	-0.2	-0.7	-0.2	17.3	7.2
	-22.4	-58.4	-13.2	33.7	-32.5	-12.2	-22.2	41.1	32.5	4.5	-4.0	32.4	-1.6	0.2	3181.9	0.2	10.1	-0.6	-12.1	16.8
$\|0,0,2,0\rangle$	-65.6	24.9	-36.7	-15.2	14.8	-37.1	-45.9	-24.8	-4.0	31.9	-31.8	-4.0	1.8	-0.2	0.2	3183.5	-6.1	-2.8	7.4	6.1
	25.9	12.7	1.8	1.1	0.6	0.6	-22.7	7.0	-0.3	0.0	-0.2	0.0	0.2	-0.7	10.1	-6.1	3204.8	10.9	0.0	0.3
	0.9	-9.9	1.5	16.3	-10.7	2.4	0.0	6.4	-0.1	-0.9	0.6	-0.1	-0.2	-0.2	-0.6	-2.8	10.9	3340.8	0.0	0.1
	-0.2	0.2	-35.5	-17.0	-7.5	13.6	-0.2	-0.4	29.6	-9.7	1.8	11.3	0.5	17.3	-12.1	7.4	0.0	0.0	3312.6	0.1
	-0.5	-0.4	-16.9	25.4	-24.3	-17.4	-0.7	0.5	5.9	21.5	21.3	-10.4	0.0	7.2	16.8	6.1	0.3	0.1	0.1	3314.7

doi:10.6342/NTU202404353

B.5 $(HBr_1)(HCl_2)$-tagged methylammonium cluster

B.5.1 Effective Hamiltonian

doi:10.6342/NTU202404353

Table B.7: The effective Hamiltonian in the unit of wavenumber, where $|r'_x, r_y, b_z, s_q\rangle$ indicates x and y, z and q vibrational quanta in rocking R'and R, bending and stretching modes, respectively.

	$\|0,0,0,0\rangle$	$\|1,0,0,0\rangle$		$\|0,1,0,0\rangle$		$\|0,0,1,0\rangle$		
$\|0,0,0,0\rangle$	30.1	-1.8	0.2	0.7	-1.6	22.5	-2.2	0.2
$\|1,0,0,0\rangle$	-1.8	1008.1	0.0	-10.2	-1.5	1.1	26.7	14.3
	0.2	0.0	1012.2	-1.0	8.8	1.8	12.3	-26.2
$\|0,1,0,0\rangle$	0.7	-10.2	-1.0	1352.0	0.0	1.3	-22.8	-4.5
	-1.6	-1.5	8.8	0.0	1353.0	-2.5	7.0	-22.7
$\|0,0,1,0\rangle$	22.5	1.1	1.8	1.3	-2.5	1569.4	0.0	-0.2
	-2.2	26.7	12.3	-22.8	7.0	0.0	1676.1	-0.3
	0.2	14.3	-26.2	-4.5	-22.7	-0.2	-0.3	1678.3

doi:10.6342/NTU202404353

Table B.8: The effective Hamiltonian in the unit of wavenumber, where $|r'_x, r_y, b_z, s_q\rangle$ indicates x and y, z and q vibrational quanta in rocking R'and R, bending and stretching modes, respectively.

	$\|1,0,1,0\rangle$						$\|0,1,1,0\rangle$					$\|0,0,2,0\rangle$	$\|0,0,0,1\rangle$			$\|0,0,2,0\rangle$				
$\|1,0,1,0\rangle$	2562.1	0.0	6.0	0.1	-0.3	5.6	1.8	0.0	3.4	0.5	0.1	-3.6	2.1	-12.6	-22.4	-65.6	25.9	0.9	-0.2	-0.5
	0.0	2566.1	0.1	-6.0	5.6	-0.3	0.5	-3.0	-0.5	3.5	3.5	0.6	2.9	-29.5	-58.4	24.9	12.7	-9.9	0.2	-0.4
	6.0	0.1	2657.3	-0.6	-1.0	0.3	3.4	0.5	-7.8	-1.0	-0.2	0.0	-0.4	-5.8	-13.2	-36.7	1.8	1.5	-35.5	-16.9
	0.1	-6.0	-0.6	2661.8	0.3	0.3	-0.5	3.5	-0.9	6.2	0.1	0.0	0.0	16.2	33.7	-15.2	1.1	16.3	-17.0	25.4
	-0.3	5.6	-1.0	0.3	2660.0	0.4	0.1	-3.6	-0.2	0.0	-7.7	-1.3	0.0	-17.2	-32.5	14.8	0.6	-10.7	-7.5	-24.3
	5.6	-0.3	0.3	0.3	0.4	2663.5	3.5	0.6	0.1	0.0	-0.7	6.5	0.5	-8.2	-12.2	-37.1	0.6	2.4	13.6	-17.4
$\|0,1,1,0\rangle$	1.8	0.5	3.4	-0.5	0.1	3.5	2898.2	0.0	2.6	0.7	0.5	-2.8	1.8	-12.0	-22.2	-45.9	-22.7	0.0	-0.2	-0.7
	0.0	-3.0	0.5	3.5	-3.6	0.6	0.0	2899.1	0.7	-2.6	-2.8	-1.0	-3.9	20.5	41.1	-24.8	7.0	6.4	-0.4	0.5
	3.4	-0.5	-7.8	-0.9	-0.2	0.1	2.6	0.7	2999.3	-0.1	-0.3	0.0	-0.5	-5.2	-5.9	-30.8	1.3	-0.1	29.6	5.9
	0.5	3.5	-1.0	6.2	0.0	0.0	0.7	-2.6	-0.1	3000.4	0.0	-0.2	0.0	-12.7	-28.9	8.3	-2.3	-3.4	-9.7	21.5
	0.1	3.5	-0.2	0.1	-7.7	-0.7	0.5	-2.8	-0.3	0.0	3001.7	0.0	0.0	-15.7	-27.1	8.1	0.1	0.5	1.8	21.3
$\|0,0,2,0\rangle$	-3.6	0.6	0.0	0.0	-1.3	6.5	-2.8	-1.0	0.0	-0.2	0.0	3002.7	-0.5	2.5	7.8	31.8	0.1	-0.1	11.3	-10.4
$\|0,0,0,1\rangle$	2.1	2.9	-0.4	0.0	0.0	0.5	1.8	-3.9	-0.5	0.0	0.0	-0.5	3106.8	-36.8	20.6	-0.1	-0.1	0.0	0.5	0.0
	-12.6	-29.5	-5.8	16.2	-17.2	-8.2	-12.0	20.5	-5.2	-12.7	-15.7	2.5	-36.8	3114.5	-4.5	0.0	3.2	-0.8	17.3	7.2
	-22.4	-58.4	-13.2	33.7	-32.5	-12.2	-22.2	41.1	-5.9	-28.9	-27.1	7.8	20.6	-4.5	3169.5	-0.2	6.0	-1.6	-12.1	16.8
$\|0,0,2,0\rangle$	-65.6	24.9	-36.7	-15.2	14.8	-37.1	-45.9	-24.8	-30.8	8.3	8.1	31.8	-0.1	0.0	-0.2	3191.3	8.9	0.9	7.4	6.1
	25.9	12.7	1.8	1.1	0.6	0.6	-22.7	7.0	1.3	-2.3	0.1	0.1	-0.1	3.2	6.0	8.9	3211.0	0.0	0.0	0.3
	0.9	-9.9	1.5	16.3	-10.7	2.4	0.0	6.4	-0.1	-3.4	0.5	-0.1	0.0	-0.8	-1.6	0.9	0.0	3358.3	0.0	-0.1
	-0.2	0.2	-35.5	-17.0	-7.5	13.6	-0.2	-0.4	29.6	-9.7	1.8	11.3	0.5	17.3	-12.1	7.4	0.0	0.0	3313.6	-0.2
	-0.5	-0.4	-16.9	25.4	-24.3	-17.4	-0.7	0.5	5.9	21.5	21.3	-10.4	0.0	7.2	16.8	6.1	0.3	-0.1	-0.2	3321.6

doi:10.6342/NTU202404353

doi:10.6342/NTU202404353

Appendix C — Time-dependent perturbation theory

Time-dependent perturbation theory is a framework capable of addressing time-dependent perturbations $V(t)$ applied to a time-independent Hamiltonian H_0. In our context, $V(t)$ represents a light-matter interaction that contributes to the spectroscopic signals we seek. Initially, we present the time-dependent Schrödinger equation with an exact wavefunction denoted by $|\psi(t)\rangle$.

$$i\hbar\frac{\partial}{\partial t}|\psi(t)\rangle = [H_0 + V(t))]|\psi(t)\rangle \tag{B.2}$$

Hence, we expand this exact wavefunction $|\psi(t)\rangle$ to

$$|\psi(t)\rangle = \left|\psi^0(t)\right\rangle + \left|\psi^{(1)}(t)\right\rangle + \left|\psi^{(2)}(t)\right\rangle + \cdots \tag{B.3}$$

The subsequent question addresses how to manage the first order, as well as other orders, of the wavefunction. First, we focus on the evolution of $|\psi(t)\rangle$. The wavefunction $|\psi(t)\rangle$ can be considered by acted by a time-evolution operator $U(t, t_0)$, allowing it to evolve from t_0 to t.

$$|\psi(t)\rangle = U(t, t_0)\,|\psi(t_0)\rangle \tag{B.4}$$

doi:10.6342/NTU202404353

The operator $U(t,t_0)$ can be resolved by incorporating it into TDSE, as illustrated below.

$$\begin{aligned} U(t,t_0) &= I + (-\frac{i}{\hbar})\int_{t_0}^{t} H(\tau_1)d\tau_1 + (-\frac{i}{\hbar})^2\int_{t_0}^{t} H(\tau_1)d\tau_1\int_{t_0}^{\tau_1} H(\tau_2)U(\tau_2,t_0)d\tau + \cdots \\ &= I + \sum_n (-\frac{i}{\hbar})^n \int_{t_0}^{t} d\tau_n \int_{t_0}^{\tau_n} d\tau_{n-1}\cdots\int_{t_0}^{\tau_2} d\tau_1 H(\tau_n)H(\tau_{n-1})\cdots H(\tau_1) \end{aligned} \tag{B.5}$$

Recalling our Hamiltonian $H(t) = H_0 + V(t)$, in the interaction picture, we reformulate $U(t,t_0)$ into $U_0(t,t_0)U_I(t,t_0)$, where U_0 and U_I represent the time-evolution operators driven by H_0 and $V(t)$, respectively. Therefore, $U(t,t_0)$ is expressed as following

$$\begin{aligned} U(t,t_0) &= U_0(t,t_0)U_I(t,t_0) \\ &= U_0(t,t_0)U_I(t,t_0) \\ &= U_0(t,t_0)\times\{I + \sum_n (-\frac{i}{\hbar})^n \int_{t_0}^{t} d\tau_n \int_{t_0}^{\tau_n} d\tau_{n-1}\cdots\int_{t_0}^{\tau_2} d\tau_1 V(\tau_n)V(\tau_{n-1})\cdots V(\tau_1)\} \\ &= U_0(t,t_0) + \sum_n (-\frac{i}{\hbar})^n \int_{t_0}^{t} d\tau_n \int_{t_0}^{\tau_n} d\tau_{n-1}\cdots\int_{t_0}^{\tau_2} d\tau_1 U_0(t,t_0)V(\tau_n)V(\tau_{n-1})\cdots V(\tau_1) \end{aligned} \tag{B.6}$$

Subsequently, the exact wavefunction $|\psi(t)\rangle$ can be presented as

$$\begin{aligned} |\psi(t)\rangle &= U_0(t,t_0)U_I(t,t_0)\,|\psi(t_0)\rangle \\ &= U_0(t,t_0)\,|\psi(t_0)\rangle \\ &+ \sum_n (-\frac{i}{\hbar})^n \int_{t_0}^{t} d\tau_n \int_{t_0}^{\tau_n} d\tau_{n-1}\cdots\int_{t_0}^{\tau_2} d\tau_1 U_0(t,t_0)V(\tau_n)V(\tau_{n-1})\cdots V(\tau_1)\,|\psi(t_0)\rangle \end{aligned} \tag{B.7}$$

Therefore, by comparing B.3 and B.7. we obtain the zero-order wavefunction evolved

doi:10.6342/NTU202404353

solely by $H_0$and the other orders of wavefunction denoted as

$$
\begin{aligned}
&\left|\psi^0(t)\right\rangle = U_0(t,t_0)\left|\psi(t_0)\right\rangle \\
&\sum_n \left|\psi^{(n)}(t)\right\rangle \\
&= \sum_n (-\frac{i}{\hbar})^n \int_{t_0}^{t} d\tau_n \int_{t_0}^{\tau_n} d\tau_{n-1} \cdots \int_{t_0}^{\tau_2} d\tau_1 U_0(t,t_0)V(\tau_n)V(\tau_{n-1})\cdots V(\tau_1)\left|\psi(t_0)\right\rangle
\end{aligned}
\tag{B.8}
$$

In summary, the wavefunction $|\psi(t)\rangle$, derived from $H(t) = H_0 + V(t)$, can be effectively addressed with time-dependent perturbation theory.

To accurately depict the dynamics and light-matter interactions observed in the spectrocopy, it is essential to introduce a density matrix derived from the Liouville-von Neumann equation within the interaction picture.

$$
\frac{\partial}{\partial t}\rho_I(t) = \frac{-i}{\hbar}[V(t), \rho_I(t)] \tag{B.9}
$$

From the equation, we can obtain

$$
\begin{aligned}
&\rho_I(t) \\
&= \rho_I(t_0) + \sum_n (-\frac{i}{\hbar})^n \int_{t_0}^{t} d\tau_n \int_{t_0}^{\tau_n} d\tau_{n-1} \cdots \int_{t_0}^{\tau_2} d\tau_1 [V(\tau_n), [V(\tau_{n-1}), \cdots [V(\tau_1), \rho(t_0)]] \cdots]
\end{aligned}
\tag{B.10}
$$

Subsequently, we transition this representation to the Schrödinger picture.

$$
\begin{aligned}
\rho(t) &= U_0(t,t_0)\rho_I(t)U_0^\dagger(t,t_0) \\
&= \rho^0(t) + \sum_n (-\frac{i}{\hbar})^n \int_{t_0}^{t} d\tau_n \int_{t_0}^{\tau_n} d\tau_{n-1} \cdots \int_{t_0}^{\tau_2} d\tau_1 \\
&U_0(t,t_0)[V(\tau_n), [V(\tau_{n-1}), \cdots [V(\tau_1), \rho(t_0)]] \cdots]U_0^\dagger(t,t_0) \\
&= \rho^0(t) + \sum_n \rho^{(n)}(t)
\end{aligned}
\tag{B.11}
$$

doi:10.6342/NTU202404353

In the end, the zero- and nth-order density matrices can addressed from the Liouville-von Neumann equation. By definition, polarization can be formulated as

$$\begin{aligned} P(t) &= \langle \hat{\mu}\rho(t) \rangle \\ &= P^0(t) + \sum_n P^{(n)}(t) \end{aligned} \tag{B.12}$$

doi:10.6342/NTU202404353